Volume 1
Number 6
September 2021
Pages 291–474

Environmental Science
Atmospheres

rsc.li/esatmospheres

ISSN 2634-3606

ROYAL SOCIETY OF CHEMISTRY

CRITICAL REVIEW
Hind A. Al-Abadleh
Aging of atmospheric aerosols and the role of iron in catalyzing brown carbon formation

Environmental Science: Atmospheres

ROYAL SOCIETY OF CHEMISTRY

CRITICAL REVIEW

View Article Online
View Journal | View Issue

Cite this: *Environ. Sci.: Atmos.*, 2021, **1**, 297

Aging of atmospheric aerosols and the role of iron in catalyzing brown carbon formation†

Hind A. Al-Abadleh *

Extensive research has been done on the processes that lead to the formation of secondary organic aerosol (SOA) including the atmospheric oxidation of volatile organic compounds (VOCs) from biogenic and anthropogenic sources, gas–particle partitioning, and multiphase/heterogeneous reactions. Also, a number of chemical and photochemical aging processes of primary aerosols and SOA were reported to lead to the formation of "brown carbon (BrC)", a term that refers to light absorbing soluble and insoluble components. However, the role of transition metals such as iron in these processes is not well understood. This review summarized the current state of knowledge on iron chemistry that lead to BrC formation. Dark iron chemistry with phenolic and aliphatic organic precursors is shown to be responsible for the efficient formation of soluble and insoluble BrC, including organonitrogen compounds, under a wide range of atmospheric aerosol physical states and chemical compositions. These efficient processes are not completely suppressed in the presence of competing ligands or light. The atmospheric impact of SOA and BrC from these pathways is discussed in the context of aerosols' direct and indirect effects on the climate. Additional laboratory, field, and modeling studies are needed to better understand the contributions of these potentially important metal-catalyzed pathways to SOA and BrC formation and the overall aerosol chemistry.

Received 11th May 2021
Accepted 6th July 2021

DOI: 10.1039/d1ea00038a

rsc.li/esatmospheres

Environmental significance

Atmospheric aerosols contribute to the climate radiative forcing through their aerosol–radiation and aerosol–cloud interactions. Particles that are darker in color are expected to have a stronger direct effect on the climate by absorbing solar radiation. Also, salts and mineral dust particles are efficient cloud and ice condensation nuclei. However, the extent of the above interactions remains highly uncertain stemming from the multitude of chemicals and processing pathways that modify aerosols' physicochemical properties. Dust particles from natural and human activities contain iron, which is the fourth most abundant element by mass in the Earth's crust. Through long range transport and atmospheric processing, these particles frequently mix with organic gases and particles such as those in biomass burning smoke. This review shows that iron is capable of catalyzing chemical reactions with organics that make aerosol particles more light-absorbing over a wide range of conditions. These new pathways are currently unaccounted for in atmospheric models and hence their inclusion would improve the parameterization of processes that lead to secondary organic aerosol formation and aging, and ultimately impacts on the climate.

1. Introduction

Atmospheric aerosol particles in the lower troposphere originate from primary sources and secondary processes.[1–7] Aerosol particles from primary sources include mineral dust, sea spray, terrestrial primary biological aerosol particles (bioparticles for short) such as fungal spores and pollen, primary organic aerosol such as brown carbon (BrC) and black carbon (BC) from biomass burning events referred to as biomass burning organic aerosol (BBOA). Also, an emerging class of 'unconventional' mineral dust is the one produced from rapid urbanization and industrialization, particularly in developing countries. This class is referred to as anthropogenic fugitive, combustion, and industrial dust (AFCID),[8] which largely contributes to fine particulate matter ($PM_{2.5}$) known to be harmful to human health.[9–11]

Secondary processes refer to particle formation and growth from reactions in the atmosphere among inorganic and organic precursors in the gas and condensed phases. These reactions lead to the formation of ammonium, non-sea salt sulfates, nitrates, and secondary organic aerosol (SOA) particles,[12–15] from ammonia, sulfur-containing gases such as sulfur oxides, nitrogen oxides, and volatile organic compounds (VOCs) of biogenic[16] and anthropogenic[17] origins. The organic component in the fine aerosol particle fraction (diameter less than 1 μm) contributes to more than 50% of the aerosol mass.[15] Aerosol particle resident time ranges from hours up to 10–15 days during which they undergo long range transport over thousands

Department of Chemistry and Biochemistry, Wilfrid Laurier University, Waterloo, ON, N2L 3C5, Canada. E-mail: halabadleh@wlu.ca

† Electronic supplementary information (ESI) available: Video from optical microscopy images collected for Fe-polyfumarate at the surface of the droplet while flowing humid air. See DOI: 10.1039/d1ea00038a

of miles.[18] They are removed from the atmosphere mainly *via* sedimentation and dry and wet deposition. As a result, atmospheric aerosol particles contribute to the biogeochemical cycles of nutrients such as nitrogen, phosphorus, iron and other transition metals.[19–21]

Atmospheric aerosol particles impact the climate system because they have complex physical and chemical properties that evolve over time and govern their lifetime in the atmosphere.[22] These properties also govern their biological and toxicological impacts, which are of importance to understand and quantify the aerosol effects on ocean productivity and human health,[23] respectively. McMurry published a review of atmospheric aerosol measurements of physical and chemical properties,[24] which are classified into categories according to the instrumental capacity to resolve their size, time and composition. Since McMurry's paper, edited books[25,26] and a number of reviews were published on advanced analytical tools[27] used to study the hygroscopic properties and water uptake,[28] ice nucleation,[29,30] aerosol morphology and mixing states,[31,32] optical properties,[33] viscosity,[34] liquid–liquid phase separation,[35] acidity,[36,37] and chemical composition.[15,38–42]

All of the aforementioned properties contribute to the direct and indirect effects of aerosol particles on the climate. The direct effect of aerosol particles refers to their role in modifying the planetary energy balance (*i.e.*, radiative forcing) and precipitation, which has the highest uncertainty in climate and weather models.[6] Aerosol particles affect the radiative forcing directly through absorption and scattering of shortwave and longwave radiation. This effect is quantified through the radiative forcing due to the aerosol–radiation interaction term (RFari) in W m^{-2}. Positive RFari indicates heating effects and negative RFari indicates cooling. RFari values for different anthropogenic aerosol types are shown in Fig. 1, for the 1750–2010 period. Fig. 1 also shows that the highest uncertainty in RFari is associated with the organic content of atmospheric aerosol particles, with BC resulting in the net heating effect, and BBOA and SOA having both heating and cooling effects.

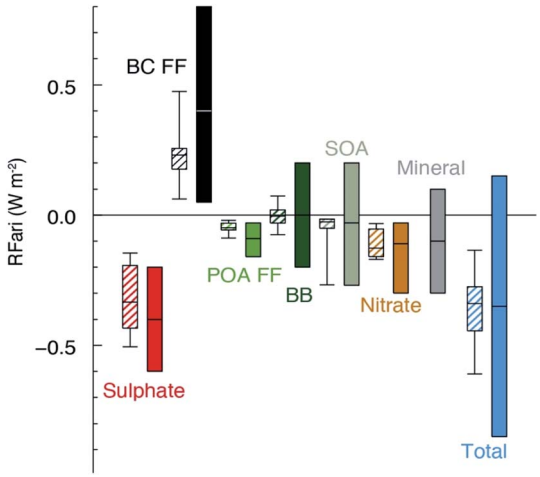

Fig. 1 Annual mean top of the atmosphere radiative forcing due to aerosol–radiation interactions (RFari, in W m^{-2}) due to different anthropogenic aerosol types, for the 1750–2010 period. Hatched whisker boxes show median (line), 5th to 95th percentile ranges (box) and min/max values (whiskers) from AeroCom II models[43] corrected for the 1750–2010 period. Solid coloured boxes show the IPCC Assessment Report 5 (AR5) best estimates and 90% uncertainty ranges. BC FF is for black carbon from the fossil fuel (FF) and the biofuel, POA FF is for primary organic aerosol from fossil fuel and biofuel, BB is short for BBOA for biomass burning organic aerosols and SOA is for secondary organic aerosol. The figure and the caption were reproduced from ref. 1 with permission from Cambridge University Press, © 2013.

The indirect effects of aerosols are related to cloud formation and lifetime and modification of atmospheric composition through multiphase and heterogeneous surface chemistry. Aerosol particle–cloud interactions are coupled by a multitude of dynamical and physical processes that span multitemporal and spatial scales (minutes to months, and meters to thousands of kilometers).[6] Changes in relative humidity (RH) and temperature affect the aerosol phase, phase transitions, extent of surface *versus* bulk chemistry, formation of haze, and activation of aerosol particles as cloud condensation nuclei (CCN) and ice nuclei (IN).[22] The water content in atmospheric aerosols refers to water activity in the condensed phase of atmospheric particles and droplets. In addition to the effect of RH and temperature, the amount of aerosol liquid water varies with particle size and surface tension. The latter property is sensitive to the surface chemical composition, which in turn controls the solubility, viscosity and hydrophilicity. Uptake of gas phase water on the surfaces of insoluble aerosol particles such as freshly emitted mineral dust and hydrophobic organics results in the formation of 'adsorbed water', which can take the form of either thin films or islands depending on the thermodynamic favourability of hydrogen bonding with the underlying surface. In the case of hydrophobic organics, their hygroscopicity is related to surface tension, which is affected by the carbon chain length, functional groups, presence of surfactants, and oxygen to carbon (O : C) ratio, and can lead to liquid–liquid phase separation.[44]

Hind A. Al-Abadleh is a Full Professor in the Department of Chemistry and Biochemistry at Wilfrid Laurier University. She is the 2021–2022 University Research Professor, a Fellow at the Balsillie School of International Affairs in Waterloo, Ontario, Canada, and was the 2019 Fulbright Canada Visiting Research Chair in Atmospheric Chemistry, Air Quality, and Climate Change at the University of California Irvine. The active research programs in her lab are in the fields of atmospheric chemistry, air quality, geochemistry, and environmental remediation. Among her leadership roles, Al-Abadleh is the current Chair of the Environment Division of the Chemical Institute of Canada and Vice Chair of the Special Interest Group on Atmosphere-Related Research in Canadian Universities (ARRCU) at the Canadian Meteorological and Oceanographic Society (CMOS).

Water uptake by pure salts, highly soluble organics and mixtures of soluble salts and organics proceeds *via* different mechanisms than on surfaces of insoluble materials.[45–47] While adsorption still occurs on dry salt particles at low RH, phase transitions, namely deliquescence and efflorescence are observed at room temperature as a function of increasing and decreasing RH, respectively.[45,46,48,49] Hence, aerosols not only contribute to the changing atmospheric temperature but also to the hydrological cycle and precipitation frequencies.

In addition, atmospheric aerosols provide unique multicomponent reaction environments whose reactivity can change the chemical composition of the gas and condensed phases. The term 'atmospheric aging' refers to the processes that change the physicochemical properties of aerosol particles during their residence time in the atmosphere. These processes can take place at the surface of the particles or within the condensed phase. The physicochemical properties mentioned above influence the rates of chemical processes during the aging of aerosol particles. In general, the term 'multiphase chemistry' is an all-encompassing term that refers to bulk and heterogeneous chemical and photochemical reactions of atmospheric aerosol particles from primary and secondary sources within the condensed phase and the surrounding gas phase. The area-to-volume ratio of atmospheric aerosols determines the extent of surface (*i.e.*, interfacial) *versus* bulk reactions in changing the chemical composition and physical properties of the particles. This ratio changes with evaporation and water uptake processes due to changes in temperature and relative humidity. Fig. 2 shows a schematic diagram of some of the reactions and processes that highlight the chemical interplay between the atmospheric gas, particle and droplet phases. The majority of reactions with VOCs, carbon monoxide (CO), nitrogen oxides (NO_x) and sulfur dioxide (SO_2) in the gas phase are initiated and propagated by oxidants (OH, O_3, H_2O_2, HO_2, RO_2, NO_3, O_2, halogen radicals, *etc.*)[50–52] leading to degradation of VOCs[53] or formation of SOA.[12–14,54] These gases and reaction products could also adsorb or react on mineral and organic surfaces, depending on the amount of surface water and the chemical composition of the surface.[55–58] Hence, atmospheric aerosol particles and cloud/fog droplets can act as a sink or source for atmospheric gases[56,59,60] and provide surfaces for heterogeneous reactions at the gas/liquid[61] or gas/solid (semi-solid) interfaces.[56,62] These atmospheric particles also act as seeds for the condensation of low volatility reaction products.[14,63–65] Reaction products in cloud or surface water could be soluble[66,67] or insoluble[68–70] in water. Hence, in multicomponent systems containing organic, inorganic salts and water, partitioning between organic and aqueous phases can take place. Evaporation of the aerosol liquid water content with decreasing relative humidity leads to efflorescence and liquid–liquid phase separation, driven by the salting-out effect.[35,71] Therefore, atmospheric aging of particles changes the chemical composition of the gas and condensed phases and can – in some cases – lead to particle growth through condensation and formation of clusters, oligomers and polymers. Atmospheric aging of aerosol particles also leads to changing optical properties,[33,72] cloud condensation and ice nucleation efficiencies.[73]

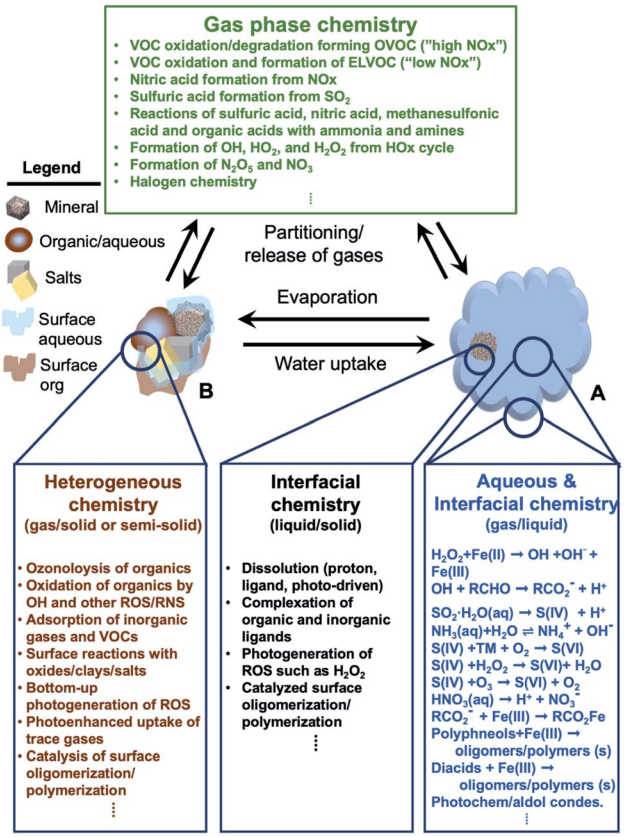

Fig. 2 Schematic diagram of reactions and processes that highlight chemical coupling in the atmospheric gas, particle and droplet phases. Day and night time gas phase chemistry leads to the degradation of VOCs, nucleation and growth of SOA, generation of reactive radicals, and transformation of NO_x and SO_2. Gas phase reactants and products can partition to cloud/fog droplet (A) or aerosol particles (B). The organic content in B could be from primary or secondary sources. A cloud/fog droplet (A) is a microreactor for bulk and heterogeneous chemistry at the liquid/solid or semi-solid and gas/liquid interfaces. Evaporation processes decrease the amount of liquid water in aerosol particles (B) leading to crystallization of salts and preferential 'salting out' of organics. Reactions in A and B can release gases as well. Abbreviations are: oxygenated volatile organic compounds (OVOCs), extremely-low VOC (ELVOC), and transition metals (TMs).

The objective of this review is to recount the current state of knowledge of the role of transition metals, iron in particular, in catalyzing reactions that lead to atmospheric BrC formation. Dust is a major source of iron in atmospheric aerosols[74–78] because iron is the most abundant transition metal in the Earth's crust.[79] Anthropogenic combustion[80] including coal burning[81,82] and biomass burning,[83–85] in addition to brake wear,[86] is found to contribute 50% of the total soluble iron deposited on the ocean.[85,87,88] Single particle analysis of field-collected aerosols from the marine, urban and rural sites showed that they contain soluble and insoluble iron.[85,89–99] Field studies reported the transport of transition metals including iron from the oceans to the atmosphere in the form of sea spray and metal enrichment at the interface of marine aerosols.[100–102] An earlier review article focused on the chemical aging of atmospheric aerosols containing iron and organic matter,

particularly those that model humic-like substances (HULIS).[77] In that review, a recount of the literature was provided from field measurements and modelling studies of iron in aerosols, iron chemistry under dark conditions, photochemical reactions driven by iron obtained from bulk and surface-sensitive measurements, and molecular level differences between bulk and surface water that affect the reaction mechanisms. The scope of this review is to recount the recent results that highlight the role of iron in catalyzing soluble and insoluble atmospheric BrC formation by new and potentially important pathways. This review is organized into five main sections: iron in atmospheric aerosols, organic compounds in atmospheric aerosols, complexation and redox reactivity of iron with organics, case studies on iron-catalyzed insoluble and soluble BrC formation, and atmospheric impact. The review concludes with a summary and directions for future research.

2. Iron in atmospheric aerosols

The chemistry of iron species is rich under a wide range of atmospherically relevant conditions. The following sections elaborate on the sources of iron in atmospheric aerosol particles, atmospheric aging pathways that lead to iron solubilization, and soluble iron concentrations in aerosol liquid water.

2.1 Sources

Mineral dust from natural and anthropogenic sources is a major component of primary aerosols in the atmosphere with the estimated atmospheric loading and emission flux of 19.2 Tg and 1840 Tg year^{-1}, respectively.[73,103] On the other hand, global fluxes and mass loadings of AFCID have been severely underrepresented in regional and global models, despite having surface $PM_{2.5}$ measurement networks for emission inventories (see the Surface PARTiculate mAtter Network (SPARTAN), https://www.spartan-network.org). Philip *et al.*[8] included AFCID emissions in a global simulation using GEOS-Chem. Fig. 3 shows the annual mean concentration of $PM_{2.5}$ dust for 2014–2015: total dust (top panel), natural mineral dust (middle panel), and AFCID (bottom panel), as simulated with the GEOS-Chem model. Also shown in the top panel are circles for different locations that compare the mean measured $PM_{2.5}$ dust from the SPARTAN in 2013–2015 (inner circles) with simulated values (outer circles). It was estimated that 2–16 μg m^{-3} of AFCID increases $PM_{2.5}$ dust concentrations across East and South Asia.[8] As noted by the authors, this concentration of simulated AFCID is comparable to that of natural mineral dust over parts of Europe and Eastern North America.[8] Overall, dust particles provide surfaces for a range of chemical reactions with trace inorganic and organic species resulting in a change in the chemical composition and hygroscopic properties of these particles.[55,73,78,104] The following section expands on dust aging in the atmosphere.

2.2 Atmospheric aging of mineral dust

The residence time of dust in the atmosphere during long range transport impacts the climate through affecting the surface

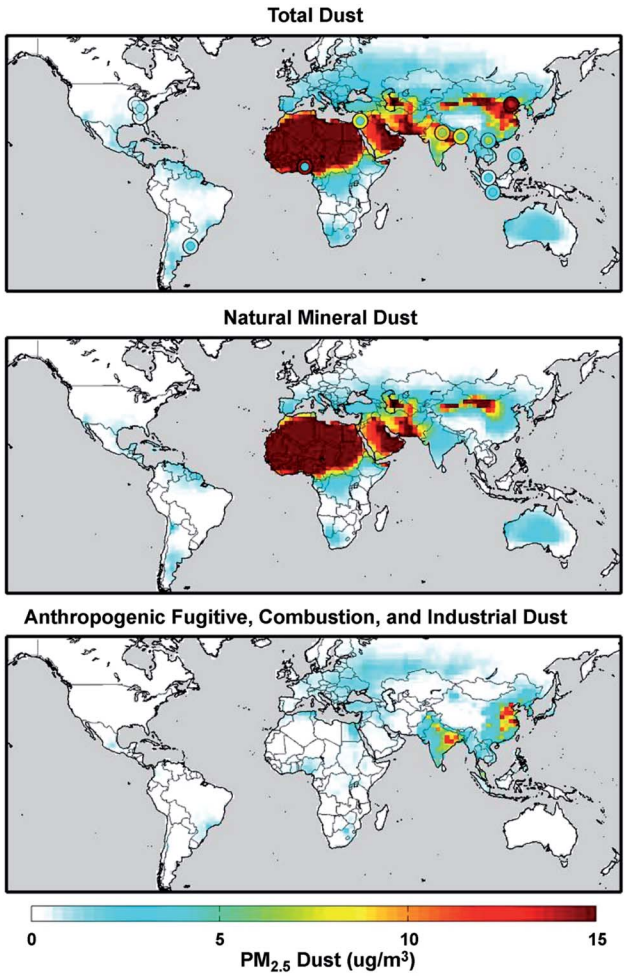

Fig. 3 Annual mean (2014–2015) concentration of $PM_{2.5}$ total dust (top panel), natural mineral dust (middle panel), and anthropogenic fugitive, combustion, and industrial dust (bottom panel) simulated with the GEOS-Chem model. Colored concentric circles in the top panel denote SPARTAN-measured campaign-mean (2013–2015) $PM_{2.5}$ dust concentration (inner circle) and the coincident simulated value (outer circle). Reproduced from ref. 8 with permission from the Institute of Physics (IOP) Science Publishing, © The Author(s), 2017.

temperature, wind, clouds, and precipitation rates.[105] The long range transport increases the solubility of iron-containing minerals depending on their composition. The iron mineralogical composition varies from poorly crystalline to crystalline iron oxides to clay minerals depending on the source region.[106] The ratio of crystalline hematite to the total of hematite and goethite is reported to vary with the geographical location. For example, for Asian dust, the ratio ranges from 0.32 to 0.37, whereas for North African dust from 0.29 to 0.63.[106] The surface area was also found to be the predominant factor affecting iron solubility through acidic surface reactions.[107] Asian[108–110] and Saharan African dust[111–114] have been shown to undergo extensive processing during long range transport that impact their mixing state and morphology.[31] The uptake coefficients of OH, HO_2, H_2O_2, O_3, HCHO, HONO, NO_3, and N_2O_5 on mineral dust particles and their proxies were reported to range from 10^{-6} to

0.2.[115] Heterogeneous reactions of African mineral dust with VOCs were found to be irreversible for limonene and reversible for toluene.[116]

Acidic reaction conditions are commonly found in atmospheric aerosol particles, as well as in fog and cloud droplets, where soluble and insoluble iron species catalyze a number of chemical processes.[77,117–119] In the presence of water soluble organic compounds, acidic reaction conditions can lead to secondary products.[120] Freshly emitted dust particles contain more than one monolayer of adsorbed water over a wide relative humidity range.[73] Surface reactions of dust with nitric and sulfuric acids lead to the formation of adsorbed nitrate and sulfate, which is enhanced in the presence of water.[104] Photolysis of surface nitrate was reported to release NO_2, which reacts with mineral dust to produce HONO.[104,121] Near-neutral pH was also reported for cloud droplets.[122] There have been no attempts to directly measure the pH of surface water in dust. Basic pH is typically measured in the slurries of unprocessed dust due to the presence of metals that act as Lewis acid sites.[123]

In addition, mixing with biomass burning products that include gases and aerosol particles also occur during the long range transport of dust.[124,125] For example, Paris *et al.*[126] reported that entrainment of dust deposited on vegetation makes biomass burning a significant indirect source of iron, where mixing with biomass burning aerosols enhances the solubility of iron. Li *et al.* in ref. 109 and 110 show electron microscopy images of aged sulfur-rich dust particles encapsulated with an organic film from either primary or secondary sources. In the same studies, soot particles were found to be internally mixed with sulfur- and iron-rich particles. These mixing states provide realistic scenarios for iron-catalyzed reactions to take place within or at the surface of dust particles.

The main two mechanisms that lead to iron release from dust and iron (oxyhydr)oxides are proton- and ligand-promoted dissolution.[127–129] Laboratory and field studies from nearly four decades of research into these mechanisms showed that a number of variables play a role, namely the pH, particle size, degree of crystallinity, presence of solar radiation, and adsorption mode of Fe–organic complexes (*i.e.*, structure of surface complexes).[130–133] In general, the highest rates of dissolution occur under acidic conditions[107,134] (pH < 4), in the presence of solar radiation and oxalate, with nanometer size and amorphous iron-containing particles. Also, UV irradiation of aqueous organic aerosol tends to fragment organic compounds producing smaller, more volatile compounds from larger oligomeric ones.[135–137] Light-absorbing compounds derived from BBOA have also been found to fragment and photobleach under irradiated conditions.[138] Such photodegradation processes can be amplified in the presence of Fe(III), which efficiently catalyzes photo-Fenton processes.[139–146]

2.3 Concentration of soluble iron

The concentration of iron in rainwater and fog, snow, and cloud waters from different locations was summarized by Deguillaume *et al.*[119] The data show that the total and dissolved iron concentrations are location dependent and range from 0.1 to 1138 μM. Hence, a typical concentration of dissolved Fe(III) in cloud droplets (diameter ∼ 20 μm) is around 10^{-6} M.[119] Therefore, for an aerosol particle produced by evaporation of cloud droplets down to a diameter of 1 μm, the concentration of dissolved Fe(III) could be as high as 10 mM. For example, Gen *et al.*[147] measured iron concentrations in fine particles across China in the range 331–1640 ng m^{-3}. To estimate the concentration of water soluble iron, they used the typical lower limit of iron solubility of 5%. The corresponding molar concentrations were calculated using an aerosol liquid water content of 6×10^{-8} L m^{-3} of air and found them to range from 5 to 43 mM. Since the reaction kinetics are affected by the concentration of reactants, exploring iron chemistry using micro- to millimolar levels would cover the range of reactions in aerosol to droplet nano- to micro-environments.

3. Organic compounds in atmospheric aerosols

Organic compounds represent a major fraction of atmospheric aerosol particles. Advances in the analysis of organic aerosol particles from primary and secondary sources have been the subject of a number of reviews.[15–17] The organic content in atmospheric particles is characterized by a number of functional groups with the oxygen-to-carbon elemental ratio (O : C) ranging from 0.1 to 1.0 and are often grouped together into classes of compounds.[35] Our latest study[148] highlights that the knowledge of the pK_a values of organic acids, some of which are currently incorporated in atmospheric chemistry models, is not enough to fully understand their complexation and reactivity with transition metals. The knowledge of structural effects on the kinetics of these reactions provides invaluable information of the role of the diacids in changing the chemical and physical properties of aerosol particles. Identifying functional groups in organic aerosol particles aid in understanding and predicting their chemical and photochemical reactivities. Examples of 'offline' techniques used to identify organic functional groups are Fourier transform infrared spectroscopy (FTIR) and nuclear magnetic resonance spectroscopy (NMR). The application of infrared spectroscopy to the detection and quantification of functional groups in water soluble organic particles from the smog chamber and field studies has been reviewed by Reggente *et al.*[149] and Gao *et al.*[150] The identification and quantification of functional groups in organic aerosol particles using NMR Spectroscopy was reviewed by Duarte and Duarte.[39,151] Classes of identified organic functional groups include aliphatic, alkene, aromatic, and carbonyl carbon, in addition to alcohols, organosulfates and amines. The following two sections highlight two classes of organic compounds whose reactions with iron led to the formation of BrC: phenolic compounds and unsaturated dicarboxylic acids.

3.1 Phenolic compounds

Biomass burning is one of the largest sources of organics, gases and BBOA in the atmosphere, in general, and phenolic compounds, in particular. Examples of these phenolic

compounds are catechol, guaiacol, resorcinol, and hydroquinone. The relative amounts of these compounds vary with fuel type[152] and combustion conditions.[153,154] Also, these compounds are produced by photo-oxidation of aromatic VOCs, are well-known aromatic SOA precursors, and are simple models for the aromatic fraction of HULIS in aerosol particles.[155] Similar to atmospheric dust, BBOA travels long distances[156] and hence there are realistic scenarios in which catechol and related compounds can end up in iron-containing particles. For example, primary particles from cooking emissions contain internally mixed soluble iron and organics.[157] Smoke from biomass burning is often spread by wind, which also lifts

Table 1 Physical properties of selected semi-volatile phenolic compounds reactive with iron

Compound name	Structure[a]	O : C molar ratio	Molecular weight[a] (g mol^{-1})	pK_a at[a] 25 °C	Henry's law constant[b] (M atm^{-1}) at 25 °C
Catechol ($C_6H_6O_2$, CA)	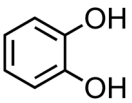	0.33	110.11	9.3, 12.6	8.3×10^5
3-Hydroxycatechol ($C_6H_6O_3$, 3-HC)	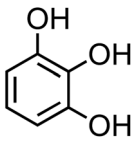	0.5	126.11	9.0, 11.6, 14	6.4×10^6
4-Hydroxycatechol ($C_6H_6O_3$, 4-HC)	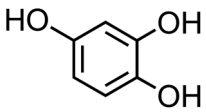	0.5	126.11	9.1, 11.6, —	—
4-Nitrocatechol ($C_6H_5NO_4$, 4-NC)	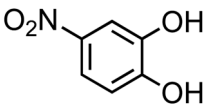	0.67	155.11	6.7, 11.3	$\sim 10^6$
4-Methylcatechol ($C_7H_8O_2$, 4-MC)	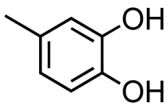	0.29	124.14	9.6, 14	—
Guaiacol ($C_7H_8O_2$, GA)	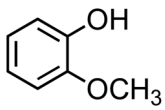	0.29	124.14	10	973
Coniferaldehyde ($C_{10}H_{10}O_3$, CON)	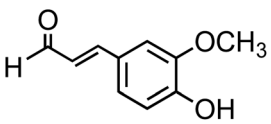	0.3	178.18	9.7	—
Syringol ($C_8H_{10}O_3$, SYR)	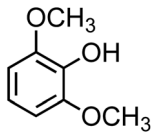	0.38	154.16	9.8	1.2×10^4
o-Cresol (C_7H_8O, *o*-CR)	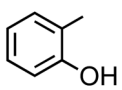	0.14	108.14	10.3	6.3×10^2
p-Cresol (C_7H_8O, *p*-CR)	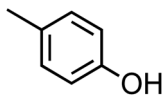	0.14	108.14	10.3	1.3×10^3
2,4-Dinitrophenol ($C_6H_4N_2O_5$, 2,4-DNP)	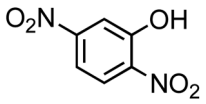	0.83	184.11	4.1	3.5×10^3

[a] From ref. 170–178. [b] From ref. 159, 161 and 179.

crustal particles off the ground. Mineral dust is known to be transported globally by wind, which offers ample time for the partitioning of organic vapors into iron-containing particles.

The simplest phenolic compounds are catechol and guaiacol. The gas phase concentration of catechol can be as high as 50 ppbv ($\sim 5 \times 10^{-8}$ atm), resulting from biomass burning, pyrolysis and combustion,[158] but in most cases it will be well below the 1 ppbv (10^{-9} atm) level. With Henry's law constant of 8.3×10^{5} M atm^{-1},[159] this translates into 41.5 mM and 0.83 mM, respectively, in a bulk system like a cloud droplet. The concentrations could be higher in the interfacial region of the particles because of surface enhancement of organics.[160] Similar calculations could be done for guaiacol that has a Henry's law constant of 973 M atm^{-1} (ref. 161) and for other polyphenols listed in Table 1. As presented in the following sections, the reactivity of these compounds and their derivatives with iron proceeds differently because of their structure.

3.2 Dicarboxylic acids

Dicarboxylic acids are abundant in atmospheric aerosols from continental, marine and polar regions with mass concentrations in tens to hundreds of ng m^{-3} of air.[162] Fig. 4 shows the gas phase and in-cloud oxidation processes responsible for their formation from natural and pollution-driven organic precursors. The most abundant diacid is oxalic acid (C2). Ubiquitous C3–C6 dicarboxylic acids such as malonic, malic, maleic, succinic, glutaric, fumaric and muconic acids are detected in BBOA aerosol particles[163] and used in laboratory studies investigating liquid–liquid phase separation.[35] Ring-opening reactions involving common atmospheric aromatic compounds, such as benzene, toluene, and xylenes, are known sources of unsaturated aldehydes[164] and dicarboxylic acids.[3] Muconic acid was identified as a product of photo-oxidation of benzene,[165,166] and fumaric, maleic, and succinic acids are commonly observed in the atmosphere.[167,168] These diacids, along with inorganic salts, influence the pH, ionic strength, water activity, and viscosity of the aerosol liquid water and also compete for binding to iron, specifically the anionic species.[169] Using an aerosol liquid water content of 6×10^{-8} L m^{-3} of air, Gen *et al.*[147] estimated the molar concentration of C2–C4 diacids to range from 3 to 95 mM depending on the diacid over a number of locations in China. Table 2 lists the physical properties of C2–C6 dicarboxylic acid that we used to explore their complexation with iron and their effect on the extent of BrC formation using catechol[68,148] and in the absence of catechol.[69] The following sections elaborate more on these cases.

4. Complexation and redox reactivity of iron with organics

The chemical state (*e.g.*, soluble *vs.* insoluble) and cycling of iron between oxidation states 3+ and 2+ depend on a number of chemical processes that include complexation strength to organic and inorganic ligands, the presence of electron donors/acceptors, and absorption kinetics of UV-vis light. The following sections elaborate on these topics beyond what was covered in the earlier review.[77]

4.1 Soluble organic complexes with iron

Acidic and phenolic functional groups are strong complexing agents to soluble iron.[77] Visual MINTEQ freeware is a chemical equilibrium computer program with extensive thermodynamic databases that allow for the calculation of speciation, solubility, and equilibrium of solid and dissolved phases of minerals in an aqueous solution.[182] Visual MINTEQ has a large selection of organic acids and includes a database management tool that allows organic species to be easily added or deleted. It could be used as a tool to obtain values for the pK_a and complex stability constants (log K). Also, this program can generate the relative concentration of different species that exist in solution at equilibrium. Fig. 5 shows examples of iron speciation curves in solution mixtures containing iron chloride, oxalic acid and

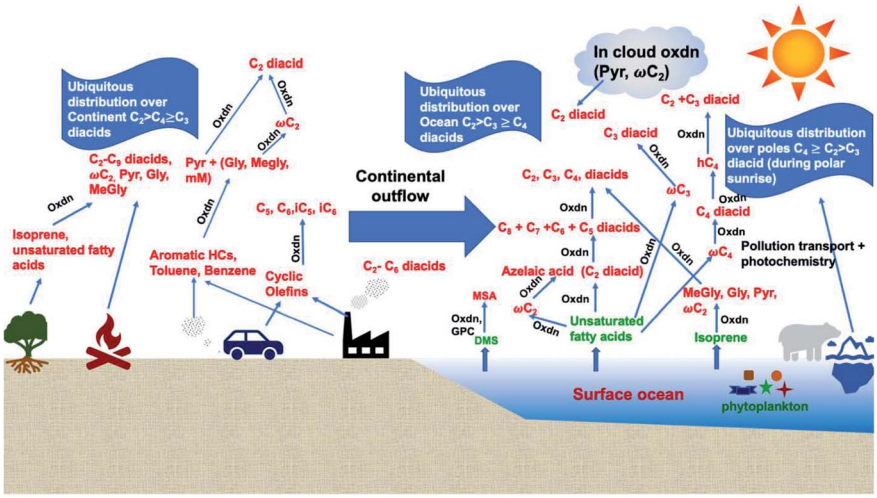

Fig. 4 Schematic representation of atmospheric reaction pathways of dicarboxylic acids and other related water-soluble organic compounds (Oxdn = photochemical oxidation). Adapted from ref. 162 with permission from Elsevier, © 2016.

Table 2 Physical properties of selected dicarboxylic acids

Compound name	Structure[a]	O : C molar ratio	Molecular weight[a] (g mol^{-1})	pK_a at[a] 25 °C	Aqueous saturation concentration[b] (wt%) at 25 °C
Oxalic acid ($C_2H_2O_4$)	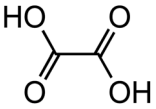	2	90.03	1.3, 3.8	9.52
Malonic acid ($C_3H_4O_4$)	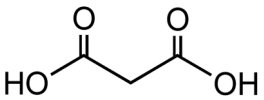	1.33	104.06	2.83, 5.69	61.3
Malic acid ($C_4H_6O_5$)	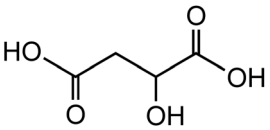	1.25	134.09	3.40, 5.11	57.4
Succinic acid ($C_4H_6O_4$)	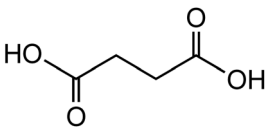	1	118.09	4.16, 5.61	7.2
Fumaric acid *trans*-$C_4H_4O_4$	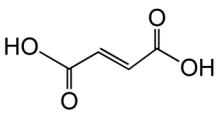	1	116.07	3.0, 4.2	0.7
Maleic acid *cis*-$C_4H_4O_4$	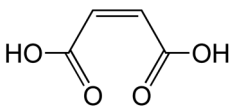	1	116.07	1.9, 6.2	44.1
Glutaric acid ($C_5H_8O_4$)	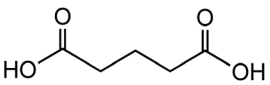	0.8	132.12	4.31, 5.41	58.8
Muconic acid (*trans*, *trans*-$C_6H_6O_4$)	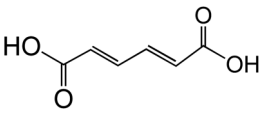	0.67	142	3.9, 4.7	Not determined

[a] From ref. 170. [b] From ref. 180 and 181.

ammonium sulfate as a function of pH.[68] These curves are very useful in quantifying dominant species at a given pH for accurate interpretation of chemical and photochemical reactivity in multicomponent systems.

The log K values of different iron complexes can be used in the interpretation of experimental data in multicomponent systems, as illustrated in the following sections. Reliable kinetic studies on iron complex formation with the organic ligands of atmospheric relevance are sparse. Table 3 lists values for the forward complex formation rate constants, k_f, between $FeOH^{2+}$ and selected aliphatic carboxylic acids for comparison with catechol. Within the experimental conditions listed in Table 3, the k_f value for forming the iron catecholate complex, $Fe(C_6O_2H_4)^+$ (Fe–CA), is 3× that for forming iron sulfate, $Fe(SO_4)_2^-$, and iron malate, $Fe(C_4O_5H_4)^+$ (Fe–MA). As described in detail in Section 5, iron-catalyzed polymerization of catechol forming insoluble black polycatechol particles and colored water-soluble oligomers occurs in systems containing excess ammonium sulfate (AS)/nitrate (AN) and C4–C5 dicarboxylic acids, which were used to vary the ionic strength under acidic pH (~2).[148]

4.2 Redox reactivity of iron forming soluble products

The presence of Fe(III)/Fe(II) species in aerosol particles can influence their oxidative potential through acting as electron acceptors/donors, respectively. The term "oxidative potential" refers to metal-driven redox chemical reactions that lead to the formation of reactive oxygen species (ROS), such as OH and H_2O_2, and also organic radicals/cations.[188] The redox reactions catalyzed by iron not only can cause degradation of water-soluble organics but also the formation of soluble and insoluble secondary and high molecular weight organics depending on the chemical structure of the organic precursors.[68–70,77,120,148,189–191]

Under oxic conditions, Fe(III) species are dominant. Using basic principles of electrochemistry, one can predict if a redox

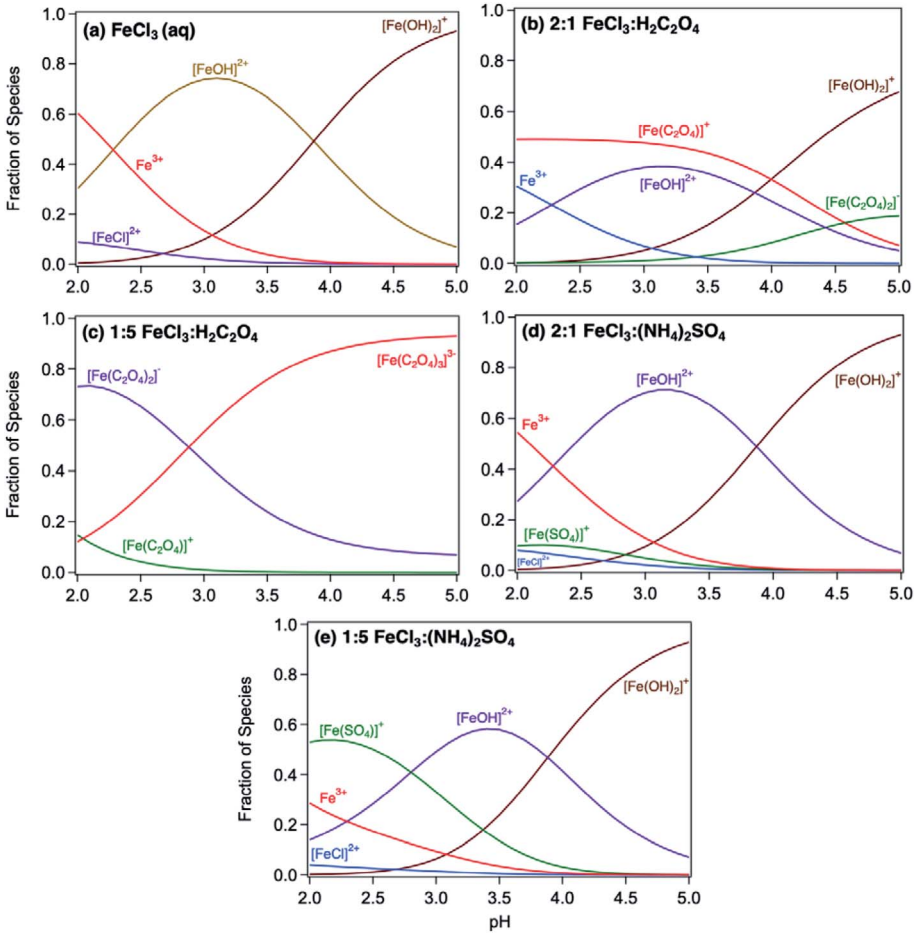

Fig. 5 Speciation curves of iron chloride, oxalate, and sulfate with variable molar ratios. Ratios in headings are mol : mol. The curves were generated using equilibrium constants for the acid dissociation and complexation reactions of iron from the database in Visual MINTEQ, v. 3.1. Reproduced from ref. 68 with permission from the American Chemical Society, © 2019.

reaction will take place spontaneously upon mixing Fe(III) with organic compounds acting as electron donors. In systems containing Fe(III), reduction reactions of iron species under acidic conditions are listed in Table 4 along with the reduction potential, E. Table 5 lists the oxidation potential and major products of phenol, catechol and guaiacol from electrochemical studies under acidic conditions.

For a system containing catechol/Fe(III) at pH 3, eqn (1) and (2) represent the redox coupling for the net reaction shown in eqn (3):

Oxidation:

$$\text{Catechol} \rightarrow \textit{ortho}\text{-quinone} + 2e + 2H^+,\ E_{ox1} = 0.4\ \text{V} \quad (1)$$

Reduction:

$$2Fe(OH)^{2+} + 2H^+ + 2e \rightarrow 2Fe(II) + 2H_2O,\ E_{red} = 0.72\ \text{V} \quad (2)$$

Net reaction:

$$\text{Catechol} + 2Fe(OH)^{2+} \rightarrow o\text{-quinone} + 2Fe(II) + 2H_2O,$$
$$E_{net} = E_{red} - E_{ox} = 0.72 - 0.4 = 0.32\ \text{V} \quad (3)$$

The net positive redox potential indicates that reaction (3) is spontaneous under acidic conditions. Using the same approach, it could be concluded that redox reactions between phenol and Fe(III) are non-spontaneous under acidic conditions, whereas they are with guaiacol. The oxidation potential of

Table 3 Literature values for the complex formation rate constant between $FeOH^{2+}$ and selected ligands. Reproduced from ref. 148 with permission from the American Chemical Society, © 2021

Reaction	Experimental conditions	Forward rate constant, k_f (M^{-1} s^{-1})	Ref.
Citric acid	20 °C, $[HClO_4]$ = 0.01–0.05 M, pH = 1–2	50–930	183
Oxalic acid	25 °C, 1 M $HClO_4$, 'acidic' pH	2×10^4 for FeO_x^+	184
Sulfate	25 °C, 1 M $NaClO_4$, pH = 0.7–2.5	1×10^3 for $Fe(SO_4)_2^-$	185
DL-Malic acid	25 °C, 1 M $NaClO_4$, pH = 1–2	$95–10^3$	186
Catechol	25 °C, 1 M $NaClO_4$, pH = 1–2	3×10^3 for $FeCA^+$	187

Table 4 Selected reduction reactions of Fe species and their electrochemical potentials from ref. 192

Rxn#	Reduction reaction	pH range	E (V) range and pH dependency
1	$Fe(III) + e \rightarrow Fe(II)$	0–2.12	0.77
2	$Fe(OH)^{2+} + H^+ + e \rightarrow Fe(II) + H_2O$	2.12–3.48	0.9–0.06 pH (pH 3, $E = 0.72$ V)
3	$Fe(OH)^{2+} + 2H^+ + e \rightarrow Fe(II) + H_2O$	3.48–6.30	1.10–0.12 pH (pH 4, $E = 0.62$ V; pH 5, $E = 0.5$)

a number of carboxylic acids of atmospheric relevance is higher than 1 V under acidic conditions. Hence, no spontaneous redox reactions take place with Fe(III) in solution.[197]

In addition, binding of Fe(III)/Fe(II) to polyphenols containing the catecholate or gallate (*i.e.*, 3-HC in Table 1) moieties plays a role in their antioxidant properties.[198,199] Complexes with Fe(II) quickly oxidize in the presence of oxygen in a process referred to as auto-oxidation to give Fe(III)–polyphenol complexes. Once these complexes form, the polyphenol can reduce Fe(III) to Fe(II) forming a semiquinone that further oxidizes to a quinone. If the organic ligands exist in excess, the coordination of two or three polyphenol ligands inhibits Fe(III) reduction processes.[198] As shown below in Section 5, irreversible oxidative polymerization reactions take place in systems with excess Fe(III) forming insoluble black particles, and the particle density depends on the organic ligand to iron molar ratios.

5. Case studies on iron-catalyzed insoluble and soluble BrC formation

The results on iron research to date summarized above are invaluable in understanding and predicting the chemical reactivity of dust aerosols. However, the role of dust in catalyzing the polymerization reactions of organics due to the soluble iron fraction and its effect – as a dust aging pathway – on the optical properties and the ice nucleation efficiency have received little attention under atmospherically relevant conditions. These reactions might be as efficient as those producing BrC from VOC precursors.[33] In the following sections, the results to date from our group and others show that iron can catalyze the oligomerization and polymerization reactions of phenolic compounds and some dicarboxylic acids in systems that model aerosol particles.

5.1 Phenolic precursors

5.1.1 Catechol and guaiacol. The phenolic compounds that have been tested to date for the reaction with soluble Fe(III) under acidic conditions and formed colored oligomeric and polymeric products over short periods of time (*i.e.*, 2 h) are the majority of those listed in Table 1. Slikboer *et al.*[70] reported the first set of experiments on the efficient formation of highly absorbing, water-insoluble particles of polycatechol and polyguaiacol from the reaction of Fe(III) at pH 3 with catechol and guaiacol at millimolar concentrations. Fig. 6 shows the digital photos of the unfiltered solutions as a function of time, dry particles collected on filters, and the UV visible spectra of reaction solutions. Both catechol and guaiacol solutions are transparent in the visible range and show a UV band around 274 nm due to $\pi \rightarrow \pi^*$ transitions in the benzene ring. The UV-vis absorbance spectrum of $FeCl_3$ solution (pale yellow) shows

Table 5 Electrochemical oxidation potential and reaction products of selected phenolic compounds

Compound	Oxidation potential (V)	Cyclic voltammetry experimental conditions	Oxidation reaction	Ref.
Phenol 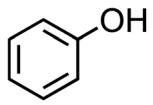	~1 (pH 0.2–2)	50 mV s^{-1} *vs.* Ag/AgCl 0.5–25 mM Pt electrode	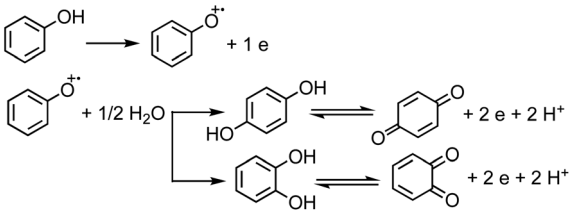	193 and 194
Catechol 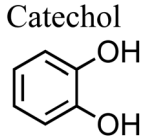	0.43 → 0.2 (pH 4 → 8)	50 mV s^{-1} *vs.* Ag/AgCl 1 mM Pt electrode	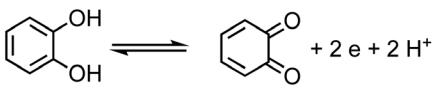	194 and 195
Guaiacol 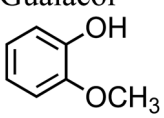	0.48–0.9 (pH 2)	100 mV s^{-1} *vs.* Ag/AgCl 0.1 mM boron-doped diamond electrode	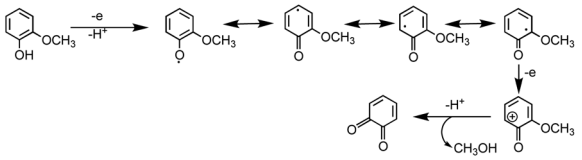	196

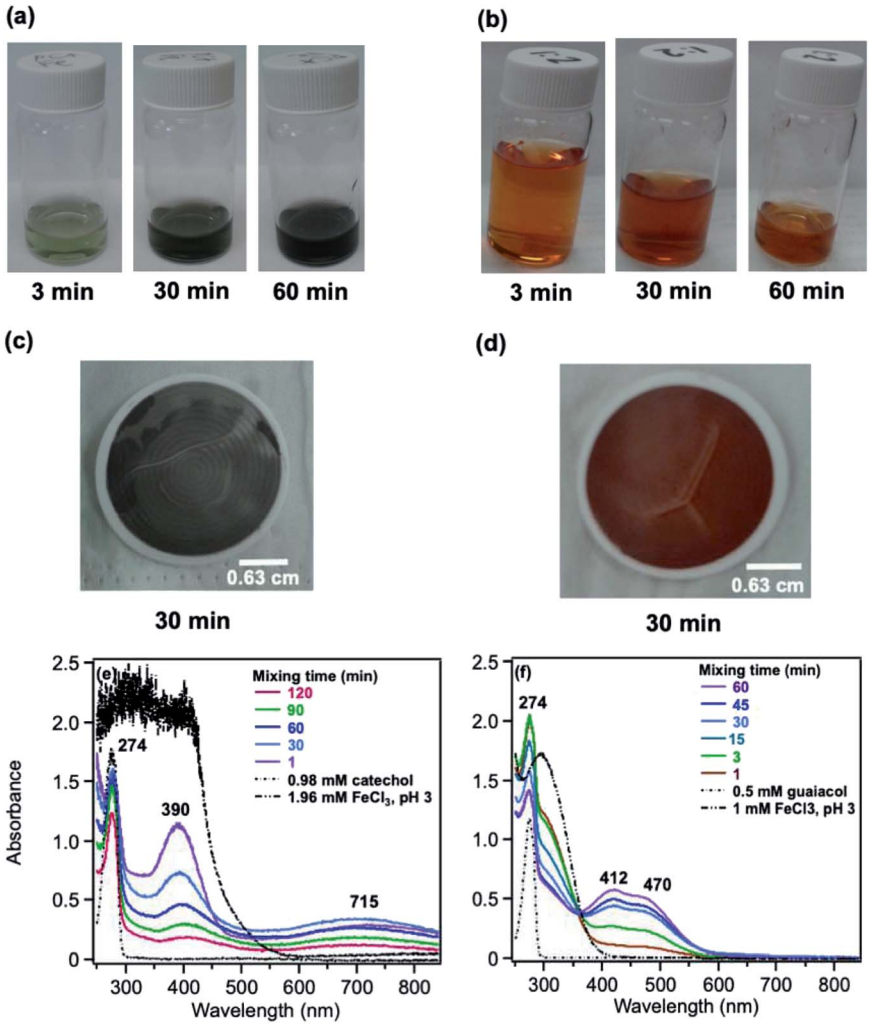

Fig. 6 Dark reaction of catechol and guaiacol with $FeCl_3$ at pH 3: (a and b) digital images of the 1 : 2 organic reactant/Fe molar ratio of unfiltered solutions as a function of time; (c and d) particles on filter after 30 min; and (e and f) the corresponding UV-vis spectra after filtration. Reproduced from ref. 70 with permission from the American Chemical Society, © 2015.

a band around 295 nm from the ligand-to-metal-charge transfer (LMCT) of the prevailing species in solution, $[Fe(H_2O)_5OH]^{2+}$.[200] Spectra collected at pH = 1–5 exhibit a shift in this peak because the iron speciation is strongly pH-dependent.[201] In the case of catechol, an initial green color was observed for the 1 : 2, 1 : 1 and 2 : 1 organic reactant : Fe molar ratios, which was attributed to the formation of a bidentate mononuclear catechol–Fe complex with an LMCT band around 700 nm.[202] The intensity of this feature varied with the amount of Fe in the solution mixture: the lowest intensity was observed for the 2 : 1 organic reactant : Fe solution mixtures. The intense spectral feature at 390 nm was attributed to n → π* transitions of *o*-quinone species formed from the oxidation of catechol–Fe complexes.[203] This peak was also observed at lower concentrations of catechol and iron under acidic conditions and for other catecholates such as gallic acid.[200] The presence of $-OCH_3$ group in the case of guaiacol inhibited the formation of the iron complex, as evident by the absence of the characteristic LMCT band in Fig. 6f. As explained below, the spectra in Fig. 6f indicated the formation of soluble amber-colored oxidation products due to iron redox chemistry.

The data in Fig. 6 clearly show the phase separation and solid particle formation in water. Fig. 7 shows scanning electron microscopy (SEM) images of the particles collected on the filters in Fig. 6. These images clearly show micron-size conglomerates of nanometer-size soot-like particles that we named 'fireless soot'. Energy dispersive X-ray spectroscopy (EDS) experiments showed that polycatechol and polyguaiacol particles are organic materials with no detectable iron content. The mass yield experiments using a 1 : 2 organic reactant : Fe molar ratio at pH 3 after 2 h of reaction were 47 ± 4% and 49 ± 14%, for polycatechol and polyguaiacol, respectively. These mass yield values were calculated using eqn (4):

$$\text{Yield } (\%) = \frac{\text{mass}_{\text{dried filter}} - \text{mass}_{\text{orginal filter}}}{\text{mass}_{\text{organic reactant}}} \times 100\% \qquad (4)$$

These mass yield values are comparable to or larger than the typical mass yields of SOA obtained by the photo-oxidation of

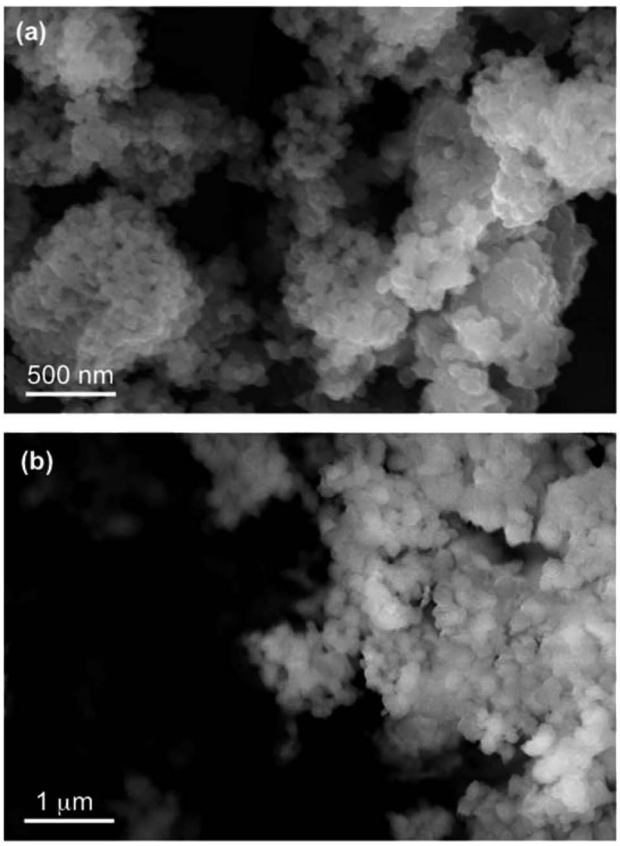

Fig. 7 SEM images of (a) polycatechol and (b) polyguaiacol collected on copper grids after a 90 min dark reaction of catechol with $FeCl_3$ at pH 3 in a 1 : 2 molar ratio. Reproduced from ref. 70 with permission from the American Chemical Society © 2015.

common VOCs, such as terpenes,[204] and are also larger than the yields associated with aqueous SOA (aqSOA) photochemical production.[205] Therefore, the iron-catalyzed reactions of catecholates have high potential to produce SOA with superior efficiency.

Using Matrix Assisted Laser Desorption Ionization Time-of-Flight Mass Spectrometry (MALDI-TOF-MS), Link *et al.*[206] explored the structure of a polycatechol thin film in the *m*/*z* range 200–450 (Fig. 8A). The MALDI mass spectrum in the *m*/*z* range 200–550 for a polyguaiacol thin film sample is shown for comparison in Fig. 8B. The tentative assignment of the peaks to chemical formulae and structures of oligomeric fragments is also shown in Fig. 8. While the peak pattern is complex, the highest intensities were associated with the trimer (around *m*/*z* 330 and 370) and the tetramer species (around *m*/*z* 430 and 490). Higher order oligomers, above *m*/*z* 450, were not reproducibly observed. In the following sections, a summary of previous studies is provided on the analysis of organic solvent extracts of polycatechol and polyguaiacol that contained oligomers with masses observed in the MALDI spectra. These structural details are useful when comparing the hygroscopic properties and ice nucleation activity of polycatechol and polyguaiacol with other organics.[73]

Moreover, Fig. 9 shows the attenuated total internal reflectance FTIR (ATR-FTIR) spectra of solid polycatechol and polyguaiacol formed in reactions of Fe(III) with catechol and guaiacol. The 2000–1000 cm^{-1} spectral range contains vibrations of aromatic (1640–1400 cm^{-1}), C–O and C–C stretching (1400–1200 cm^{-1}) and C–H bending (1200–1000 cm^{-1}) modes. The spectrum of polycatechol recorded by transmission FTIR using KBr pellets[209,210] is in line with the one shown in Fig. 9, where broadening and shift in peak frequencies were observed due to the rigid structure of polymers. The high intensity of features in the 1400–1200 cm^{-1} range is characteristic of phenylene (C–C) and oxyphenylene (C–O–C) linkages. These spectra show no absorbance around 1700 cm^{-1}, indicative of carbonyl (C=O) groups, which were reported for catechol and guaiacol SOA due to reaction with ozone.[155] The following sections highlight the effect of ring substituents in the benzene rings of catechol and guaiacol and competing ligands on the iron-catalyzed oxidative polymerization of catechol and guaiacol.

5.1.2 Derivatives of catechol and guaiacol. The reactions of Fe(III) with catechol and guaiacol derivatives were investigated by Chin *et al.*[190] to explore the effect of ring substituents on the polycatechol and polyguaiacol formation efficiency. These derivatives are listed in Table 1, which include 4-hydroxycatechol (4-HC), 3-hydroxycatechol (3-HC), coniferaldehyde (CON), 4-methylcatechol (4-MC), 4-nitrocatechol (4-NC) and 2,4-dinitrophenol (2,4-DNP).[68–70,211] Fig. 10A shows the UV-vis spectra of reaction mixtures as a function of time along with digital photographs of the reaction solutions. In these experiments, the concentration of soluble Fe(III) was less than or equal to 2 mM, which is a relevant choice for aerosol particles, as stated above. Fig. 10B shows digital photographs of the filters with insoluble products after 2 h of reaction time with CA, 3-HC, 4-HC, and CON. 3-HC and 4-HC are catechol derivatives with an extra hydroxyl group in the *para*- and *meta*-positions, respectively. The UV-vis spectra indicated the formation of quinone species between 350 and 400 nm. Both compounds formed colored particles with mass yields of 27 ± 2% and 32 ± 3% for 3-HC and 4-HC, respectively, after 2 h of reaction with Fe(III) at pH 3. The reaction of 4-MC and $FeCl_3$ did not produce particles over the 2 h reaction time. However, particles did eventually appear on the filter after allowing the mixture to react further for 24 h. On the other hand, the reaction of Fe(III) with 4-nitrocatechol and 2,4-dinitrophenol did not form particles.[190]

In the case of the guaiacol derivative, CON, particles formed after 2 h reaction with iron with a mass yield of 35 ± 4%. These differences in the reactivity of catechol and guaiacol derivatives with iron are discussed in the following sections. Syringol (SYR) is another guaiacol derivative, and its reactivity with iron was investigated by Lavi *et al.*[211]. They reported the formation of insoluble brown to black matter that was collected on a filter, washed and then completely dissolved in dimethyl sulfoxide (DMSO) and analyzed using UV-vis spectroscopy and liquid chromatography/mass spectrometry (see sections below for details). The insoluble matter was also analyzed using X-ray photoelectron spectroscopy (XPS), which showed that the surface chemical composition was predominately carbon (76–87%), as evidenced from the peaks of C=C or C–H, C–OH, and C=O functional groups. The atomic concentration of oxygen ranged from 13 to 24%. The following sections provide details

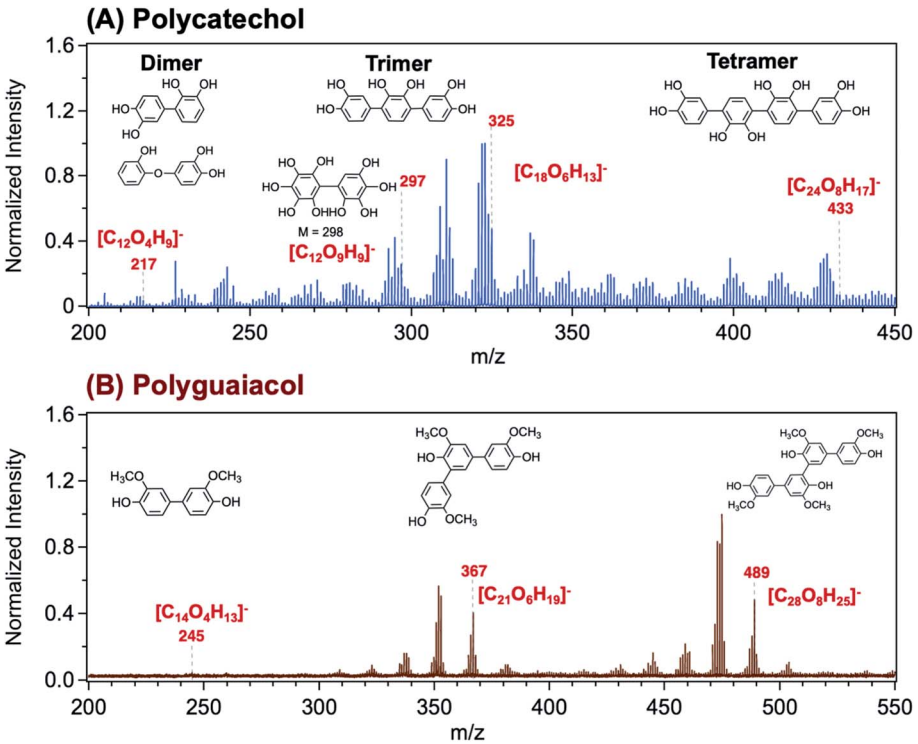

Fig. 8 Representative MALDI-TOF mass spectrum of (A) polycatechol and (B) polyguaiacol thin films in the negative ion reflector mode, $[M-H]^-$. The structure of fragments was based on ref. 207 for polycatechol and ref. 208 for polyguaiacol. No additional matrix compound was used in the spectra collection. Spectra were collected with the assistance of Dr Lauren T. Fleming, Prof. Sergey A. Nizkorodov, and Dr Ben Katz at the University of California Irvine Mass Spectrometry Facility.

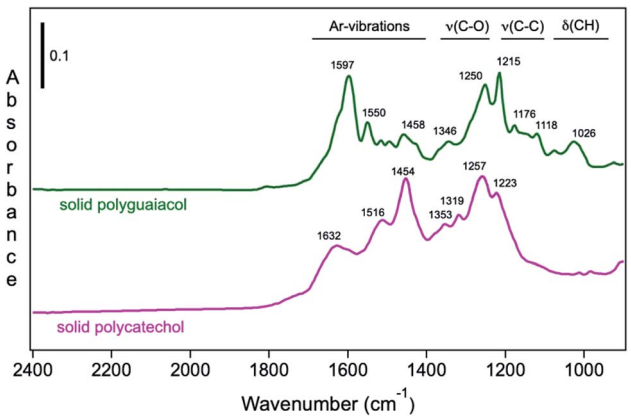

Fig. 9 ATR-FTIR absorbance spectra of (a) solid polycatechol (bottom) and polyguaiacol (top) deposited on a ZnSe ATR crystal from a water/ethanol slurry, followed by drying overnight. Reproduced from ref. 70 with permission from the American Chemical Society, © 2015.

on the mechanism that explains iron-catalyzed polymerization of phenolic compounds.

5.1.3 Mechanism of iron-catalyzed oxidative polymerization

5.1.3.1 Insoluble polycatechol formation. Abiotic oxidative polymerization of phenolic compounds is catalyzed by transition metals such as iron. Scheme 1 shows a proposed mechanism for polycatechol formation based on the results from ref. 212–216 under dark conditions leading to the formation of oligomers and polymeric particles. Iron catalyzes the deprotonation of catechol and its derivatives below their first pK_a[198] and forms strong bidentate complexes with stability constants that vary with iron species in solution. For example, the formation of $Fe(C_6O_2H_4)^+$ as per eqn (5) and (6) has log K values of 7.9 and 9.9 depending on the iron species:

$$Fe^{3+} + H(C_6O_2H_4)^- \rightleftharpoons Fe(C_6O_2H_4)^+ + H^+ \quad (5)$$

$$FeOH^{2+} + H(C_6O_2H_4)^- \rightleftharpoons Fe(C_6O_2H_4)^+ + H_2O \quad (6)$$

The extent of charge transfer that oxidizes the organic compound and reduces Fe(III) depends on the benzene ring substituents. In this mechanism, dissolved O_2 is the oxidant and Fe(III) plays a role as a catalyst. Tran *et al.*[69] investigated the effect of dissolved oxygen in aqueous solutions containing iron under acidic conditions. The level of dissolved O_2 in these experiments was quantified at 11 ± 2 mg L^{-1} (or ppm). Bubbling N_2 gas into the reactant solutions (prior to mixing) for 1 h reduced the level of dissolved O_2 to 3 ± 2 ppm. Longer bubbling times up to 2 h did not significantly reduce this value further. So, we concluded that it is practically impossible to completely purge dissolved oxygen by nitrogen bubbling, and that the amount of dissolved oxygen below the detection limit of the measuring electrode is enough to oxidize polyphenols in the presence of iron.

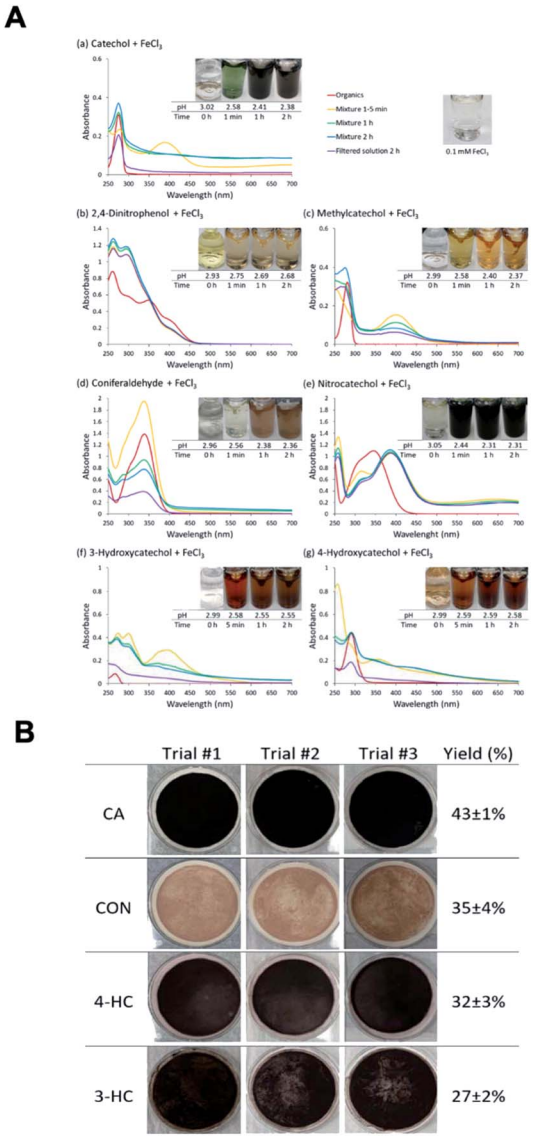

Fig. 10 (A) UV-vis absorption spectra of mixtures of Fe(III) with (a) CA, (b) 2,4-DNP, (c) 4-MC, (d) CON, (e) 4-NC, (f) 3-HC, and (g) 4-HC. Different colors of traces correspond to spectra of organic reactants before mixing (red), 1–5 min after mixing (orange), 1 h after mixing (green), 2 h after mixing (blue), and filtered solution (purple). The final concentration of organics is 1 mM, and the final concentration of Fe(III) is 2 mM. The photographs are those of unfiltered solutions. (B) Photographs of filters containing particles after 2 h of reaction, filtration, and drying for CA, CON, 4-HC, and 3-HC. The last column contains the average ($n = 3$) effective mass yield in percent. Reproduced from ref. 190 under Create Commons License (CC BY-NC) from the Royal Society of Chemistry, © The Author(s), 2021.

Cycling between Fe(II) and Fe(III) species is coupled with the production of ROS, H_2O_2, and OH radicals as intermediates.[217] The LMCT steps lead to the formation of quinone species and the release of Fe(II). Oxidation of Fe(II) to Fe(III) by dissolved oxygen is spontaneous according to reactions (7)–(9):

$$\mathrm{Fe(II)} \rightarrow \mathrm{Fe(III)} + \mathrm{e},\ E_{ox} = -0.75\ \mathrm{V} \quad (7)$$

$$\mathrm{O_2(g)} + 2\mathrm{H^+} + 2\mathrm{e} \rightarrow \mathrm{H_2O_2(l)},\ E_{red} = +0.7\ \mathrm{V} \quad (8)$$

Net reaction:

$$\mathrm{Fe(II)} + 2\mathrm{H^+} + \mathrm{O_2(g)} \rightarrow \mathrm{Fe(III)} + \mathrm{H_2O_2(l)},\ E_{net} = E_{red} - E_{ox} = +1.45\ \mathrm{V} \quad (9)$$

The rate constant for the net spontaneous oxidation of Fe(II) by dissolved oxygen is pH-dependent and is known up to pH 6.[218] Another pH-dependent reaction of Fe(II) with O_2(g) produces the superoxide anion, $O_2^{\bullet -}$, according to:

$$\mathrm{Fe(II)} + \mathrm{O_2(g)} \rightarrow \mathrm{Fe(III)} + \mathrm{O_2^{\bullet -}},\ k = 10^7\ \mathrm{M^{-1}\ s^{-1}}\ \text{(ref. 119)} \quad (10)$$

The pK_a of the superoxide is 4.8 and its protonated form is $HO_2^{\bullet}$.[219] Under excess Fe(III), the formation with H_2O_2 or $HO_2^{\bullet}/O_2^{\bullet -}$ from the above reactions occur according to eqn (11) and (12):

$$\mathrm{Fe(III)} + \mathrm{H_2O_2(l)} \rightarrow \mathrm{Fe(II)} + \mathrm{HO_2^{\bullet}/O_2^{\bullet -}} + \mathrm{H^+},\ k = 2 \times 10^{-3}\ \mathrm{M^{-1}\ s^{-1}}\ \text{(ref. 220)} \quad (11)$$

$$\mathrm{Fe(III)} + \mathrm{HO_2^{\bullet}/O_2^{\bullet -}} \rightarrow \mathrm{Fe(II)} + \mathrm{O_2} + \mathrm{H^+},\ k = 7.8 \times 10^5\ \mathrm{M^{-1}\ s^{-1}}\ \text{(ref. 220)} \quad (12)$$

The *in situ* formation of Fe(II) and H_2O_2 would lead to the OH radical production per the Fenton reaction shown in eqn (13) under acidic conditions:

$$\mathrm{Fe(II)} + \mathrm{H_2O_2(l)} \rightarrow \mathrm{Fe(III)} + \mathrm{OH} + \mathrm{OH^-},\ k = 55\ \mathrm{M^{-1}\ s^{-1}}\ \text{(ref. 220)} \quad (13)$$

The rate of the Fenton reaction is pH-dependent, and the relative importance of the different elementary steps varies with the relative amounts of Fe(II) and H_2O_2 in solution.[221] The OH radical in the presence of quinone and catechol species leads to hydroxylation of the benzene rings forming oligomers and eventually polycatechol. The formation of polycatechol in solution falls under the category of 'mechanisms for polymerization reactions', which are composed of three main steps: initiation, propagation and termination.[222] The OH radical plays a role in the first and second steps. Under conditions characteristic of viscous multicomponent aerosol systems with relatively high ionic strength (I = 1–12 m) and acidic pH (~2) that likely affected the kinetics of the polymerization reactions, Al-Abadleh *et al.*[148] detected colored water-soluble oligomers shown in Scheme 2 using ultrahigh pressure liquid chromatography coupled with mass spectrometry (UHPLC-MS).

5.1.3.2 Insoluble polyguaiacol formation. Scheme 3 shows the mechanism of guaiacol oxidation in the presence of excess iron under dark conditions based on reported mechanisms in ref. 223 and 224. Previous studies[208,224,225] on the guaiacol reaction with transition metals including iron reported the characterization of the soluble products from the oxidation process. The established mechanism that explains these results is mainly carbon–carbon coupling of guaiacoxy radicals, with little evidence for carbon–oxygen coupling,[208,224] leading to the formation of dimers and eventually polyguaiacol. Pillar *et al.*[207]

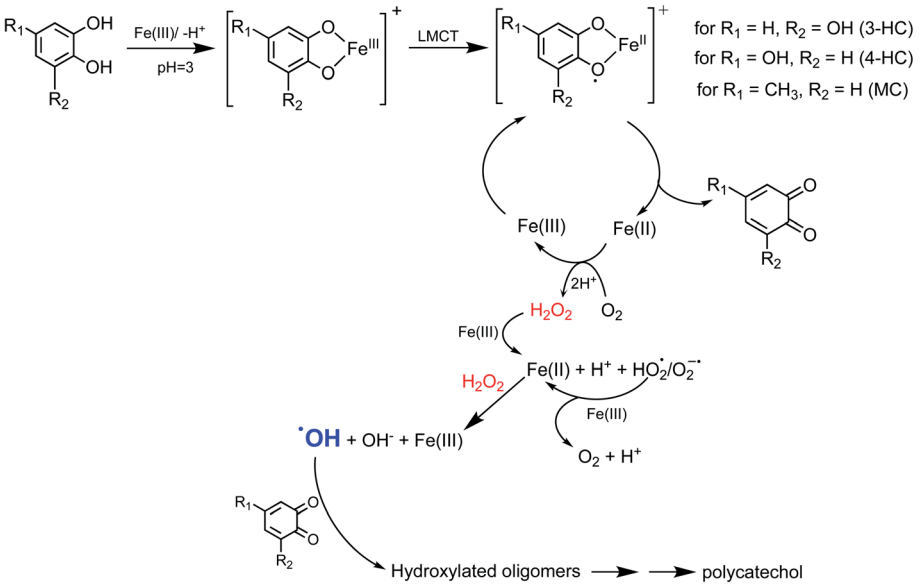

Scheme 1 Suggested mechanism for polycatechol formation. Reproduced from ref. 190 under Create Commons License (CC BY-NC) from the Royal Society of Chemistry, © The Author(s), 2021.

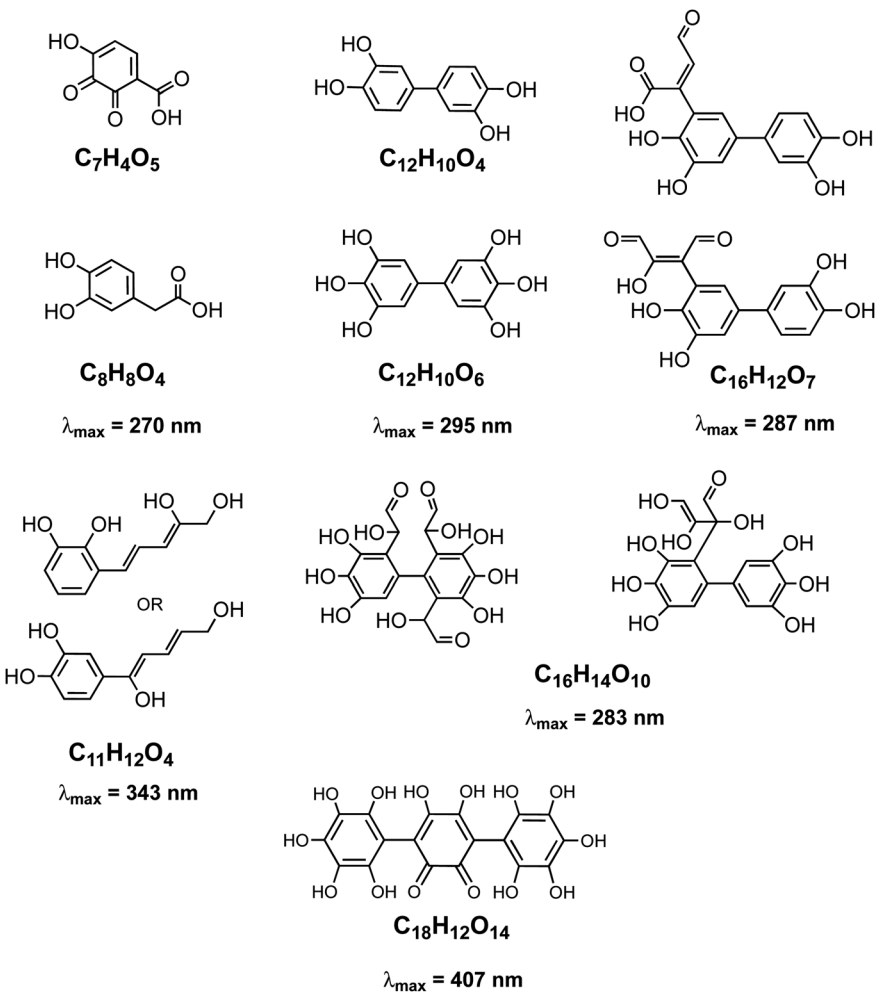

Scheme 2 Structure of molecules and oligomers and their characteristic absorption wavelength detected in the reaction of catechol with Fe(III) under conditions characteristic of viscous multicomponent aerosol systems with relatively high ionic strength (I = 1–12 m) and acidic pH (~2) using UHPLC-MS. Modified from ref. 148 with permission from The American Chemical Society, © 2021.

observed dimers and trimers in the electrospray ionization mass spectra of organic solvent extracts of soluble products from the heterogeneous ozonolysis of catechol thin films. Using a combination of HPLC, ^{1}H NMR, fast atom bombardment, and chemical ionization mass spectrometry, Schmalzl *et al.*[208] studied the reaction of guaiacol with $FeCl_3$ and reported the elemental composition, retention times, characteristic chemical shifts and masses of guaiacol oligomers ranging from dimers to pentamers at 246, 368, 490 and 612 mass units. They assigned the 470 nm peak to an unstable 4,4′-diphenoquinone intermediate.[208] These oligomers formed a precipitate soluble in organic solvents and were found to be mainly organic in composition. Similar oligomers – up to trimers – were observed in the mass spectra of reaction products from the enzymatic oxidation of guaiacol.[224,225] Hwang *et al.*[224] identified products from the biochemical oxidation of guaiacol by manganese peroxidase (MnP) in the presence of H_2O_2 by a suite of analytical techniques and reported the structure of the dimers shown in Scheme 3. Lavi *et al.*[211] characterized oligomeric products solubilized in DMSO using a HPLC/PDA/ESI-HRMS platform from the reaction of Fe(III) with guaiacol. Fig. 11 shows the chromatogram of the reaction products and their characteristic UV-visible absorption spectra in 300–700 nm. The fragments observed were assigned to trimers and tetramers.

Hence, based on the above, *in situ* reduction of Fe(III) to Fe(II) leads to the formation of phenoxy radicals, which proceeds

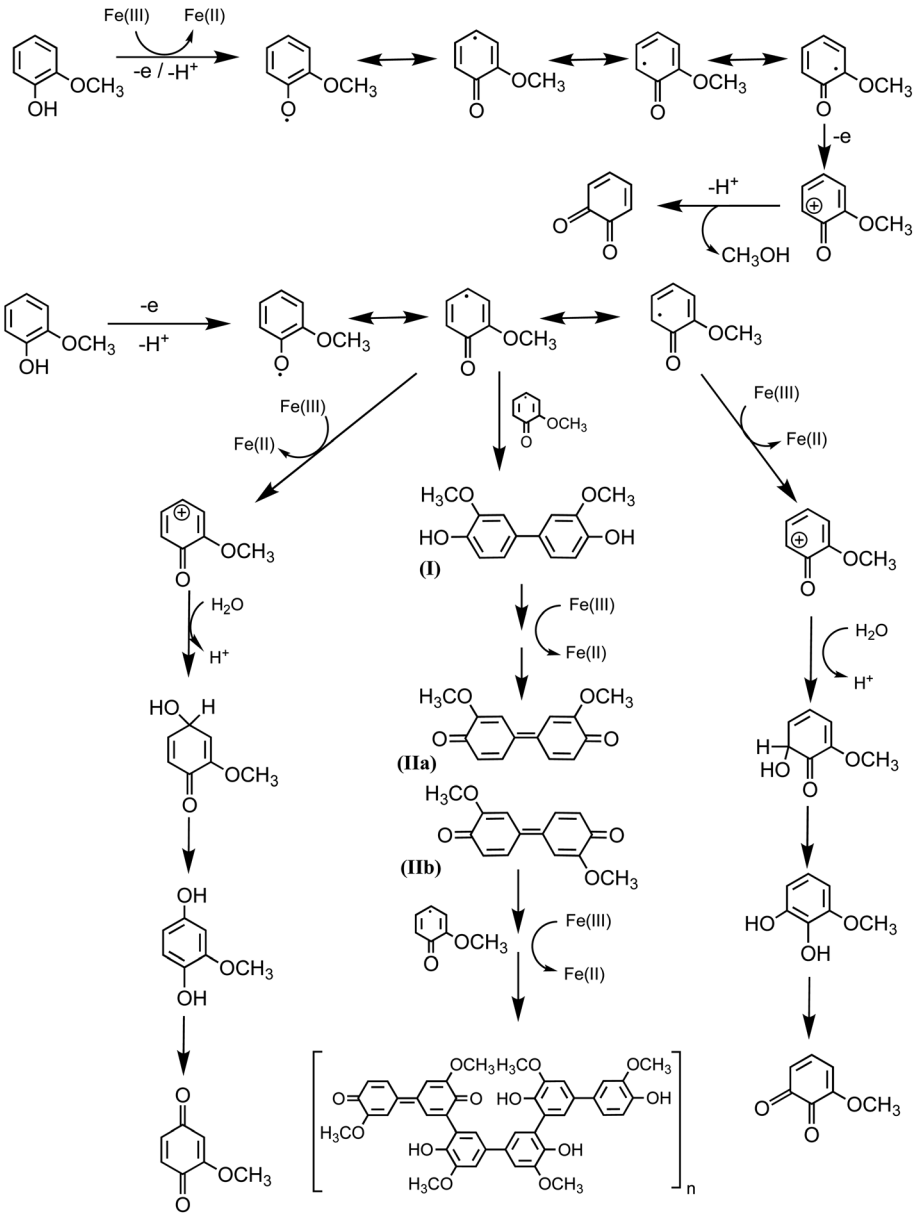

Scheme 3 Mechanism for the oxidation of guaiacol in the presence of excess iron under dark conditions leading to the formation of dimers and eventually polyguaiacol based on the mechanism reported in ref. 223 and 224. Reproduced from ref. 190 under Create Commons License (CC BY-NC) from the Royal Society of Chemistry, © The Author(s), 2021.

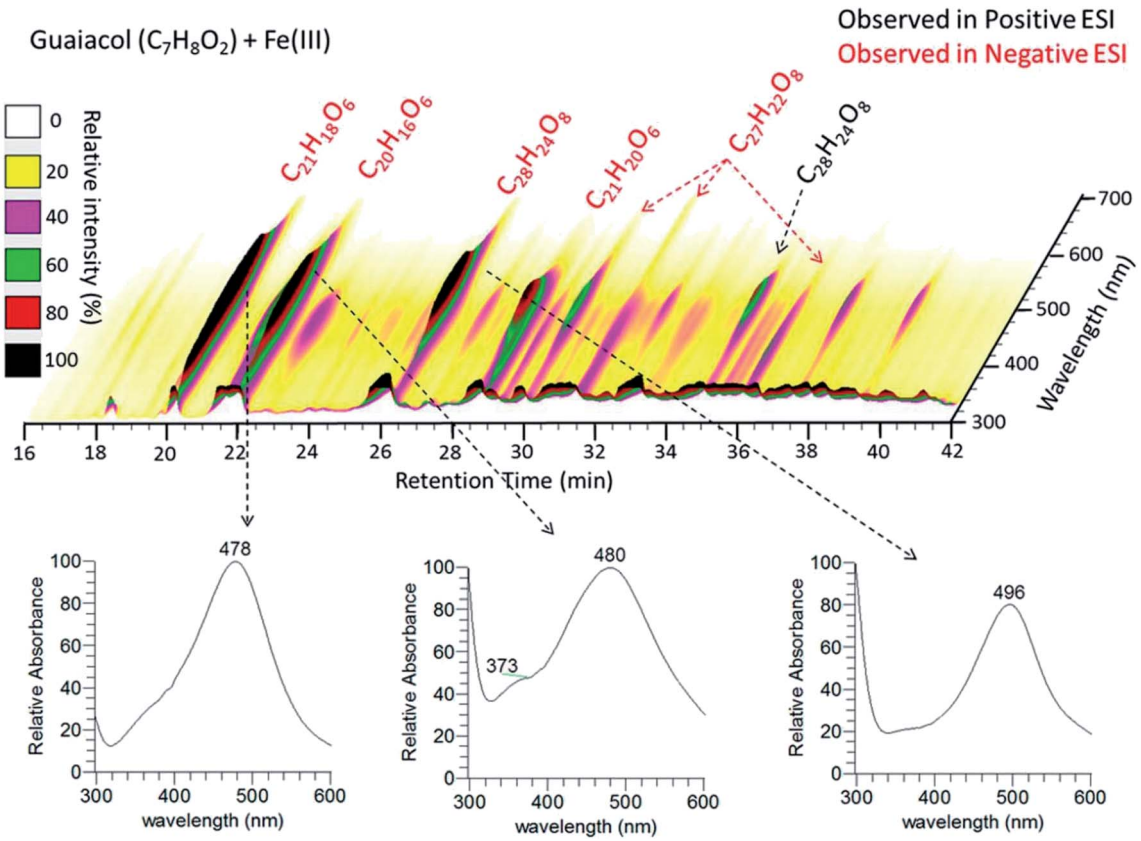

Fig. 11 (Upper panel) HPLC/PDA chromatogram of guaiacol/Fe(III) reaction products. The *x*-axis is the retention time, the *y*-axis is the UV-vis absorption wavelength, and color denotes the intensity of the absorption signal. (Lower panels) UV-visible spectra of selected chromophores. The figure and the caption were reproduced from ref. 211 with permission from the American Chemical Society, © 2017.

through C–C radical coupling from compound I in Scheme 3. Compounds IIa and IIb (Scheme 3) give rise to the spectral features at 412 and 470 nm (Fig. 6f), which were observed to decrease in intensity upon overnight storage of solutions.[224,225] As detailed below, formation of these polymeric species has implications on the overall optical properties and chemical reactivity of the surfaces coated by these products.

5.1.4 Effect of competing ligands on the polycatechol and polyguaiacol formation efficiency

5.1.4.1 Oxalate. Oxalic acid (pK_a 1.3 and 3.8)[170] is a ubiquitous component and the most abundant dicarboxylic acid in ambient aerosols with a high complexation affinity to iron. The work by Kundu *et al.*[163] on biomass burning aerosols showed that 77% of oxalic acid is formed from the degradation of dicarboxylic acids and related compounds, and 23% are likely directly emitted or chemically produced from other unknown precursors. Other well-studied mechanism of oxalate formation in atmospheric aqueous particles is the oxidation of glyoxal and methylglyoxal.[226] Recently, Zhang *et al.*[227] reported results from field measurements, showing enhanced formation of oxalate associated with iron-containing particles. They attributed this observation to the complexation of oxalate to iron following gas–particle partitioning of oxalic acid. In general, aqueous phase oxalate is the most effective organic compound among the known atmospheric organic ligands that promotes dust iron solubility.[132]

The thermodynamic stability constants of iron oxalate complexes were calculated using Visual MINTEQ software and found to vary with pH (Fig. 5b and c). In the pH range 2–3, the dominant iron species are Fe^{3+} and $FeOH^{2+}$, which complex with hydrogen oxalate, $HC_2O_4^-$, according to eqn (14) and (15):

$$FeOH^{2+} + HC_2O_4^- \rightleftharpoons Fe(C_2O_4)^+ + H_2O,\ \log K = 6.9 \quad (14)$$

$$Fe^{3+} + HC_2O_4^- \rightleftharpoons Fe(C_2O_4)^+ + H^+,\ \log K = 4.9 \quad (15)$$

In excess oxalate at pH 3, the following reactions also take place since a maximum of three oxalate molecules can complex with a single iron centre:

$$FeOH^{2+} + 2HC_2O_4^- \rightleftharpoons Fe(C_2O_4)_2^- + H_2O + H^+,\ \log K = 8.9 \quad (16)$$

$$FeOH^{2+} + 3HC_2O_4^- \rightleftharpoons Fe(C_2O_4)_3^{3-} + H_2O + 2H^+,\ \log K = 8.9 \quad (17)$$

$$Fe^{3+} + 2HC_2O_4^- \rightleftharpoons Fe(C_2O_4)_2^- + 2H^+,\ \log K = 6.9 \quad (18)$$

$$Fe^{3+} + 3HC_2O_4^- \rightleftharpoons Fe(C_2O_4)_3^{3-} + 3H^+,\ \log K = 6.9 \quad (19)$$

The left panel in Fig. 12 shows the effect of varying the amounts of oxalate, catechol and guaiacol on the mass of the insoluble product following 2 h reaction of these ligands with iron under dark conditions at pH 3.[68] In the presence of equimolar amounts of oxalate and catechol, no suppression of particle formation was observed relative to the control experiments (absence of oxalate and sulfate), which corresponds to mass yields of ~50% and 60% for polycatechol and polyguaiacol, respectively. The data also show a larger reduction in particle mass with guaiacol than catechol. Suppression of particle formation was observed with excess oxalate (left side of 2 : 1 : 1 Fe : catechol : Ox molar ratio, Fig. 12a). This suppression is explained by the predominance of soluble iron oxalate complexes, $Fe(C_2O_4)_2^-$ and $Fe(C_2O_4)_3^{3-}$. The log K values for the formation of both complexes equal 8.9 with $FeOH^{2+}$ species, which is much higher than that for the ligand exchange between catecholate, $H(C_6O_2H_4)^-$, and $Fe(C_2O_4)_2^-$ or $Fe(C_2O_4)_3^{3-}$ ($\log K = 1$). Particle mass is also lower in the 1 : 1 : 1 Fe : catechol : Ox molar ratio (right side of 2 : 1 : 1, Fig. 12a). This observation is explained by the reduction in the rate of the oxidative polymerization reaction when iron is the limiting reagent relative to catechol, as highlighted in the above section Mechanism of iron-catalyzed oxidative polymerization.

The time-dependent average particle size of polymeric particles produced *in situ* from the reaction of Fe(III) with aromatic reagents in the presence or absence of oxalate (and sulfate) in solution is shown in Fig. 13. Within the first 20 min, adding oxalate and sulfate leads to the formation of polycatechol particles in solution that are 2 and 2.5 times larger than those from control experiments, respectively (Fig. 13a). In light of the product mass yields obtained from filter weighing, one can take the interpretation of the DLS measurements further. For example, since the 2 : 1 : 1 Fe : catechol : Ox or AS reaction produces the same product mass as 2 : 1 Fe : catechol control (Fig. 12a and b), but the particles are initially larger (Fig. 13a), there must be fewer of them in the solution. This could indicate that the initial solution nucleation is retarded by oxalate, but once particles form they grow faster. When the reaction is carried out according to method 2 using sulfate (defined in the caption of Fig. 13), the DLS measurements show micron-size particles forming right away (Fig. 13a) with polydispersity index (PDI) above 0.5, indicating their high degree of polydispersity. As detailed above, the product mass from this reaction is double the control value at pH 3 (Fig. 12a). Hence, these combined results suggest the formation of larger and heavier particles in solution when iron sulfate is reacted with catechol according to method 2.

In the case of guaiacol, particles produced according to method 1 (defined in the caption of Fig. 13) at pH 3 show no significant difference in size when oxalate (or sulfate) was added relative to the control (Fig. 13b). These conditions produce less product mass than the control per data in Fig. 12b. However, the cases that produced twice the product mass when sulfate was added according to method 2 at pH 5 and 3 resulted in higher variability in particle size within the first 40 min of reaction time. Similar to the results with catechol, these particles have a PDI above 0.5, indicating their high degree of polydispersity. When these results are combined with product mass results, they suggest the formation of fewer and heavier particles in solution when iron sulfate was reacted with guaiacol according to method 2. This method is more atmospherically relevant over a range of multicomponent aerosol processing than method 1.

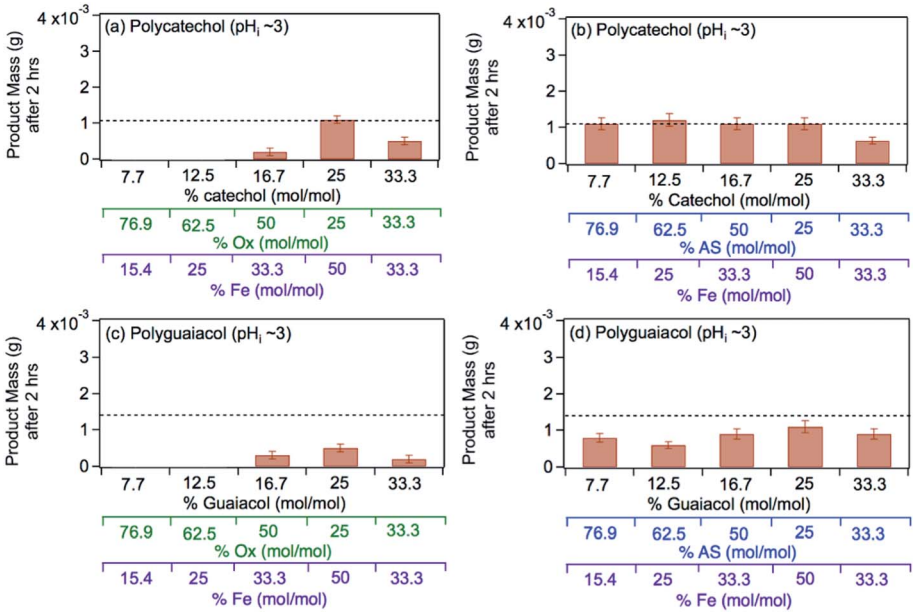

Fig. 12 Effect of adding oxalate (Ox, left) and ammonium sulfate (AS, right) on product mass after 2 h of dark aqueous phase reaction of 1 mM catechol and guaiacol with $FeCl_3$ (total volume = 20 mL). The error bars represent the standard deviation ($\pm\sigma$) from averaging 3–4 filter weight values. The horizontal dashed line is the product mass for the control reaction (no added oxalate or sulfate) for 2 : 1 Fe : organic molar ratio. The figure and the caption were modified from ref. 68 with permission from the American Chemical Society, © 2019.

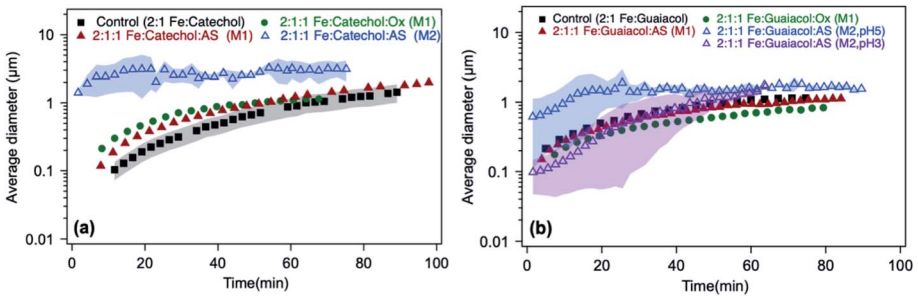

Fig. 13 Effect of adding oxalate (Ox) and ammonium sulfate (AS) on particle size from time-dependent DLS measurements during the dark aqueous phase reaction of (a) catechol (1 mM) and (b) guaiacol (0.5 mM). This molar ratio results in the maximum product mass per data shown in Fig. 1. 'M1' stands for method 1, where organic reagents were mixed first with AS or Ox, then the reaction time started when Fe was added. 'M2' stands for method 2, where AS or Ox were reacted first with Fe for 2 h, then the reaction time started when the organic reagent was added. The shaded areas represent the standard deviation of three trials. Unshaded data represent the average of two trials, with a standard deviation the size of the marker width (15%). The figure and the caption were modified from ref. 68 with permission from the American Chemical Society, © 2019.

The results described above show a new role for oxalate in aerosol chemistry, given its higher concentrations than iron and organic reagents, which is to efficiently suppress secondary particle formation in solution.

5.1.4.2 Sulfate. Sulfate is one of the most abundant inorganic components in aerosol particles that is mainly formed from aqueous phase oxidation of SO_2, a process often catalyzed by soluble iron.[117] Sulfate is routinely measured and incorporated in thermodynamic models that calculate the aerosol pH.[228] Yu *et al.*[229] reported a correlation between the sulfate and oxalate contents in particles and suggested a dominant in-cloud processing pathway to explain the close tracking of both species. Non-sea salt sulfate (nss SO_4^{2-}) from anthropogenic sources were also reported to largely control the formation of water soluble SOA dominated by oxalate *via* aqueous phase photochemical reactions.[230]

The thermodynamic stability constants of iron sulfate complexes were calculated using Visual MINTEQ software and found to vary with pH (Fig. 5d and e). In the pH range 2–3, the dominant iron species are Fe^{3+} and $FeOH^{2+}$, which complex with sulfate, SO_4^{2-}, according to eqn (20) and (21):

$$FeOH^{2+} + SO_4^{2-} + H^+ \rightleftharpoons FeSO_4^+ + H_2O,\ \log K = 6.3 \quad (20)$$

$$Fe^{3+} + SO_4^{2-} \rightleftharpoons FeSO_4^+,\ \log K = 4.3 \quad (21)$$

In excess sulfate at pH 3, the following reactions also take place since a maximum of two sulfate molecules can complex with a single iron centre:

$$FeOH^{2+} + 2SO_4^{2-} + H^+ \rightleftharpoons Fe(SO_4)_2^- + H_2O,\ \log K = 7.4 \quad (22)$$

$$Fe^{3+} + 2SO_4^{2-} \rightleftharpoons Fe(SO_4)_2^-,\ \log K = 5.4 \quad (23)$$

The above $\log K$ values for the formation of soluble iron sulfate are lower than those for iron catecholate, $Fe(C_6O_2H_4)^+$ (9.9, reactions (5) and (6). These $\log K$ values explain the trend in product mass in Fig. 12b, where adding sulfate had no effect on particle formation in solution because $[FeOH]^{2+}$ species are still the dominant species in solution (Fig. 5d and e). Under excess sulfate, an increase in the concentration of $[FeSO_4]^+$ relative to $[FeOH]^{2+}$ species is observed at pH 3 (Fig. 5e). Data in Fig. 12b show that the product mass nearly doubled when the reaction resulting in the 2 : 1 : 1 Fe : catechol : AS molar ratio was carried out at pH 3 according to method 2 (*i.e.*, catecholate reacts with iron sulfate complexes). Ligand exchange between catecholate and iron sulfate complexes is favorable with $\log K = 3.6$, according to reaction (24):

$$H(C_6O_2H_4)^- + FeSO_4^+ \rightleftharpoons SO_4^{2-} + Fe(C_6O_2H_4)^+ + H^+,\ \log K = 3.6 \quad (24)$$

Ion chromatography (IC) analysis showed a 34% reduction in the solution concentration of sulfate following polycatechol formation in solution according to method 2, where AS was reacted first with Fe for 2 h, then the reaction time started when catechol was added. This observation was interpreted to mean that sulfate was trapped within the insoluble polycatechol particles based on the DLS measurements in Fig. 13a discussed above. Particle characterization using ATR-FTIR and combined thermal gravimetric analysis and differential scanning calorimetry (TGA/DSC) also confirmed this interpretation.[68] Similar observations were reported for polyguaiacol particles formed in the presence of sulfate. The TGA/DSC analysis also revealed that it is very likely that the polycatechol particles formed in the presence of sulfate are porous and can retain sulfate anions. In the case of polyguaiacol particles, their higher molecular weight and therefore higher viscosity[231] helps retain sulfate. This sulfate retention in polycatechol and polyguaiacol appears to take place during particle growth and hence contributes to their polydispersity and size observed in the DLS curves in Fig. 13. The trapping of sulfate in the organic polymers studied here might result in changing their hygroscopic properties, water uptake behavior (described below), and their chemical/photochemical reactivities.

5.1.5 Effect of light on the polycatechol formation efficiency. The effect of near-UV radiation on soluble Fe(III) reactions with catechol was examined to highlight the contrast in aqueous phase iron chemistry with atmospherically relevant organic compounds under dark *versus* irradiation

conditions[56,118,232–234] (*i.e.*, night *versus* daytime). In these experiments, Chin *et al.*[190] used UV radiation at 405 nm because oxidation species of the Fe–catechol complex has a strong absorption band at 400 nm. The radiation was produced by a light-emitting diode (LED, M405L4, Thorlabs) with a center wavelength of 405 ± 7 nm (the quoted range refers to full width at half maximum). Two different intensities of the UV light were tested: one with the maximal LED output (~135 mW) and another with the LED power set to 50% of the maximal value (~70 mW). The hypothesis tested was whether 405 nm irradiation can suppress the Fe(III)-catalyzed oligomerization reactions in the catechol + Fe(III) system. The overall scattering due to suspended particles reduced as the UV intensity increased (Fig. 14A), and the measured particle yields dropped from 43 ± 2% at 0 mW to 32 ± 6% at 70 mW and to 28 ± 2% at 135 mW (Fig. 14B). In systems, containing guaiacol, Pang *et al.*[234] found a strong effect of UV irradiation on chemistry in the Fe(III)–oxalate–guaiacol aqueous mixtures. The results suggested that photodegradation counteracted the polymerization. Indeed, it was reported that catechol photodegrades under UV irradiation in the presence of O_2.[235] In an oxidative environment, the easily produced radical caused by irradiation is the main reason for degradation.[235,236] Nevertheless, the photodegradation was not sufficiently fast to prevent particle formation, suggesting that the chemistry studied here will occur under both dark and sunlit conditions.

In summary, polycatechol and polyguaiacol formation is efficient under dark and light conditions using millimolar concentrations of Fe(III) and organic reactants, which may be attainable on surfaces of particles or in aerosol liquid water. As stated earlier, the concentrations of these reactants are lower in cloud and fog droplets, making the extrapolation of the above results not straightforward.

5.1.6 Effect of ionic strength and viscosity on polycatechol formation under acidic conditions. A number of factors affect the rate of reactions in atmospheric cloud/fog droplets and deliquescent aerosol systems containing Fe(II)/Fe(III) species. These factors include the concentration of reactants, pH, and ionic strength (I), which are chiefly dependent on the aerosol liquid water. As stated earlier and in the following sections, the amount of aerosol liquid water in atmospheric particles is a function of temperature, RH, and chemical composition (inorganic *vs.* organic).[237,238] The aqueous phase volume in cloud/fog droplets is about 10^{-1} cm^3 m^{-3} with pH values in the range of 2–7 and I of 10^{-4} M, compared to ~10^{-6} cm^3 m^{-3} in deliquescent aerosols with pH values below 2 and I > 6 M depending on the source location (*e.g.*, marine, urban, or continental).[66] These values are largely controlled by the inorganic salt content of atmospheric droplets/aerosols. The organic content in atmospheric particles is characterized by a number of functional groups with the oxygen-to-carbon elemental ratio (O : C) in the range of 0.1–1.0.[35] The uptake of VOCs from biogenic and anthropogenic sources, gas and particle phase oxidation reactions can produce low-volatility products leading to the mixing of organic species with inorganic salts.[35]

Iron-catalyzed polymerization of catechol was investigated[148] under conditions characteristic of relatively viscous multicomponent aerosol systems and adsorbed water[70] with high ionic strength (I = 1–12 m), acidic pH (~2),[66,237,239] and low water

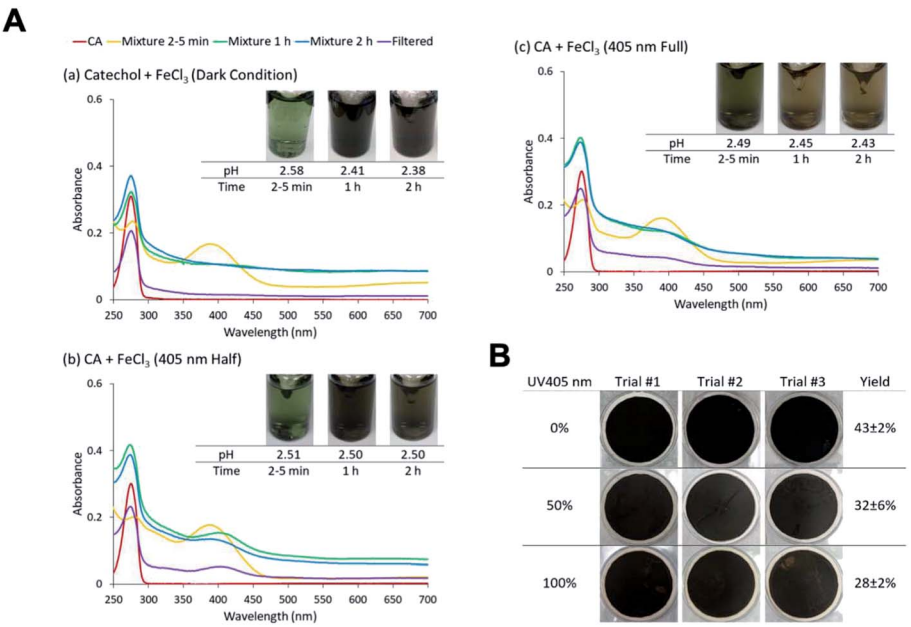

Fig. 14 (A) Effect of 405 nm irradiation on particle formation of CA and Fe(III) at different levels of UV LED intensities (0%, 50%, and 100%). Different colors of traces correspond to the spectra of CA before mixing (red), 2–5 min after mixing (orange), 1 h after mixing (green), 2 h after mixing (blue), and filtered solution (purple). (B) Photographs of filters containing particles after 2 h of reaction, filtration, and drying for pyrocatechol (CA) under different intensities of 405 nm UV irradiation. The last column contains the average (n = 3) effective mass yield in percent. Reproduced from ref. 190 under Create Commons License (CC BY-NC) from the Royal Society of Chemistry, © The Author(s), 2021.

Table 6 Chemical composition and physical properties of background solutions for the reaction between iron chloride and catechol using ammonium sulfate (AS) as salt. Reproduced from ref. 148 with permission from the American Chemical Society, © 2021

Rxn no.	[Salt] (M)	[Org] (M)	Ionic strng.[a] (m)	Soln. density[b] (gmL^{-1})	Soln. viscosity[c] (mPa s)	pH	Water activity[d] (%RH)	Org : AS mass ratio	%[Fe–CA][e]
AS only (no added organics)									
1	0.01	—	0.015	1.0 ± 0.1	—	2.2	0.99	—	1.2
2	1	—	2.2	1.1 ± 0.1	—	2.6	0.97	—	0.33
3	2	—	4.4	1.2 ± 0.1	—	2.5	0.95	—	0.12
M1 + AS									
4	1	SA, 0.2	2.2	1.1 ± 0.1	—	2.7	0.97	0.2	0.34
5	2	SA, 0.2	4.3	1.2 ± 0.1	—	2.6	0.94	0.1	0.16
6*	1	MA, 2	2.2	1.2 ± 0.1	—	2.1	0.93	2.1	0
7	2	MA, 1	4.4	1.2 ± 0.1	—	2.6	0.92	0.5	0
8	1	GA, 2	2.2	1.1 ± 0.1	—	2.5	0.95	2.1	0.028
9	2	GA, 1	4.4	1.2 ± 0.1	—	2.6	0.93	0.5	0.054
M2 + AS									
10*	2.9	SA, 0.17 GA, 4.4	5.8	1.2 ± 0.1	2445 ± 40	2.1	0.89	1.6	0.015
11*	2.6	SA, 0.28 Mal, 4.6	5.4	1.3 ± 0.1	2445 ± 40	2.2	0.88	1.5	0
M3 + AS									
12	4.4	SA, 0.4 MA, 4.9 GA, 1.6	7.9	1.3 ± 0.1	3014 ± 344	2.1	0.81	1.6	0

[a] Calculated using $I = 1/2\sum_{1}^{i} C_i z_i^2$, where C_i is the concentration of charged species in solution in molality (m) calculated using Visual MINTEQ[182] for each solution. [b] Calculated from the mass of a known volume. [c] Measured in this study using a viscometer for low viscosity fluids. The '—' indicates instrument was not accurate in measuring viscosity using water-like fluids around 1 mPa s. [d] Calculated using E-AIM, Model IV, aqueous solutions. [e] Calculated using Visual MINTEQ for each solution relative to total Fe(III) aqueous species in solution. Abbreviations are: Rxn = reaction, AS = ammonium sulfate, Org = organic compound, SA = succinic acid, MA = malic acid, GA = glutaric acid, and Mal = malonic acid. M1–3 refer to the number of organic compounds in the solution per the terminology used by Marcolli *et al.*[180] The concentrations are in the final solutions after mixing. All solutions contained final concentrations of 2×10^{-3} and 1×10^{-3} M of Fe(III) and catechol, respectively. The final solution volume of Rxn no. 1–8 was 20 mL and of Rxn no. 9–11 was 5 mL. The '*' marks the reactions that were analyzed using UHPLC-UV-MS after filtration.

activity (0.6–0.97)[240] for comparison with earlier studies completed under conditions typical for cloud chemistry (I = 0.01 M, pH 3–5).[68,70] To vary the pH, I, and water activity, the background aqueous phase solutions were prepared by adding either ammonium sulfate (AS) or ammonium nitrate (AN), and ubiquitous C3–C5 dicarboxylic acids (malonic, malic, succinic, and glutaric acids) were detected in biomass burning aerosols[163] and used in laboratory studies for investigating the liquid–liquid phase separation.[35] The relative amounts of the organic (Org) and inorganic (Inorg) components were varied to achieve mass ratios reported for field aerosols, Org : Inorg = 0.2–3.5.[35] These salts and diacids also competed for binding to iron, specifically the anionic species,[169] forming soluble iron complexes. For example, Table 6 lists the reaction numbers and the composition of the background solutions using ammonium sulfate (AS). The concentration of chemicals was chosen to achieve an Org : Inorg (AS or AN) mass ratio between 0.5 and 2. This mass ratio range was measured in field-collected organic aerosols from the pristine Amazon Basin[241] and many locations in the Northern Hemisphere.[242,243] The diacids chosen for this study have an O : C molar ratio greater than or equal to 0.8. Previous work on aerosol systems containing organics with this molar ratio range showed no liquid–liquid phase separation as a function of the Org : AS mass ratio range used here.[244] Instead, deliquescence (D) and efflorescence (E) were observed in these systems with DRH and ERH ranging from 45–80 and 10–35%, respectively.[244] The calculated water activity in the solutions in Table 6 ranges from 0.81 to 0.99 and that using AN ranges from 0.68 to 0.99, hence covering a relatively wide range of aerosol liquid water.

Fig. 15A shows digital photos of particles on filters and filtrate solutions from the reaction of catechol with Fe(III) as a function of O : C molar ratio in the background solutions listed in Table 6. For comparison, images for the control reactions in the absence of catechol are shown in Fig. 15B. These qualitative results clearly show that the insoluble black particles and brownish soluble reaction products originated from catechol. Also, the type of the diacid and its concentration relative to AS in the background solutions affected the particle density after 24 h of reaction time, as inferred from the color of the filters. This is because these diacids and AS can complex Fe(III) and hence compete with catechol.[169] The formation of the iron

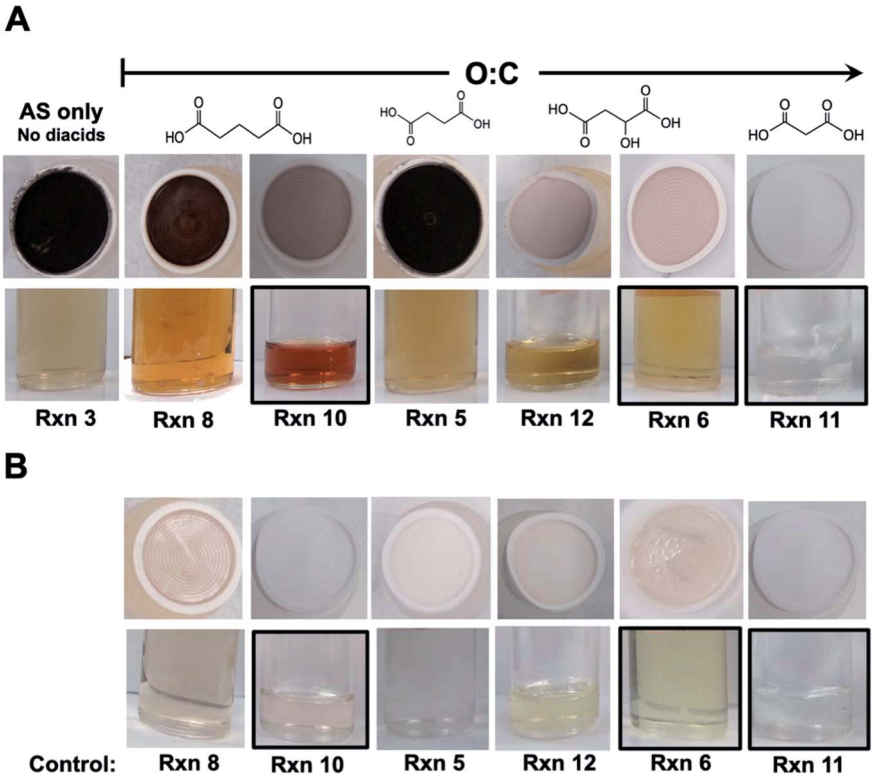

Fig. 15 (A) Digital photographs of filters and filtrate solutions after 24 h of selected reactions listed in Table 6 between catechol (1×10^{-3} M) and $FeCl_3$ (2×10^{-3} M) in AS solutions. The photographs are arranged in the order of increasing O : C molar ratio of the most dominant diacids based on the structures shown. (B) The corresponding photographs for the control reactions in the absence of catechol. The black border marks the filtrate samples analyzed using UHPLC-UV-MS and ion chromatography-MS. Reproduced from ref. 148 with permission from the American Chemical Society, © 2021.

catecholate complex, $Fe(C_6O_2H_4)^+$ (Fe–CA), is the first step in the oxidative polymerization mechanism. As the kinetics of the iron catecholate complex, $Fe(C_6O_2H_4)^+$ (Fe–CA), formation is 3× that of forming iron sulfate, $Fe(SO_4)_2^-$, and iron malate, $Fe(C_4O_5H_4)^+$ (Fe–MA) (Table 3), and because similar kinetic data were not available for other diacids, the last column in Table 3 shows the percentage of Fe–CA complexes relative to other complexes in solution from thermodynamic modeling. These values were the basis for explaining the trend in particle density observed in Fig. 15.[148] Despite the very low values of %Fe–CA in Rxn no. 2–12 (Table 6), polycatechol particles still formed (as judged by the color of the filters for reaction and control

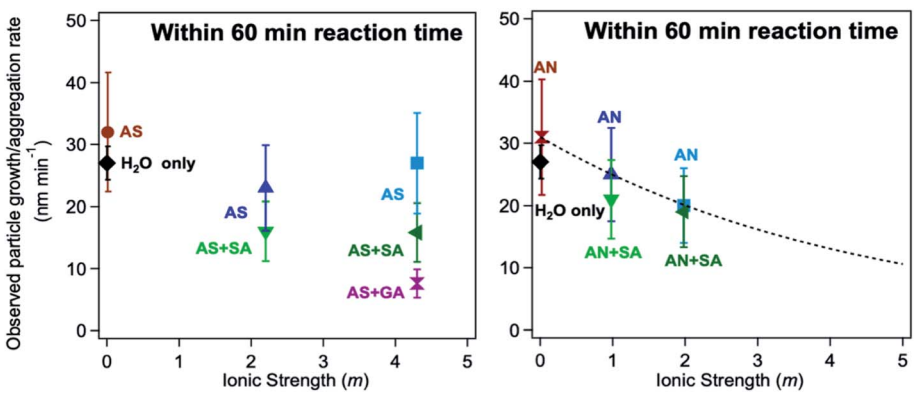

Fig. 16 Observed rate of particle growth/aggregation as a function of ionic strength (I) from the time-dependent DLS data in the first 60 min reaction between catechol (1×10^{-3} M) and $FeCl_3$ (2×10^{-3} M) in (left) AS solutions used in different background solutions listed in Table 6, and (right) AN solution of varying compositions as per Table S2 in ref. 148. The line through the data is an exponential decay fit, $y = a + be^{-cx}$, with $a =$ 0.5 nm min^{-1}, $b = 31$ nm min^{-1}, and $c = 0.2$ m^{-1}. DLS data with error bars represent $\pm 1\sigma$. Reproduced from ref. 148 with permission from the American Chemical Society, © 2021.

experiments) with apparent reduction in particle density with increasing concentrations of the diacids that strongly complex with iron (Mal > MA > GA). This trend correlated with the O : C molar ratio of these diacids (Table 2: 1.33 > 1.25 > 0.8, respectively). SA was removed from this list because it had lower solubility than other diacids, which prevented our ability to conduct experiments using concentrations 1 and 2 M. The case of Rxn no. 11 where Mal is the dominant diacid was the only one where no evidence of particle formation was observed. For Rxn no. 6, 7, and 12, the Visual MINTEQ thermodynamic model calculated a %Fe–CA to be zero, yet discoloration of filters was apparent after 24 h of reaction (Fig. 15). This discoloration is due to traces of polycatechol particles suggesting a significant reduction in the rate of particle growth under these reaction conditions.

On the other hand, nitrate is a much weaker ligand than sulfate, hydroxide, and chloride,[245] hence the calculated fraction of iron species in solution did not contain iron nitrate.[148] The addition of the diacids to the AN solutions had a larger impact on the %Fe–CA than the increasing AN concentration. For example, increasing the concentration of AN from 0.01 to 12.3 M reduced the %Fe–CA from 9.5 to 2.4, and adding diacids further reduced %Fe–CA to be in the range 0–0.8 depending on the diacid (see Table S2 in ref. 148). The %Fe–CA in AN solutions were considerably higher than that employed for Rxn no. 1–3 using AS (Table 6), which ranged from 1.2–0.12. This difference had an impact on the rate of particle growth/agglomeration, as determined by DLS experiments. Fig. 16 shows the observed rate of polycatechol growth/aggregation as a function of I in different solutions using AS and AN with and without diacids. Using either AS or AN, and within the uncertainty of the measurement, these data showed that increasing I and addition of diacids reduced the initial rate of polycatechol growth/agglomeration. The addition of SA at 0.2 M concentration (200× higher than catechol) did not result in a statistically significant reduction in the rate at $I = 1$ and 2 m compared to the observed with no SA (using AN, right). These results suggest that under these conditions, the presence of iron succinate with AN did not interfere with the kinetics of the oxidative polymerization of catechol, which was not observed in the case of AS (Fig. 16 left). This result signifies the role that the type of the inorganic anion plays in the mechanism of polycatechol formation, which warrants further investigation.

The reduction in the polycatechol growth/aggregation rate in solutions with high I and levels of diacids allowed for the detection of oligomers that were not observed earlier. Rxn no. 6, 10, and 11 in Table 6 were selected for mass spectrometric analysis because their filtrate solutions shown in Fig. 15 highlight the effect of dicarboxylic acids on the optical properties of the products. The retention times, m/z values, and general elemental formula of labeled chromatographic peaks in Fig. 17 are provided in Table 7. The suggested structures of the molecules with the elemental formula in Table 7 are shown in Scheme 2. The formation of the organonitrogen compound, $C_{12}H_7O_3N$, assigned to peak 4 was confirmed using $(^{15}NH_4)_2SO_4$ and HR-MS(+) detected at m/z^+ 214.0501, which is only 1.1015 ppm apart from that at m/z^+ 214.0499 for $C_{12}H_8O_3N^+$.

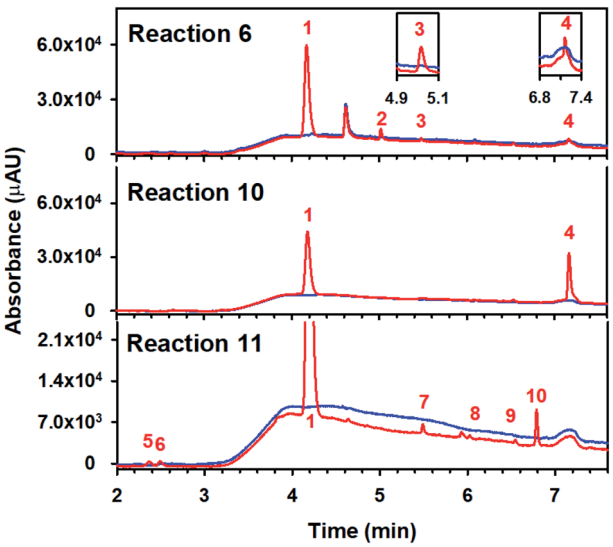

Fig. 17 UHPLC-UV chromatogram ($\lambda = 210$ nm) for (red lines) Rxn no. 6 (top), 10 (center), and 11 (bottom) after 24 h of reaction between catechol (1×10^{-3} M) and $FeCl_3$ (2×10^{-3} M) in AS solutions, as listed in Table 6. The blue lines correspond to the respective control solutions without catechol. Except catechol (peak 1), all other labeled peaks correspond to products described in the text. Reproduced from ref. 148 with permission from the American Chemical Society, © 2021.

Such organonitrogen molecule was not recognized in earlier studies but is now available for further evaluation in new laboratory studies and field sampling, where it can play a role as a reactive intermediate. Hence, metal-catalyzed reactions driven by dissolved oxygen that lead to the formation of NOC in particles are potentially important pathways in systems containing ammonium and transition metals, which warrant further investigation.

5.2 Dicarboxylic acid precursors

Unlike most dicarboxylic acids that form strong soluble complexes with iron such as oxalic and succinic acids, the reaction of unsaturated C4–C6 dicarboxylic acids detected in aged secondary organic aerosols[3,164] – with Fe(III) under acidic conditions led to the efficient formation of insoluble and colored polymeric compounds, even in the presence of competing ligands such as sulfate and oxalate. Tran *et al.*[69] showed that fumaric and muconic acids react with $FeCl_3$ at pH 3 forming orange colored organometallic polymers, Fe-polyfumarate and Fe-polymuconate. Fig. 18 shows the photographs of reaction solutions and filters. The mass yields were found to be ~84 ± 6% using fumarate and 52 ± 6% using muconate at pH 5 after overnight reaction. These yield values are relative to the initial concentration of the organics (2.1 mM) in control experiments at pH 5. Scheme 4 shows the proposed structures of these organometallic polymers based on the dry particle characterization using ATR-FTIR spectroscopy, TGA, transmission electron microscopy (TEM) with diffraction, scanning transmission electron microscopy-energy dispersive X-ray spectroscopy (STEM-EDS) for elemental mapping, electron

Table 7 Retention time (r.t.) for chromatographic peaks in Fig. 17 with m/z values and molecular formula in the negative and positive ion modes. See Scheme 2 for suggested structural formulae. ND = not detected. Reproduced from ref. 148 with permission from the American Chemical Society, © 2021

		m/z^-		m/z^+		
Peak#	r.t. (min)	Parent	Fragment	Parent	Adduct	Molecular formula
1	4.17	109.10			128.15 ($M + NH_4^+$)	$C_6H_6O_2$
2	5.02	207.20				$C_{11}H_{12}O_4$
3	5.48	ND		453.29	470.32 ($M + NH_4^+$)	$C_{18}H_{12}O_{14}$
4	7.16	212.18	173.19	214.20		$C_{12}H_7O_3N$
5	2.37	167.14	149.12			$C_8H_8O_4$
6	2.49	167.10	123.09			$C_7H_4O_5$
7	5.49	217.20			471.48 ($2M + 2NH_4^+ - H^+$)	$C_{12}H_{10}O_4$
8	6.03	315.25			334.30 ($M + NH_4^+$)	$C_{16}H_{12}O_7$
9	6.54	249.20		251.21		$C_{12}H_{10}O_6$
10	6.79	365.27			384.31 ($M + NH_4^+$)	$C_{16}H_{14}O_{10}$

energy loss spectroscopy (EELS) for oxygen K-edge, and XPS for iron oxidation state. The presence of excess oxalate in solution was found to suppress the formation of Fe-polyfumarate and Fe-polymuconate particle formation, whereas excess sulfate had no effect.[68] Polymerization reactions efficiently take place in the presence of sulfate in solution producing particles with iron-coordinated and/or pore-trapped sulfate groups. When soluble iron was the limiting reagent, the insoluble product mass was reduced, highlighting the central role of excess iron in catalyzing particle formation in solution.

The insoluble particles were found to be amorphous, contain iron in the oxidation state between 2+ and 3+, and can form using reaction solutions at 21-fold lower organic reactant concentrations than those used in Fig. 18. These particles are responsible for the UV absorbance of unfiltered reaction solutions at 370 nm, which was assigned to the π–π* transitions in C=C groups of Fe-polyfumarate and Fe-polymuconate backbone structures. The UV absorbance spectra were converted to the mass-normalized absorption coefficient (MCA) for comparison with those recorded for other BrC materials, as discussed in the following sections. For comparison, OH or ozone oxidation of FA and MA would instead produce water-soluble products that do not absorb visible light.[246] Hence, the iron-catalyzed polymerization described here opens up unique pathways for processing these diacids.

Using 25–50 μM concentrations of organic diacids, the DLS experiments aimed at monitoring the particle growth in real time showed that polydispersed particles formed quickly and

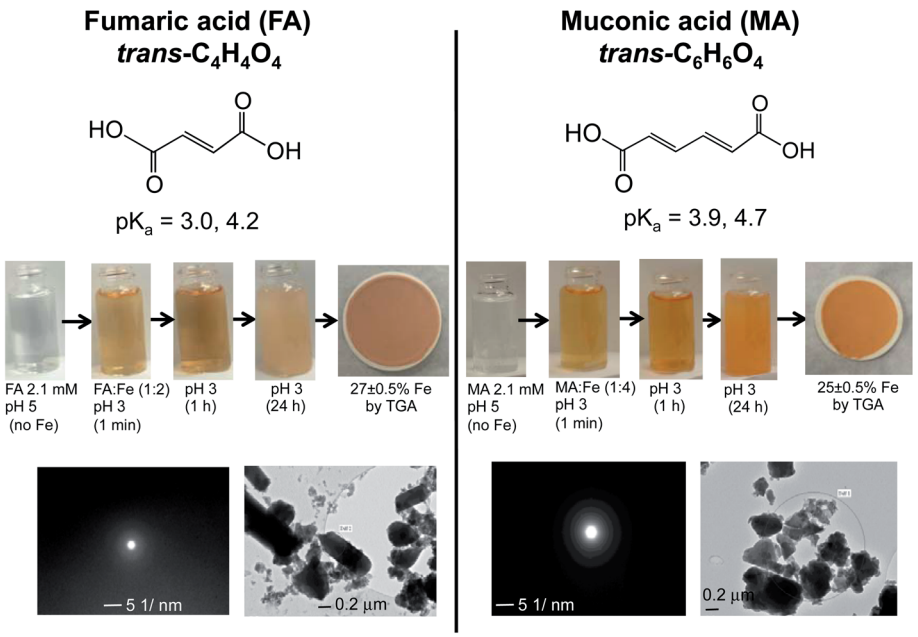

Fig. 18 Dark reaction of fumaric acid (FA, panels on the left) and muconic acid (MA, panels on the right) with $FeCl_3$ at pH 3: (top) chemical structure and pK_a values of FA and MA; (middle) digital images of the 1 : 2 organic reactant/Fe molar ratio of unfiltered solutions as a function of time and particles on filters after 24 h of reaction time; and (bottom) TEM images with diffraction of dry Fe-polyfumarate and Fe-polymuconate particles. Reproduced from ref. 69 with permission from the American Chemical Society, © 2021.

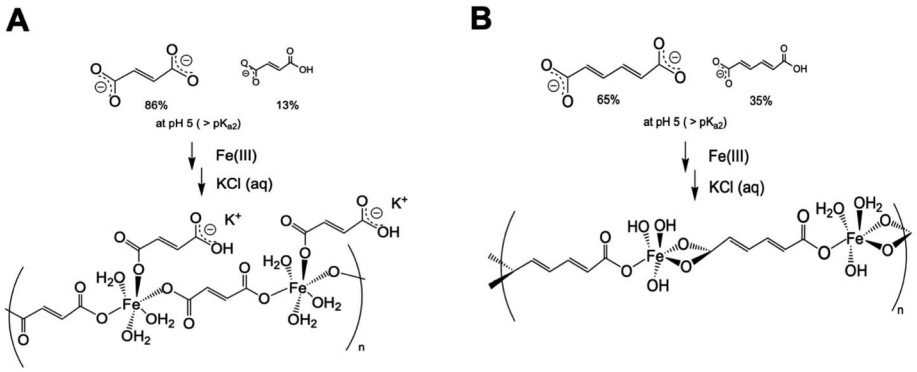

Scheme 4 Diagrams for the formation of (a) Fe-polyfumarate, and (b) Fe-polymuconate based on structural elucidation of the organometallic polymers in ref. 69. The percentages show the fraction of species in solution based on the pK_a values of fumaric and muconic acids, respectively.

grew to >100 nm in hydrodynamic size after half an hour of reaction.[68] The growth rate of these particles appears to depend on the final organic reactant : Fe molar ratio and pH. Within the variability of the DLS results in Fig. 19a and b, it is clear that sulfate has no significant effect on the kinetics of particle growth/agglomeration relative to the control. The addition of oxalate, on the other hand, appeared to initially produce relatively larger particles that grow to micron-size particles at a faster rate than when sulfate is added or in the control case. The product masses under these reaction conditions with oxalate and sulfate in solution resulted in values close to the control value (see Fig. 2 in ref. 68). Hence, it was concluded that the initial solution nucleation is retarded by oxalate, which produces fewer particles. In conclusion, Fe-polyfumarate and Fe-polymuconate efficiently form over a wide range of atmospherically relevant conditions. The iron centers in the amorphous structures of Fe-polyfumarate and Fe-polymuconate could act as catalysts for the dark and photochemical production of reactive oxygen species (ROS)[77] such as OH and H_2O_2, adsorption of oxyanions such as sulfate, and reduction of NO_x in the presence of ammonia. The low solubility of these particles makes them uniquely different from the much better known oligomeric compounds formed during VOC oxidation, which are commonly water soluble.[247] These chemical processes will depend on the amount of 'adsorbed water' and aerosol liquid water. Similar to polycatechol and polyguiacol,[70] and as presented in the following section on the optical properties and morphology, the presence of polymeric products in atmospheric aerosol particles would affect their absorption and scattering properties, and the high hydrophobicity of Fe-polyfumarate and Fe-polymuconate would drive their enrichment at surfaces of aerosol particles with direct consequences on their (likely poor) ability to act as clouds and ice condensation nuclei.[248,249]

5.3. Reactivity of BBOA aqueous extracts with iron

Reactions of BBOA aqueous extracts with Fe(III) were examined to check whether this chemistry can occur in realistic atmospheric samples.[190] In these experiments, dried pine needles were burned and the resulting BBOA particles were sampled during different burning stages on Fluoropore PTFE membrane filters. Each filter was then extracted using 10 mM KCl solution at pH 3 by shaking the solution for 1 h. As not all BBOA material could be extracted using this method, the mass concentration of BBOA compounds (C_{mass}) in the extract was estimated using UV-vis spectroscopy where the base 10 absorbance (A) is measured in

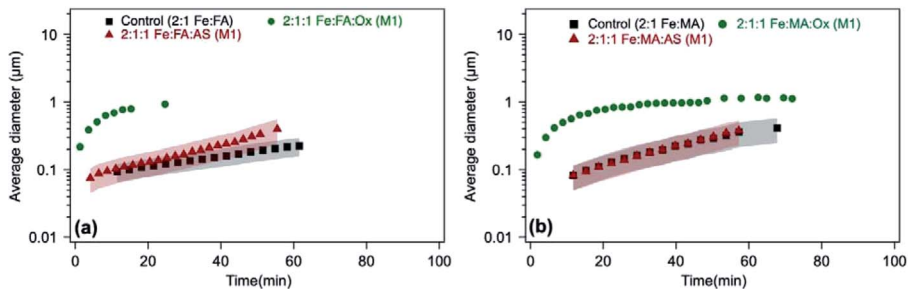

Fig. 19 Effect of adding oxalate (Ox) and ammonium sulfate (AS) on particle size from time-dependent DLS measurements during the dark aqueous phase reaction of (a) fumarate (50 μM, FA) and (b) muconate (25 μM, MA). This molar ratio results in the maximum product mass per data shown in Fig. 1. 'M1' stands for method 1, where organic reagents were mixed first with AS or Ox, then the reaction time started when Fe was added. 'M2' stands for method 2, where AS or Ox were reacted first with Fe for 2 h, then the reaction time started when the organic reagent was added. The shaded areas represent the standard deviation of three trials. Unshaded data represent the average of two trials, with a standard deviation the size of the marker width (15%). Reproduced from ref. 68 with permission from the American Chemical Society, © 2021.

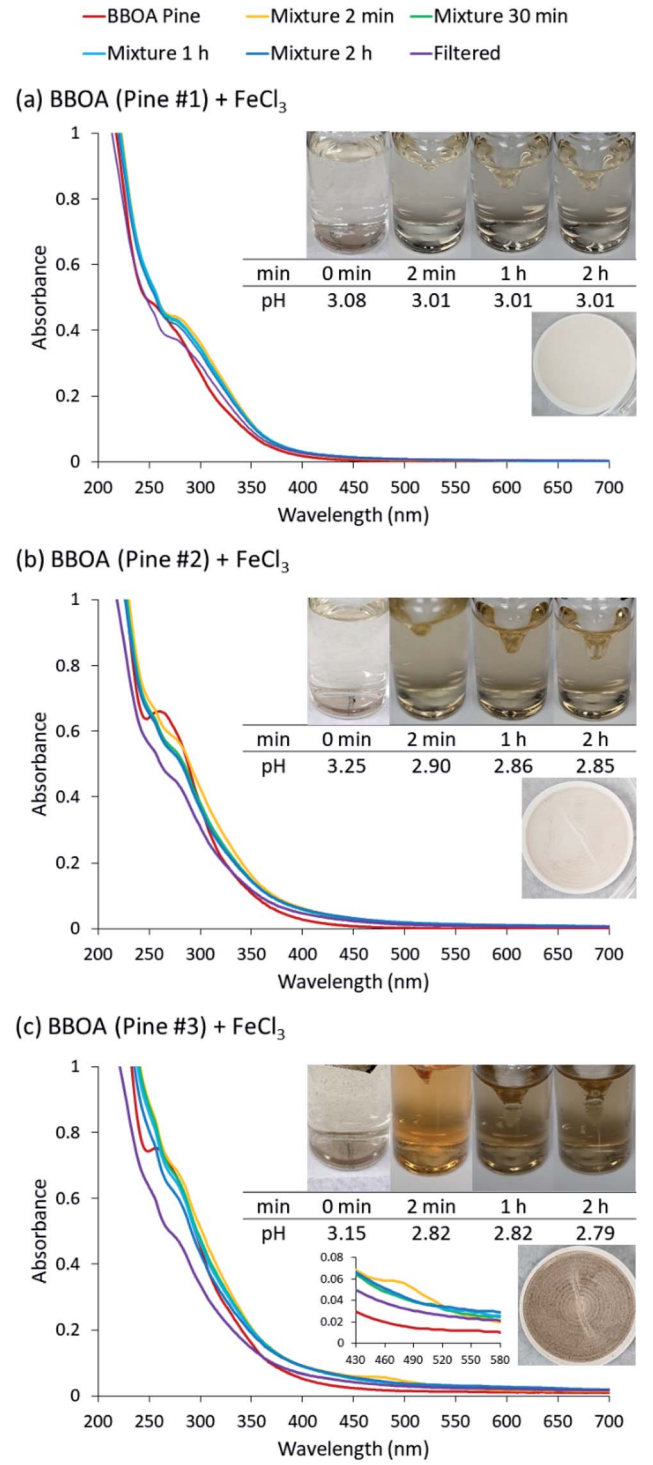

Fig. 20 UV-Vis absorption spectra of mixture of excess Fe(III) and BBOA extracts. Different colors of traces correspond to the spectra of BBOA before mixing (red), 2 min after mixing (orange), 30 min after mixing (green), 1 h after mixing (light blue), 2 h after mixing (dark blue), and filtered solution (purple). Reproduced from ref. 190 under Create Commons License (CC BY-NC) from the Royal Society of Chemistry, © The Author(s), 2021.

a cuvette path length (l) with a typical value of mass absorption coefficient (MAC)[250] at 365 nm equal to ~1 $m^2\ g^{-1}$ according to eqn (25):

$$\mathrm{MAC}\ (\lambda) = \frac{A(\lambda) \times \ln(10)}{l \times C_{\mathrm{mass}}} \quad (25)$$

The molar concentration of BBOA compounds in the extract was estimated assuming an average molecular weight of 200 g mol^{-1}. Fig. 20 shows the UV-Vis spectra of the reaction solutions of BBOA and $FeCl_3$ at pH 3 under dark conditions and the filter after 2 h of reaction. These data show that the particle density from iron chemistry varied depending on the amount of smoldering combustion that occurred while BBOA samples were collected. Pine #1 was taken at the start of the burning when conditions could be characterized as flaming. In this case, it is very likely that the BBOA did not contain sufficient quantities of reactive catechol or guaiacol derivatives, or it contained compounds with stronger affinity to Fe(III) preventing it from particle-forming reactions such as nitrated aromatics,[251,252] Pine #2 was collected later in the burning process, when at least half of the fuel burned. Upon mixing with Fe(III), the changes in the UV vis spectra and the pattern of color change of the reaction with $FeCl_3$ were similar to those of the reaction of 4-MC and $FeCl_3$. Given these observations and the lack of particles on the filter after 2 h of reaction, it was inferred that BBOA compounds produced during this burning stage may form complexes, but they do not partake in the subsequent polymerization over relatively short reaction times, *i.e.*, 2 h. In the case of Pine #3, BBOA was collected after the fire was extinguished by placing a lid on the container where burning took place. This resulted in purely smoldering conditions, expected to emit lignin pyrolysis and distillation products.[253] The UV-Vis spectrum for reaction solutions of Pine #3 with Fe(III) had a notable decrease over time at 480 nm that matched that of the reaction of 4-HC and $FeCl_3$. Also, the particle mass yield was found to be 53% after 2 h of reaction with Fe(III). Therefore, it appears that BBOA produced during smoldering conditions contain hydroxylated aromatics such as 4-HC. In conclusion, the behavior of three different samples of BBOA contrasts with the highly reproducible results of experiments in which individual catechol derivatives were mixed with Fe(III), suggesting the need for further investigation of how burning conditions and fuel types affect the BBOA chemical composition and the composition of its aqueous phase extracts.

6. Atmospheric impact of particles from iron chemistry

6.1. Dust dissolution and reactivity

The length of time mineral dust particles spend either as a wet aerosol or in cloud droplets will affect the amount of soluble iron due to aging during long range transport. The uptake of acids within clouds can also enhance iron dissolution in the droplets or in the residual aerosol formed after droplet evaporation. The chemistry described above used $FeCl_3$ as a source of dissolved iron in aqueous phase reactions to simulate the reactivity in aged iron-containing mineral dust particles. To simulate acid-driven dissolution of freshly emitted dust and its reactivity with catechol, two types of experiments were

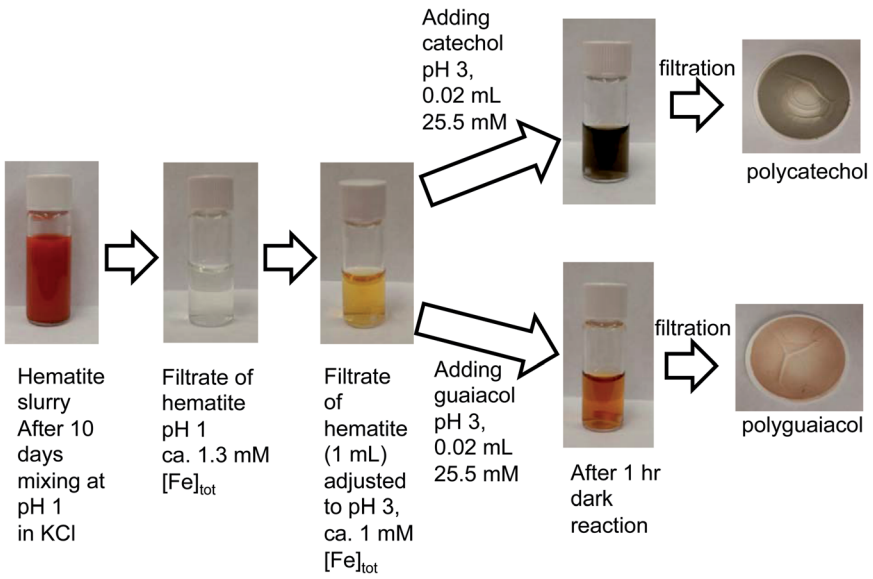

Fig. 21 Formation of polycatechol and polyguaiacol from reaction with dissolved iron from acid-promoted hematite dissolution. Reproduced from ref. 70 with permission from the American Chemical Society, © 2015.

conducted, one with hematite[70] and one with Arizona Test Dust (AZTD).[206] Fig. 21 shows the digital images of hematite slurry following 10 days of mixing at pH 1. Also shown are images of the filtrates before and after the addition of catechol and guaiacol, in addition to the filters after 1 h of reaction. The changes observed in the color of the solutions before filtration and the presence of the polycatechol and polyguaiacol particles on the filters clearly highlight that the same chemistry takes place as that observed using $FeCl_3$.

Using AZTD, Link *et al.*[206] studied its reaction with dissolved catechol as functions of time and pH in the dark. The left and right panels of Fig. 22 show photographs of AZTD control (C, no catechol added) and reaction (R, with catechol) slurries over a 14 day period and that of the dry particles after filtration. Photographs of the AZTD slurries in Fig. 21 showed little change in color over the 14 d reaction time. However, the color of the particles on the filters from the reaction vials appeared darker compared to that from the control vials with no catechol. Similar studies were conducted using hematite nanoparticles under acidic pH where progressive darkening in the color of the slurry containing catechol with time was observed (see ESI in ref. 206). The darker color of the dried filters obtained after 14 d of simulated acid processing suggests that the adsorption of catechol to iron-containing materials slowly changes the surface chemical composition of the particles. Fig. 23 shows the scanning transmission electron microscopy (STEM) images of AZTD particles with catechol (top) and unreacted (bottom) following nearly two weeks of reaction at pH 1. The STEM images were coupled with energy dispersive X-ray spectroscopy (EDS) elemental mapping to show the distribution of carbon, oxygen and iron in the samples. The iron signals are concentrated in some areas where brighter areas correspond to higher relative amounts than dimmer areas. The carbon signals in Fig. 23a for particles reacted with catechol are not uniformly distributed across the image with some areas having larger amounts of detected carbon than the others. The C atomic% is higher for AZTD-Cat at 4.5% compared to undetectable for the control AZTD (no catechol in Fig. 23b). Other STEM images in ref. 206 showed that there is some co-localization of the iron and carbon signals, suggesting that the iron content in the dust particles might be anchoring the polymeric network of polycatechol, which upon formation, might encapsulate the dust particle.

In the soil chemistry literature, catechol was found to undergo catalytic abiotic oxidation on the surfaces of iron and manganese oxides at basic pH (pH > 8). Scheme 5 shows a three-step mechanism for the formation of polycatechol proposed by Colarieti *et al.*[254] Steps 1 and 2 are heterogeneous reactions, which involve the partial oxidation of catechol due to an electron transfer to surface iron and the release of Fe(II) to solution. The reduced Fe(II) species in solution further complex with catechol, which then undergoes homogeneous oxidation, step 3, in the presence of dissolved oxygen. This reaction step involves cycling between Fe(II) and Fe(III) species and the production of reactive oxygen species, H_2O_2 and OH radicals, as intermediates.[217] Under acidic conditions relevant to atmospheric aerosol pH, the same chemistry takes place albeit over days of reaction time. Although the reaction kinetics with AZTD and HEM particles are slower under acidic relative to basic pH according to the qualitative assessment of the filter images in Fig. 22, polycatechol formation changes the optical properties of the dust and hematite particles (discussed in detail below). In summary, the change in the chemical composition of iron-containing particles driven by oxidative polymerization of catechol changes the optical properties, mixing state and morphology of the particles. The next few sections elaborate on the latter topics and their impact on the hygroscopic properties of atmospheric particles.

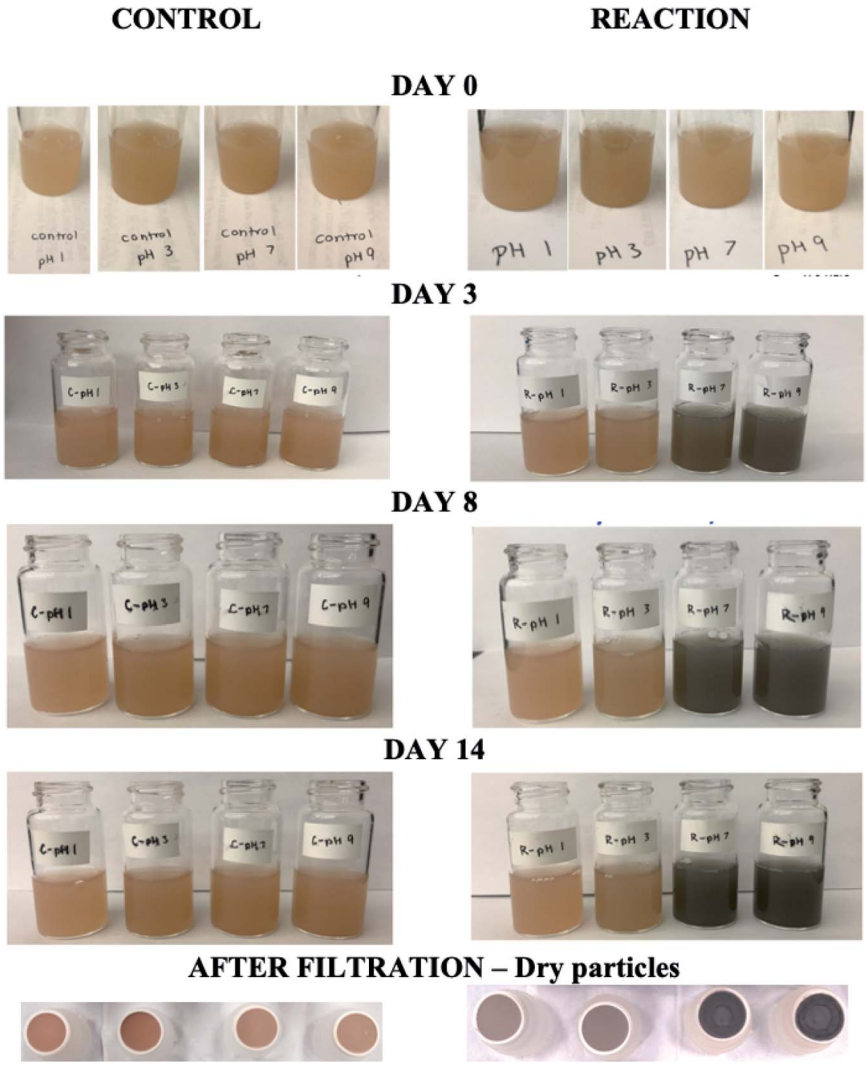

Fig. 22 Digital photographs of control (C, left) and reaction (R, right) vials containing AZTD as a function of pH and simulated atmospheric aging time. The pH values shown in the label of each vial refers to the starting pH of the slurry. At the end of day 14, the slurries were filtered and the corresponding filters are shown below each vial. The concentration of DFe in the filtrates of C-pH 1, R-pH 1, and R-pH 3 were 9.5, 12.2, and 2.3 mg L^{-1}, respectively. Values of DFe for the other filtrate solutions were below the detection limit of the instrument (0.25 mg L^{-1}). Reproduced from ref. 206 with permission from the American Chemical Society, © 2020.

6.2. Mixing states and morphology

The complex chemical composition of atmospheric aerosols influences their physical properties such as the morphology and the mixing state. Aerosol morphology is a general term that reflects the apparent shape, size, and topology of particles from optical and electron microscopy images. Examples of morphology include homogeneous, phase-separated core–shell and partially engulfed.[255–257] The mixing state refers to the chemical speciation and physical properties of each particle.[27,31,258,259] Often the mixing state is described in terms of external and internal mixtures to refer to the number of chemical species per particle in an aerosol population. Freshly emitted particles are more externally mixed, whose atmospheric aging leads to internal mixing. Experimental measurements of the physical and chemical properties provide information on their distribution within the particle population of an aerosol. Riemer *et al.*[31] and Laskin *et al.*[32] reviewed the literature on the techniques used to obtain information on aerosols' mixing state, their advantages and limitations. Using some of these techniques, You *et al.*,[35] Li *et al.*,[260] and Song *et al.*[257] identified mixing states beyond homogeneous-like particles that include dumb-bell, core shell and organic matter-coating, as shown in Fig. 24. These morphologies and mixing states depend on the particle size, are not static and tend to evolve over time due to multiphase aging processes in the atmosphere including the variation in the relative humidity that can lead to liquid–liquid phase separation and other phase transitions.[35,257]

In order to explore the mixing state and morphological changes to aqueous droplets containing organics and iron, the reaction between catechol, guaiacol, fumaric acid and Fe(III) in a micrometre-sized aqueous droplets was monitored *in situ* and in real time under a constant flow of humid air (~96–100% RH)

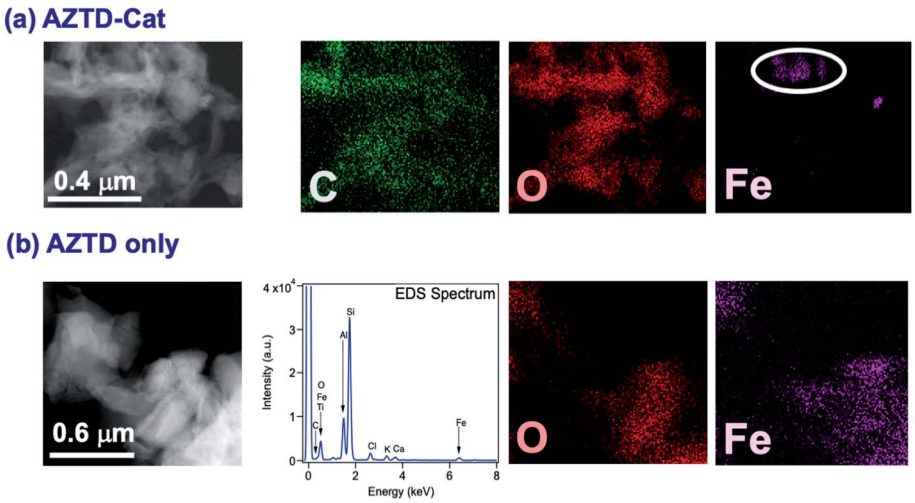

Fig. 23 Representative STEM images and EDS elemental mapping of AZTD particles with (a) polycatechol (AZTD-Cat) and (b) control (AZTD only, no catechol in solution). Slurries used for the images are shown in Fig. S3 in the ESI.† The images labeled C, O, and Fe represent the elemental maps for the corresponding atoms. In (b), no carbon signal was detected in the EDS spectrum, hence no carbon map was generated. Reproduced from ref. 206 with permission from the American Chemical Society, © 2020.

using an optical spectroscopy setup used for monitoring liquid–liquid phase separation in aqueous phase droplets at the University of British Columbia.[35] Fig. 25 shows images of these droplets at the beginning of the reaction for comparison with those collected after the reaction proceeded for the times specified. These images indicate that polycatechol and polyguaiacol form as 'inclusions' in the aqueous droplets, whereas Fe-polyfumarate forms a polymeric network at the air/aqueous interface. An animation movie in the ESI† shows the movement of this polymer at the surface of the droplet, while flowing humid air suggests a preference for the core–shell morphology. These results highlight changes to the droplet morphology, mixing state, and chemical composition due to the formation of the insoluble products from iron chemistry. These changes would have consequences on the bulk and surface chemistry of the droplets.

6.3. Optical properties

The term aerosol optical properties refer to optical parameters that quantify aerosols' ability to scatter and absorb shortwave and longwave radiation through the imaginary (k) and real (n) parts of the particle refractive index, $m = n - ik$. Both components contribute to the extinction coefficient of the material of interest and vary with the wavelength, which for atmospheric aerosol particles, ranges from the near-UV to the IR part of the

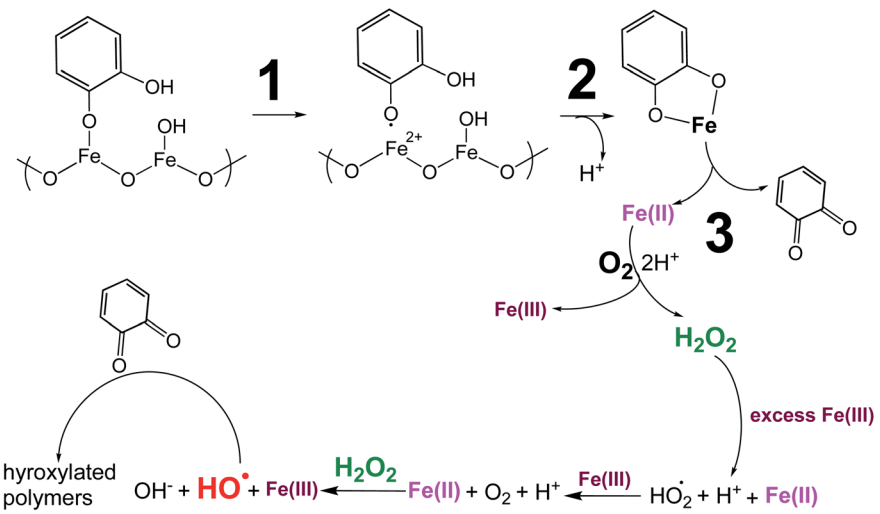

Scheme 5 A three-step mechanism for abiotic oxidative polymerization of catechol on the surface of iron oxide proposed by Colarieti *et al.*[254] and Larson and Hufnal Jr[217] The different colors are used to highlight the oxidation state of the iron in the respective step. The larger size of OH and H_2O_2 is used to highlight the reactive oxygen species generated in the reaction. Reproduced from ref. 206 with permission from the American Chemical Society, © 2020.

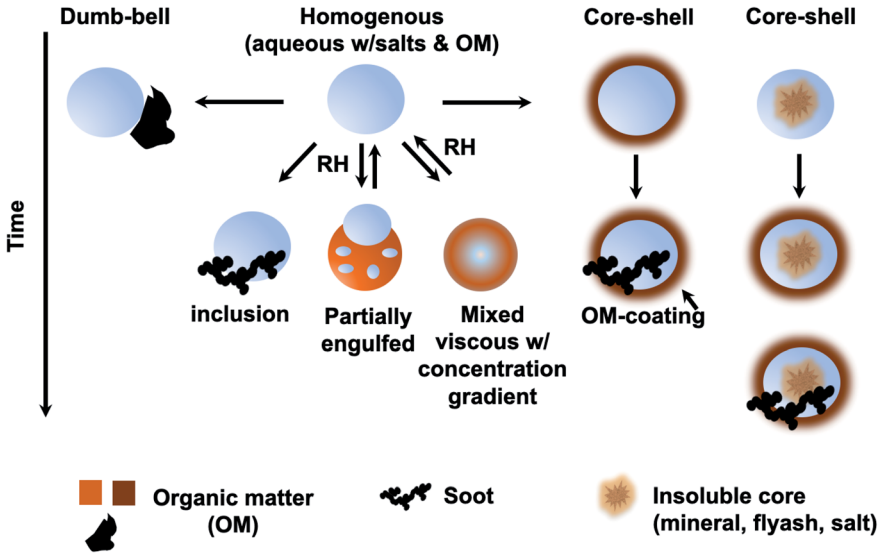

Fig. 24 Schematic of major atmospheric aerosol morphology and mixing states proposed by You *et al.*,[35] Li *et al.*[260] and Song *et al.*[257]

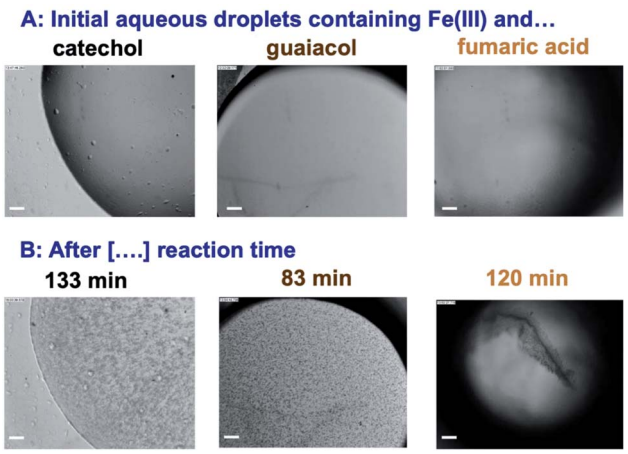

Fig. 25 Optical images of aqueous droplets showing the formation of polycatechol (left), polyguaiacol (middle) and Fe-polyfumarate (right). Left and middle images were taken from the bottom of the droplet, and the right image was taken from the top of the droplet. Reaction final concentrations were 5 mM organic precursor and 10 mM $FeCl_3$(aq). Each droplet, of 2 μL, was 'sandwiched' between two slides with no flow of humid air over the droplet. After acquiring the initial images shown in the top panel, the reaction took place in the dark, with slides placed in the condition flow cell on the bench. Then, the flow cell was transferred to the microscope to collect the images during the flow of humid air at ~ 100% RH at the specified reaction time in the lower panel. The scale bar = 0.1 mm. Unpublished results in collaboration with Professor Allan Bertram and graduate student Yuanzhou Huang at the University of British Columbia (2019).

electromagnetic spectrum.[261] As outlined in the review article by Laskin *et al.*,[33] the measurements of optical properties will vary depending on the sample being analyzed: bulk solid aerosol materials as thin films, bulk liquid aerosol extracts, air containing aerosol particles, and aerosol-loaded filters. The refractive index of scattering particles is used in Mie theory calculations along with the size distribution to compare the calculated phase function and linear polarization for light scattering with experimental ones.[262] Mie theory was derived for spherical particles and hence is limited in predicting particle scattering from non-spherical and irregularly shaped particles, as illustrated in the case of mineral dust and its components.[263] These parameters are used in climate models for the calculation of the radiative forcing due to aerosol–radiation interactions (RFari).[1] The values of RFari clearly show a variation depending on the chemical properties. These properties are not static and change during the lifetime of the aerosol particles.

Fig. 26 shows a graphical representation of the absorption and scattering optical parameters, namely *k*, mass absorption coefficient (MAC), and single scattering albedo (SSA) for three aerosol types with dominant light absorption properties as it results in positive RFari and hence have direct climate relevance,[264] namely mineral dust, black carbon (BC) and brown carbon (BrC). Conceptually, the net shortwave aerosol absorption, usually quantified through the absorbing aerosol optical depth (AAOD), can therefore be thought of as the sum of the contributions of the above three separate species, integrated over the atmospheric column.[264] Modeling AAOD is challenging and hence model validation, because the observed aerosol mixing state makes clear distinctions between separate aerosol types hard.[258,264] The SSA values range from 0 to 1 (purely scattering). Aerosols that have SSA values below ~0.85–0.9 indicate the absorption of solar radiation, hence they have a net positive RF.[265]

6.3.1 Mineral dust. Mineral dust in the atmosphere is the most abundant atmospheric aerosol by mass in most global aerosol models;[266,267] as a result, its absorption of solar radiation can dominate that of BC and BrC in some regions and seasons.[268,269] Because climate forcing is highly sensitive to the optical properties of dust particles,[270] dust radiative forcing can be positive (heating) or negative (cooling) depending on the values of key variables that include the height of the dust layer, particle size and aerosol optical depth (AOD).[103] Although dust

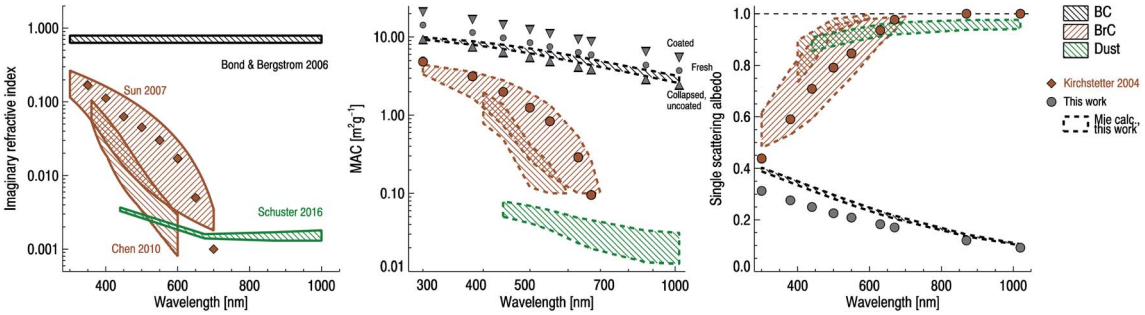

Fig. 26 Physical parameters used in modeling aerosol absorption: wavelength dependence of the imaginary refractive index (left), MAC (middle), and SSA (right). The term 'this work' refers to ref. 264. Reproduced from ref. 264 under Create Commons License (CC BY-NC-ND 4.0) from Springer, © The Author(s), 2018.

particles weakly absorb visible radiation (single scattering albedo (SSA) of dust particles is typically in excess of 0.95 at the peak of the solar spectrum[271,272]), the SSA value depends on the particle size and mineralogy (particularly, the hematite and goethite contents). Scanza *et al.*[273] reported the simulation of dust radiative forcing as a function of both the mineral composition and size on the global scale, using mineral soil maps for estimating emissions. Previous field measurements showed that volatiles efficiently transfer from accumulation mode particles onto dust particles in Asian outflows,[274] thus creating an environment for the possible reactions between volatiles and dust surfaces. Light-absorbing inclusions on dust have a strong effect on its optical properties, for example, internal mixing of dust particles with strongly light-absorbing black carbon has been shown to decrease the SSA for a smaller particle size.[275]

Al-Abadleh and co-workers reported on a chemical process that made dust more light absorbing.[206] Using AZTD and hematite nanoparticles as laboratory standards and proxies for hematite-rich natural dust, respectively, they showed that reactions with catechol over 14 days of simulated acidic atmospheric aging (pH 1 and 3) lead to the formation of black polycatechol, increasing the ability of dust and hematite to absorb light over a wide range of wavelengths given its dark color. This simulated aging process was in contrast with the behavior of oxalate and sulfate that form complexes with iron sites, promoting the dissolution of iron minerals in dust. Hence, this aging chemistry may change the radiative forcing of dust aerosol from negative to positive, similar to that of black carbon. Mixing with pollution emissions during mineral dust transport is also recognized to alter the optical properties of dust.[276–278] Bi *et al.*[277] quantified the optical parameters of pure and transported anthropogenic dust over East and Central Asia for improving the accuracy of remote sensing applications and global climate models.

6.3.2 Black carbon (BC or soot). Black carbon (BC) or soot is the most abundant light absorbing carbonaceous aerosol type, which results from the combustion of fossil fuels and biofuels.

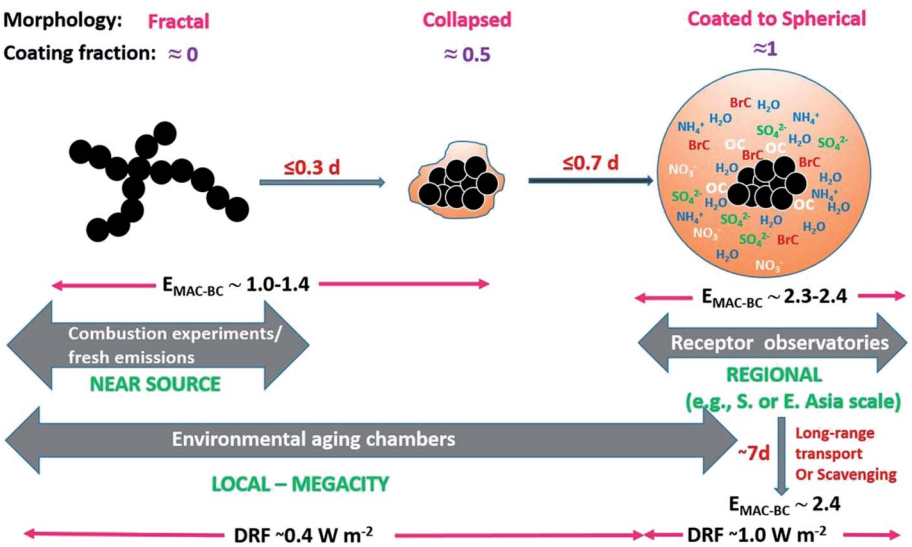

Fig. 27 Time-course evolution of BC aerosol composition, light absorption (where E_{MAC-BC} is the enhancement because of coatings relative to fresh/uncoated particles), and associated climate effects (as DRF). Reproduced from ref. 281 under the Create Commons License (CC BY-NC-ND 4.0) from the National Academies of Sciences USA, © The Authors, 2016.

Table 8 Overview of enhancement factors from a number of studies. Reproduced from ref. 264 under Create Commons License (CC BY-NC-ND 4.0) from Springer, © The Author(s), 2018

	$E_{abs,fresh}$	$E_{abs,aged}$	$E_{abs,total}$	
Reference	Pure → fresh	Fresh → aged	Pure → aged	λ (nm)
Bond and Bergstrøm (2006)[285]	1.5	1.5	(2.3)	
Cappa *et al.* (2012)[286]	1.06	1.2		532
Cui *et al.* (2016)[287]	1.4	1.7	3	678
Peng *et al.* (2016)[288]			2.4	532
Liu *et al.* (2015)[289]	1.1	1.4		781
Healy *et al.* (2015)[290]	1.0			781
Nakayama *et al.* (2014)[291]	1.1			781
Sinha *et al.* (2017)[292]			1.44	565
Lan *et al.* (2013)[293]	1.07			532
Liu *et al.* (2017)[294]		1.1–1.6		405, 532, 781

Within the current uncertainty, BC has a net positive radiative force second only to CO_2.[279,280] Bond and Bergstrom[261] reviewed the literature on the relationship between the structure of BC and its optical parameters to be used in models. Flame-generated BC contains sp^3 bonds (as in diamond) and sp^2 bonds with loosely held valence electrons in p-orbitals (as in

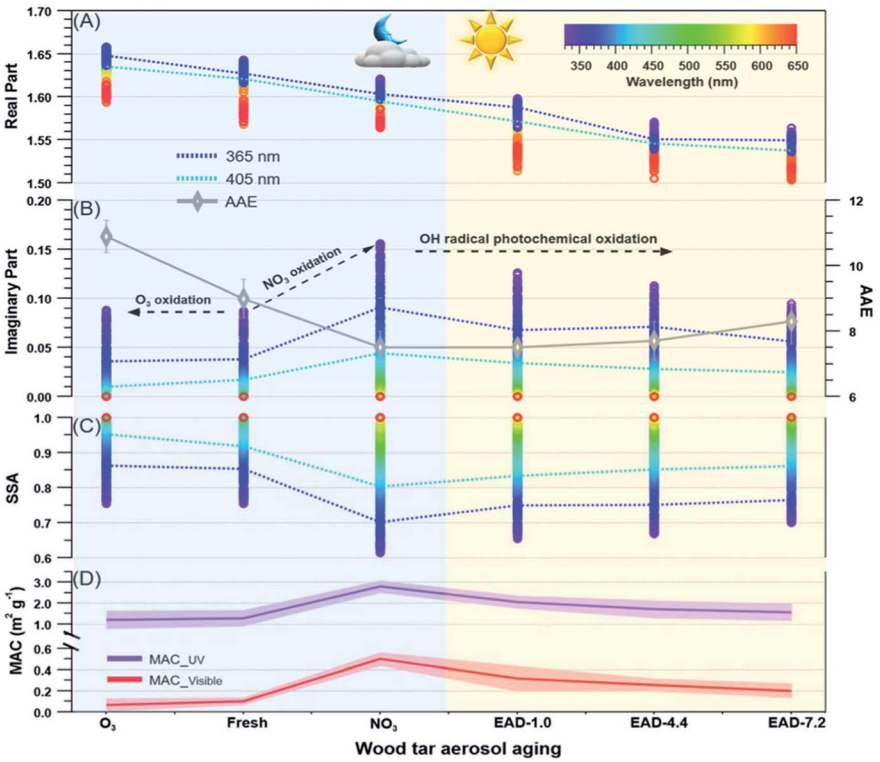

Fig. 28 Optical evolution of wood tar aerosols through various atmospheric aging processes, including O_3 and $NO_3^{\bullet}$ reactions in the dark (gray area: night-time aging simulation) and photochemical transformation of $NO_3^{\bullet}$-aged wood tar aerosols (yellow area: daytime photochemical simulation). (A) Continuous wavelength-dependent complex real refractive index (RI) as a function of atmospheric transformation. (B) Continuous wavelength-dependent complex imaginary RI as a function of atmospheric evolution (left *y*-axis). Absorption Ångström exponent (AAE) was derived to indicate the wavelength dependence of light absorption (right *y*-axis). (C) Wavelength-dependent single-scattering albedo (SSA) was estimated based on retrieved refractive indices (RIs) for wood tar particles at 200 nm. (D) Changes in the wavelength-weighted mean mass absorption coefficient (MAC, $m^2\ g^{-1}$) for wood tar aerosols *via* various atmospheric aging processes. Two categories are shown: near-UV absorption (330–400 nm) and visible absorption (400–550 nm). Uncertainties for each RI and SSA distributions (±0.005 for the real part, ±0.006 for the imaginary part, and ±0.013 for the SSA on average from 330 to 550 nm) are not presented for clarity. The term 'EAD' refers to the experimental hydroxyl radical concentration, which is equivalent to 1.0–7.2 days of ambient daytime oxidation. EAD-1.0 indicates the equivalent to 1.0 day of atmospheric aging and so forth. Reproduced from ref. 302 under Create Commons License (CC BY) from the American Chemical Society, © the Author(s), 2020.

graphite) in addition to hydrogen and oxygen. Bond and Bergstrom[261] suggested a narrow range of refractive indices, as highlighted in Fig. 26 (left), and a mass-normalized absorption cross section of 7.5 ± 1.2 $m^2\ g^{-1}$ at 550 nm for uncoated particles (Fig. 26 (middle)).

Freshly emitted BC has a 'fractal' structure, where nanometer size particles form conglomerates. This material absorbs electromagnetic radiation across a broad spectrum because the energy levels of the loosely held electrons are closely spaced. As highlighted above, BC can be externally or internally mixed within an aerosol population, hence affecting the overall morphology of particles. Terms that highlight the morphological changes of BC particles during atmospheric aging include 'encapsulated', 'inclusions', 'collapsed uncoated' and 'coated'. Fig. 27 shows the changes in morphology with atmospheric aging time leading to an enhancement in MAC and direct radiative forcing (DRF) values based on the experimental evidence by Peng *et al.*[282] MAC values for aged BC are higher than those of fresh/uncoated particles (Fig. 26 middle). In their models,[283] Boucher *et al.*[283] used average values of 11 $m^2\ g^{-1}$ for aged BC particles and argued that converting enhancements to increased DRF is still a work in progress. These enhancements in MAC has been explained by an optical lensing effect due to the coatings. In their review, Samset *et al.*[264] provided a summary table for enhancement in absorption (E_{abs}) as a function of wavelength for three different aging cases studied in the literature: 'pure → fresh', 'fresh → aged' and 'pure → aged', where "pure" refers to uncoated and collapsed BC, "fresh" refers to freshly emitted BC, while "aged" refers to aged BC that has become coated. Table 8 lists these E_{abs} values and the source studies. Zhang *et al.*[284] correlated the E_{abs} values with the chemical composition from field data collected over four seasons and found that the significant wavelength-dependent E_{abs} increase (from 1 to 2) correlated with the aerosol photochemical aging associated with the production of highly oxidized secondary organic aerosols (SOA), especially at summertime. Other factors that contribute to the uncertainty in BC radiative forcing calculations are residence time, vertical profiles and emission inventories.[264]

6.3.3 Brown carbon (BrC). BrC structurally differs from BC resulting in strong absorption at short wavelengths (below 500 nm) with some classes of BrC showing absorption up to 600 nm.[33,264,295,296] Fig. 26 shows the optical parameters and the level of uncertainty associated with each parameter used in predicting the RF of BrC. Factors contributing to this relatively large variability include the structure and effects of atmospheric aging such as lensing, photobleaching and emission inventory. The molecular structure of BrC includes tar balls, HULIS and water-soluble organic carbon (WSOC) with different classes of chromophores such as aromatic carboxylic acids, nitrophenols and substituted, heterocyclic, and pure polycyclic aromatic hydrocarbons.[33,264,295,297,298] Chemical processes that lead to the formation of BrC have been reviewed earlier.[33,295] These structural differences result in variable polarities, volatility,[299] viscosity[300] and hygroscopicity,[301] which affect the reactivity.

The lensing effect that increases the absorption of BrC was found to be larger in internally mixed aerosol with BC than with non-light absorbing organic carbon.[295] On the other hand, in laboratory studies, photobleaching due to irradiation with UV light at 365 nm of low molecular weight BrC was found to occur faster than high molecular weight.[295] Photobleaching involves photolytic and oxidation processes that break C=C and C–N bonds contributing to the light absorption properties of BrC. Simulating the photobleaching of BrC aerosol under realistic conditions using sunlight as the source remains challenging. Li *et al.*[302] conducted lab experiments on the optical and chemical transformations of biomass burning (wood) tar proxy aerosols by nitrate radicals ($NO_3^{\bullet}$) and ozone oxidation in the dark, followed by photolysis and photochemical OH reactions in simulated daytime (Fig. 28). They found that $NO_3^{\bullet}$ reactions form secondary chromophores, such as nitroaromatic compounds and organonitrates, causing an increase in MAC of the aerosols by a factor of 2–3. The subsequent OH oxidation and direct photolysis both decompose chromophores in the $NO_3^{\bullet}$-aged wood tar aerosols, thus decreasing the absorption. Studies by Fleming *et al.*[303] showed that the photodegradation lifetime of BrC depends on the fuel type, which ranges from 3.4 ± 1 for subalpine fir to 14 ± 1 for juniper.

In an attempt to reduce uncertainties associated with predicting RF[304] of BrC, Lu *et al.*[305] developed a method to constrain the BrC absorptivity at the emission inventory level using laboratory and field observations of POA. The main output was wavelength-dependent imaginary refractive indices (k_{OA}) for different fuel types that include the biomass/biofuel, lignite, propane, and oil. The authors acknowledged that the effects of mixing, aging, and SOA formation need to be added to models that estimate the radiative effect of BrC.

6.3.4 BrC from iron chemistry. Using phenolic compounds as precursors, the MAC values for the organic solvent extracts of the brown- to black-colored particles collected on the filters from the aqueous phase reactions of catechol, guaiacol, syringol, and *o*- and *p*-cresol with iron under acidic conditions were recorded by Lavi *et al.*[211] Fig. 29 (left) shows the MAC spectra for comparison with reference compounds, nigrosin, Suwannee River and Pahokee Peat Fulvic Acid (SRFA and pahokee). The solvent used in these measurement was DMSO. At 365 and

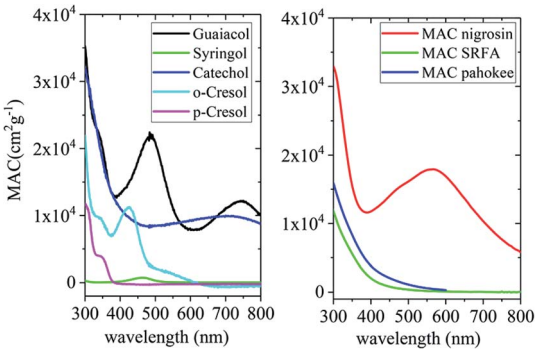

Fig. 29 Mass absorption coefficient in the UV-visible range of products formed in phenol/Fe(III) mixtures (left) and reference compounds (right). The figure and the caption were reproduced from ref. 211 with permission from the American Chemical Society, ©2017.

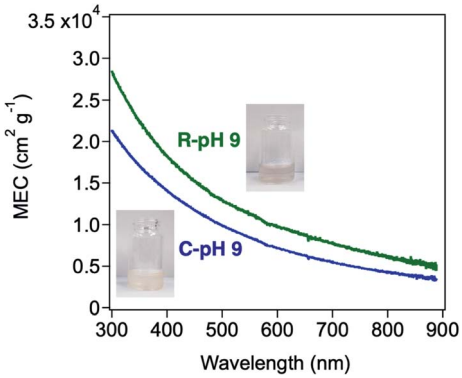

Fig. 30 Mass-normalized extinction coefficient (MEC) spectra as a function of wavelength for diluted AZTD slurries reacted with catechol at pH 9 (R-pH 9) and control at pH 9 (C-pH 9). For the controls, no catechol was added. The insets show digital photographs of the slurries used in the analysis with mass concentrations of 5.6×10^{-5} g cm^{-3} (R-pH 9) and 1×10^{-4} g cm^{-3} (C-pH 9). Reproduced from ref. 206 with permission from the American Chemical Society, © 2020.

405 nm, where absorption coefficients of ambient particles are frequently measured, MAC values for guaiacol reaction products are around 1.5×10^4 cm^2 g^{-1} in DMSO as the solvent (Fig. 29 left) and 2×10^4 cm^2 g^{-1} in water as the solvent.[70] These values are comparable to those from biomass burning aerosols (10^3–10^4 cm^2 g^{-1})[306] and in the same order of magnitude of black carbon[261] (7.5×10^4 m^2 g^{-1} for uncoated soot). In the case of the guaiacol derivative, syringol, no significant absorption was measured for its reaction products with iron.

The MAC spectrum for catechol reaction products also showed relatively high values comparable with guaiacol. For comparison, Slikboer *et al.*[70] reported the MAC spectrum for unfiltered solutions after 3 min of reaction between catechol and Fe(III) at pH 3. The intermediate peak for quinone around 390 nm[70] is absent in Fig. 29 (left). The feature above 500 nm is present in both studies using DMSO and water as solvents, which resembles a similar one observed in the absorption spectrum of a mixture of polyhydroxylated benzene and C–C coupling products from the heterogeneous ozonolysis of a thin solid catechol film.[207] Reaction products of phenol derivatives, *o*- and *p*-cresol, resulted in MAC spectra similar to those collected for SRFA and pahokee fulvic acid reference spectra between 300 and 500 nm, which have been used as model compounds for atmosphere BrC.[33]

Moreover, changes to the optical properties of diluted control and reacted AZTD slurries with catechol were reported by Link *et al.*[206] Fig. 30 shows the mass-normalized extinction coefficient (MEC) calculated in the wavelength range 300–900 nm according to eqn (26):

$$\mathrm{MEC}(\lambda)\ \left(\mathrm{cm}^2\ \mathrm{g}^{-1}\right) = \frac{\ln(10)\cdot\mathrm{extinction}(\lambda)}{\text{mass concentration of AZTD in slurry } \left(\mathrm{g\ cm}^{-3}\right)\cdot\text{path length (cm)}} \quad (26)$$

MEC values for diluted AZTD slurries reacted with catechol at pH 9 (R-pH 9) and control at pH 9 (no catechol, C-pH 9). Although this high pH is not measured in LIQUID WATER, the basic pH is typically measured in the slurries of unprocessed dust due to the presence of metals that act as Lewis acid sites.[123] Hence, it is likely that water adsorbed on freshly emitted dust particles would have a basic pH. The measured MEC values increased in the R-pH 9 sample at all wavelengths in agreement with the observed darkening of the particles by the reaction. This method cannot separate contributions to the increase in MEC driven by the growth of particles due to polycatechol formation, leading to increased scattering and by the deposition of light-absorbing organic material on particles leading to increased absorption. The lack of wavelength-dependent features in the MEC spectrum of the aged samples suggests that the scattering effect dominated the overall extinction.

In the case of BrC formation from aliphatic precursors, Tran *et al.*[69] reported the MAC spectra for the reaction products of fumaric and muconic acids with Fe(III) at pH 3 as a function of reaction time (Fig. 31). As stated earlier, the dark reaction of *trans*-C4 and C6 unsaturated diacids with Fe(III) under acidic conditions and in the absence of any added oxidants resulted in the formation of insoluble and amorphous polymeric particles, Fe-polyfumarate and Fe-polymuconate. At 365 and 405 nm, the observed MAC values after 1 h of reaction were as high as ~6 m^2

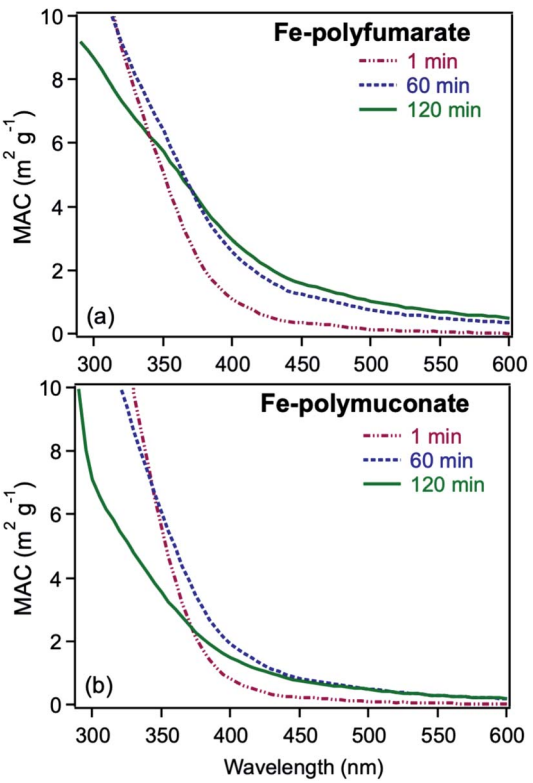

Fig. 31 Mass-normalized absorption coefficient (MAC) plot for the reaction of 0.1 mM concentration of (a) fumaric acid (FA), and (b) muconic acid (MA) with $FeCl_3$ after 1, 60 and 120 min of dark reaction at pH 3 (unfiltered solution). The final reaction mixture contains 1 : 2 molar ratio organic reactant : Fe. MAC values were calculated from eqn (1) and were not corrected for the contribution from scattering by particles in solution. The figure and the caption were reproduced from ref. 69 with permission from the American Chemical Society, ©2017.

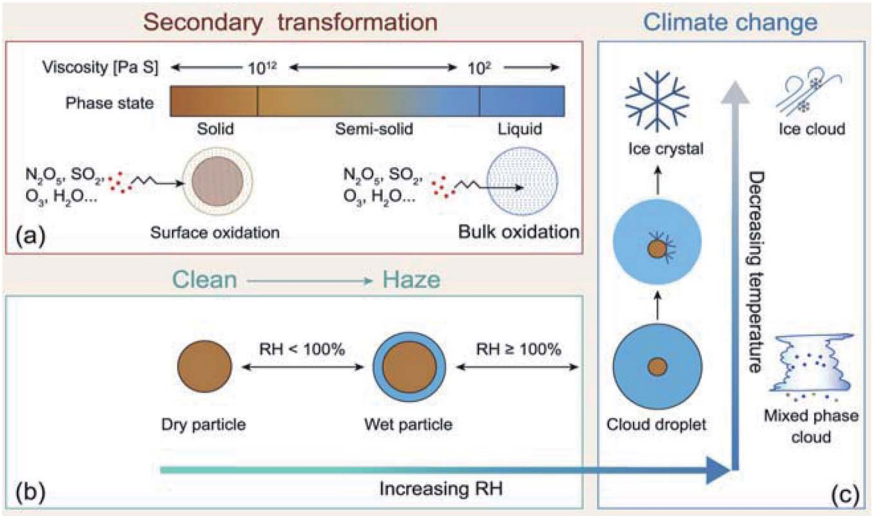

Fig. 32 Interaction of water with atmospheric particles: (a) particle phase transition from solid to liquid with increasing RH; (b) particles taking up water leads to an increase in particle size and mass loading; and (c) particles participate in cloud formation by serving as CCN and IN. Reproduced from ref. 22 with permission from Oxford University Press on behalf of China Science Publishing & Media Ltd, © The Author(s), 2018.

g^{-1} and ~2 m^2 g^{-1}, respectively, and higher than those shown in Fig. 29 for SRFA and pahokee fulvic acid. In the visible range, the observed MAC values drop to ~1 m^2 g^{-1} at 500 nm, but they still remain comparable to or higher than the typical MAC values for biomass burning aerosols. Therefore, the metal driven transformation of phenolic and aliphatic precursors detected in atmospheric aerosols with various degrees of aging is potentially an important pathway for the formation of secondary "brown carbon".

6.4. Hygroscopic properties

Quantifying gas-phase water uptake on atmospheric particles leads to understanding their role in air quality, climate change[22] and health.[23] Fig. 32 shows a general schematic of the effect of RH and temperature on particle phase transitions, surface *versus* bulk chemistry, formation of haze, cloud condensation nuclei (CCN) and ice nuclei (IN).[22] The following sections describe in detail the qualitative and quantitative aspects of aerosol liquid water on aerosol components with various solubilities for understanding the hygroscopic properties of field-collected aerosol particles. As stated above, organics from primary and secondary sources represent a major component of atmospheric aerosols, hence quantifying their hygroscopic properties is important for accurately parametrizing their climate and environmental impacts.

6.4.1 Gas phase water uptake. Iron-catalyzed aqueous phase reactions with catechol, guaiacol, fumaric and muconic acids produced water-insoluble and light-absorbing secondary organics particles, namely polycatechol, polyguaiacol, Fe-polyfumarate and Fe-polymuconate.[69,70] Rahman and Al-Abadleh[307] studied the hygroscopic properties of these particles using diffuse reflectance Fourier infrared transform spectroscopy (DRFITS) and quartz crystal microbalance (QCM) as a function of RH at 298 K. A modified 3-parameter Type II multilayer BET adsorption model described the water adsorption isotherm on the non-porous materials, polycatechol, polyguaiacol and Fe-polymuconate, whereas a Type V adsorption model (the Langmuir–Sips model) that accounts for condensation in pores was used in the case of porous Fe-polyfumarate (Fig. 33). The data revealed that organometallic polymers are more hygroscopic than organic polymers. Fig. 33 shows the water adsorption isotherms on these materials with desorption data as well. The analysis of these data shows that organometallic polymers are more hygroscopic than organic polymers and can retain more water with decreasing RH due to structural differences.

6.4.2 Structure of surface water. There are molecular level structural differences between the bulk and interfacial water on surfaces of atmospheric relevance that have consequences on the extent of water uptake, ice nucleation, ionic mobility, and chemical reactivity.[77] These structural differences arise from changes to the hydrogen bonding network in the condensed phases of water that affect the fundamental vibrational modes of water.[308] The use of experimental and computational tools such as infrared spectroscopy, nonlinear sum frequency generation spectroscopy, X-ray based techniques and molecular dynamics simulations provided invaluable information on the structure of interfacial water. These differences were the subject of thematic special issues of *J. Phys. Chem. C*[309] and *Phys. Chem. Chem. Phys.*310

Gas phase water adsorption on the surfaces of hydrophobic organics like the insoluble polymers formed from iron-catalyzed reactions with aromatic and aliphatic precursors are two examples of insoluble aerosol components, where the uptake of water on their surfaces results in the formation of 'adsorbed water'. Adsorbed water can take the form of either thin films or islands depending on the thermodynamic favourability of hydrogen bonding with the underlying surface. The number of hydrogen bonding donors and acceptors

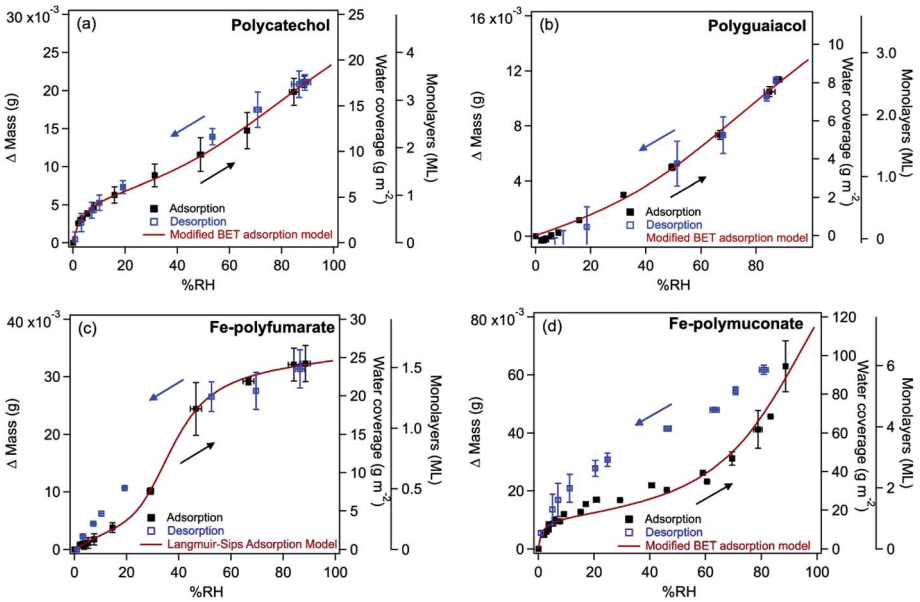

Fig. 33 Water adsorption isotherms at 298 K for (a) polycatechol, (b) polyguaiacol, (c) Fe-polyfumarate, and (d) Fe-polymuconate. The left axis shows Δmass (m), which is the change in mass due to adsorbed water, as measured using the QCM. The right axes were calculated by converting Δm to water mass (g) per surface area (m^2) of the organic film deposited. The lines through the data represent least-squares best fits to the experimental data using the modified BET and the Langmuir–Sips adsorption models. The outermost right axis was obtained by dividing the water coverage in g m^{-2} by that at the monolayer coverage obtained from the best-fit parameters (see ref. 307 for details). Reproduced from ref. 307 under the AuthorChoice License from the American Chemical Society, © 2018.

increase is a strong indicator for the extent of water-surface interactions. Formation of hydrogen bonding in water clusters and liquid and solid phases affects the frequencies and oscillator strengths assigned to stretching, bending and liberational modes of water.[308,311–313] Also, heterogeneity (*i.e.*, ordered *vs.* disordered) of the molecular environment of hydrogen bonded water can be assessed through the OH stretching band shape, which increases in broadness with increasing disorder.[313] The average hydrogen bond coordination number for water molecules in bulk water is ~3.5, which drops to 3.0 at the interface.[314,315]

In general, formation of hydrogen bonds in the liquid and solid bulk phases leads to the formation of broad OH stretching (ν_1, ν_3) and H_2O bending (δ) modes and the appearance of a new combination mode. Table 9 summarizes the frequency values of water in different molecular environments. Hydrogen bonds are random and disordered and weaker in the liquid phase compared to ice, and they lead to shifting the band centre from ~3400 to ~3200 cm^{-1}.[316,317]

For surface water, spectral features are often described as 'liquid-like' and 'ice-like' depending on the interface and the underlying substrate. A more accurate description refers to the strength of the hydrogen bonds: strong hydrogen bonds give rise to broad spectral features lower than 3400 cm^{-1} and weak hydrogen bonds between 3400 and 3500 cm^{-1}. In the case of no hydrogen bonds, the spectral features appear sharp between 3600 and 3750 cm^{-1}.[318] In the case of hydrophobic surfaces, such as hexane and CCl_4, the spectra of water show features assigned to free and bonded OH groups suggesting strong orientation effects.[318] These features were also apparent on tannic acid,[319] polycatechol, polyguaiacol, Fe-polyfumarate, and Fe-polymuconate[307] and pollen.[320] The weak and strong hydrogen bonding networks of adsorbed water on these organic powdered materials suggest cluster formation, reflecting water–water and water–organics interactions. Also, water bonding with organic functional groups acting as hydrogen bond acceptors caused shifts in their vibration modes[307] and led to partial dissolution due to the formation of hydrates, as observed in the case of tannic acid.[319] Water molecules in contact with organic self-assembled monolayers (SAMs) at low RH form clusters, which have fewer hydrogen bonds and gave rise to spectral components at 3200 cm^{-1}, whereas molecules in the interior of water clusters have 3 and 4 hydrogen bonds similar to that of bulk water.[321,322]

6.4.3 Efficiency of cloud condensation nucleation. Kuang *et al.*[44] reviewed the lab and field measurements of CCN activity of SOA and highlighted the factors that affect the degree of organic aerosol hygroscopicity. These factors include the RH; water solubility; degree of atmospheric aging that affects the carbon chain length, functional groups, and oxygen to carbon (O : C) ratio; and surface tension changes due to the presence of surfactants and liquid–liquid phase separation.

To highlight the contribution of the aforementioned factors, the hygroscopic properties of lab-generated semi-solid SOA were measured as a function of RH and oxidation state through quantifying the oxygen to carbon ratio.[326] The SOA were generated in a flow reactor by homogeneous nucleation and condensation following OH and/or O_3 oxidation of gas-phase precursors: isoprene (C_5H_8), α-pinene ($C_{10}H_{16}$), and longifolene ($C_{15}H_{24}$). The hygroscopicity parameter, κ, was

Table 9 Summary of selected studies that utilized infrared spectroscopy for characterizing water in bulk phases, at interfaces and surfaces of atmospheric relevance

	Vibrational modes (cm^{-1})				
	Stretching				
Bulk phase of water	Symmetric (ν_1)	Asymmetric (ν_3)	Combination ($\delta + \nu_R - \nu_T$)	Bending (δ)	Ref.
H_2O(g)	3656	3755	—	1594	311
HDO(g)	3622 (OH), 2723 (OD)	3699 (OH), 2781 (OD)	—	1265	[a]
H_2O(l)	3261	3351	2134	1639	323
$H_2{}^{18}O$(l)	3241	3337	2130	1632	323
HDO(l)	2502	3404	2900 (2δ)	1450	324
D_2O(l)	2407	2476	—	1206	323
H_2O(s)	3289	3411	2243	1641	311

	Adsorbed water vibrational modes (cm^{-1})			
Organic solid surface (powders, films)	Stretching	Combination ($\delta + \nu_R - \nu_T$)	Bending (δ)	Ref.
Pollen	3593, 3205	2135	1616	320
Tannic acid[a]	3600, 3400, 3169	—	1645	319
Humic acid/goethite	3582, 3512, 3491	—	1641	325
Polycatechol	3580, 3020	—	1628	307
Polyguaiacol	3580, 3170		1628	
Fe-polyfumarate	3641, 3564, 3020	—	1632	307
Fe-polymuconate			1628	
C8 and C18 self-assembled monolayers	~3400, ~3180	—	—	321 and 322

[a] Spectrum collected in the author's lab.

measured in the sub- and super-saturation RH regions using a hygroscopicity tandem differential mobility analyzer (HTDMA) and a cloud condensation nuclei counter (CCNc), yielding κ_{HGF} and κ_{CCN}, respectively. The authors calculated the ratio of κ_{HGF} to κ_{CCN} between 0 and 1 to describe a general hygroscopic behavior which is independent of absolute κ-values. κ-Ratios below 0.5 indicate the dominance of water surface adsorption, whereas those above 0.5 indicate increased solubility and higher water uptake. The phase of the SOA particles (solid, semisolid, and liquid) was quantified using an aerosol bounce instrument that yields a particle bounced fraction (BF). Particles with BF > 0 are solid or semisolid and the particles with BF = 0 behave mechanically as liquids.[326] For comparison, similar experiments were conducted using solid and insoluble SiO_2 spheres where water uptake occurs *via* surface adsorption. Fig. 34 shows a schematic that summarizes their major findings: for subsaturated conditions (RH < 100%), the water uptake of SOA with relatively low O : C (<0.6) is an adsorption-dominated process. With increasing atmospheric aging due to oxidation and increasing RH, the dissolution increases and the κ-ratio approaches 1 similar to supersaturation conditions. The authors also found that the organic precursor has an effect on the hygroscopic properties, even if the SOA O : C ratio is similar. For example, for an O : C ratio of ~0.6, a-pinene SOA would have a κ-ratio of 0.82, whereas the κ-ratio for longifolene SOA is around 0.4.

Moreover, in addition to dissolution, the type of VOC precursor, and RH, Rastak *et al.*[327] found that liquid–liquid phase separation can take place in some SOA originating from biogenic emissions with increasing RH. Fig. 35 show optical microscopy images for micrometer-scale isoprene- and α-pinene-SOA generated in the lab from photo-oxidation and ozonolysis, respectively. The SOA products were collected on a hydrophobic glass slide for collecting images at 290 K in a temperature- and RH-controlled flow cell. The presence of multiple phases is visible in the optical images. One single phase was observed over the entire RH range for isoprene-SOA, as shown in Fig. 35A, whereas for α-pinene-SOA (Fig. 35B), a single organic-rich phase is observed below 95%. Increasing the RH above 95% results in phase separation, where a water-rich phase is observed. The authors found agreement between the microscopy images and the water uptake of considerably smaller 100 nm SOA particles generated in the lab from isoprene and α-pinene. It was noted that as the O : C ratio of monoterpene-SOA changed with atmospheric aging, its hygroscopicity and CCN activity would resemble more of those of oxidized isoprene-SOA. Improved thermodynamic model predictions of κ_{HGF} were obtained when liquid–liquid phase separation was included to explore the effect of surface tension reduction by organics, as well as the coupled gas–particle partitioning of semi-volatile organic molecules and water upon RH changes.[327] In the case of secondary marine aerosol consisting of sulfate, ammonium, and organic species, Mayer *et al.*[328] found that the measured CCN activity ($\kappa_{app} = 0.59 \pm 0.04$) of the resulting secondary marine aerosol matched the values observed in previous field studies. Although these secondary

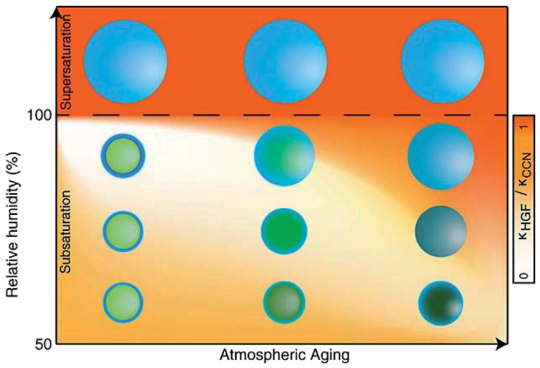

Fig. 34 Schematics of the water uptake processes of SOA particles in the atmosphere. Subsaturated swelling (κ_{HGF}) can vary dramatically with minor differences in supersaturated droplet activation (κ_{CCN}); consequently, particles can have very different direct and indirect climate effects. The background color scale indicates the ratio of these parameters under the given subsaturated and supersaturated conditions, whereas the darkness of the green color in particles denotes their atmospheric age. The contrast is the largest when adsorption is the dominant water uptake mechanism even at high RH. This is the case for low O : C SOA particles on the left. With increasing oxidation, *i.e.*, increasing atmospheric age of the particles, the solubility increases and the dissolution RH decreases, decreasing the discrepancy between the κ_{HGF} and κ_{CCN} values. Reproduced from ref. 326 under Create Commons License (CC BY-NC-ND 4.0) from the American Geophysical Union, © The Authors, 2015.

particles correlate with phytoplankton biomass (*i.e.*, chlorophyll-a concentrations), primary sea spray aerosol does not. Importantly, the authors concluded that secondary marine aerosols play a dominant role in affecting marine cloud properties.[328]

6.4.4 Ice nucleation. Understanding the role of atmospheric aerosols in cloud and ice nucleation remains at the core of minimizing uncertainties associated with the indirect effect of aerosols on the climate and the hydrological cycle. Selected recent reviews that recount the literature on the influence of aerosol chemical composition and atmospheric processes on the CCN and IN activities can be found in ref. 329–332. These reviews highlight the role of ice nucleating particles (INPs) in heterogeneous freezing, which takes place at much higher (*i.e.*, warmer) temperatures than that required for homogeneous nucleation (<−38 °C or 235 K), and lower saturation with respect to ice (<1.5), as illustrated in Fig. 36.[331] Table 10 lists the brief definition of the different heterogeneous freezing processes provided by Kanji *et al.*[330]

Following decades of research, aerosols that make effective INPs have been grouped into four categories: (a) insoluble/solid inorganic particles, (b) soluble particles, (c) organics and glassy particles, and (d) nanoscale biological fragments.[330] The chief examples of category (a) are mineral dust, fly and volcanic ash, K-feldspars, metal and metal oxides, and soil dust, where experiments have shown that factors such as the surface area, surface functional groups, surface defects, lattice match of surface planes with that of ice. A few highlights from selected recent studies include the following: DeMott *et al.*[334] developed an empirical parameterization for the immersion freezing activity of natural mineral dust particles from both laboratory studies and atmospheric measurements. The dependence of immersion mode ice nucleating ability of K-feldspars

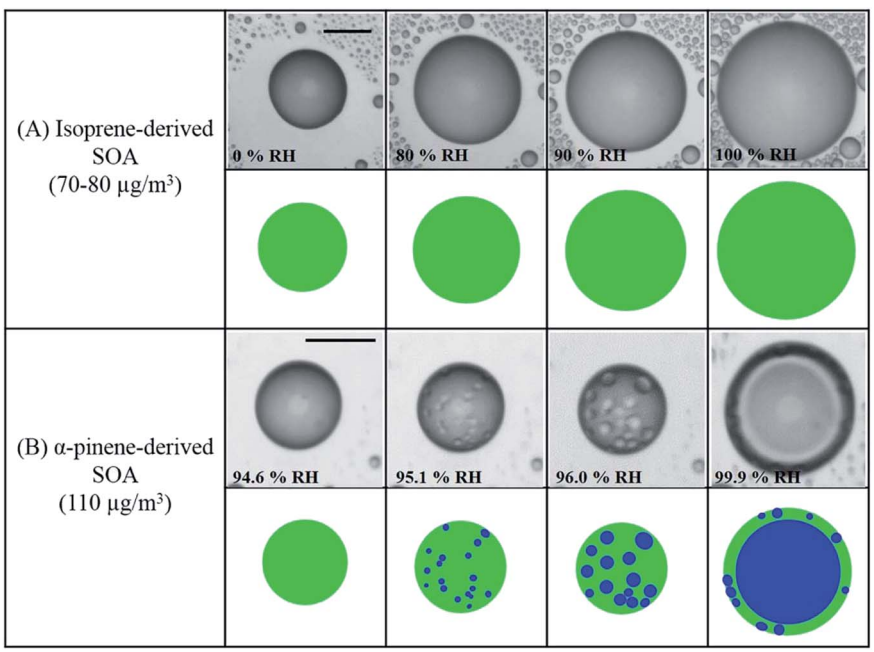

Fig. 35 Optical images of micrometer scale SOA particles with increasing relative humidity. (a) Isoprene-derived SOA for mass concentrations of 70–80 μg m^{-3} and (b) α-pinene-derived SOA for a mass concentration of 110 μg m^{-3}. Note that the light gray circles at the center of the particles are due to an optical effect caused by the hemispherical shape of the particles deposited on a substrate. Illustrations are shown below the images for clarity. Green: organic-rich phase. Blue: water-rich phase. The scale bar represents 20 μm. Reproduced from ref. 327 under Create Commons License (CC BY-NC-ND 4.0) from the American Geophysical Union, © The Authors, 2017.

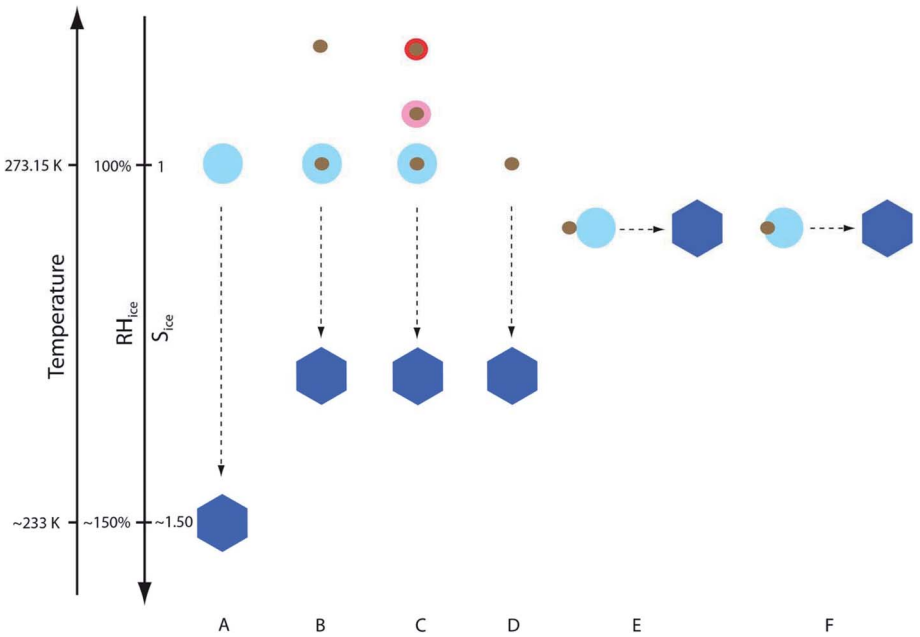

Fig. 36 Schematic overview of different ice nucleation pathways, exemplarily given as functions of temperature, relative humidity, and supersaturation with respect to ice (RH_{ice} and S_{ice}, respectively). (A) Homogeneous ice nucleation, (B) immersion freezing, (C) deliquescence and water uptake, followed by immersion freezing, (D) deposition ice nucleation, (E) contact ice nucleation, and (F) inside-out freezing. Symbol forms and sizes are not to scale. Reprinted (adapted) from ref. 331 with permission from the American Chemical Society, © 2020.

(containing 85% microcline ($KAlSi_3O_8$) and 15% albite ($NaAlSi_3O_8$)) on the surface composition was investigated by Yun *et al.*[335] to account for the effect of water-soluble inorganic solutes at low concentrations. Their study found that only K^+(aq) had a positive effect (*i.e.*, warming effect) on the ice nucleating ability of K-feldspar, while the other alkali cations, namely Li^+, had no effect, and Na^+, Rb^+, and Cs^+ had a negative effect. This trend correlated with the K/Al ratio at the surface of K-rich feldspar. Whale *et al.*[336] investigated the immersion mode enhancement and the suppression of ice nucleation of feldspars, humic acid, quartz, amorphous silica gel, and AZTD with other alkali halides and ammonium salts. Chatre *et al.*[337] showed that increasing the mole fraction of citric acid when AZTD is present increased the ice crystallization temperature compared to AZTD only. The effect of porosity of coal fly ash aerosol particles on their IN activity at cirrus temperatures was demonstrated by Umo *et al.*[333] to highlight the dominance of pore condensation and freezing processes in these systems.

In the case of soluble particles such as INPs, this class contains hygroscopic salts such as ammonium sulfate and sodium chloride, which can crystallize by efflorescence. The ice nucleating ability of these salts has been extensively studied and reviewed by Kanji *et al.*[330] Laboratory studies showed that supermicron and submicron salt particles induce heterogeneous ice nucleation *via* contact freezing. Pure soluble organics such as citric acid were found to promote ice nucleation near

Table 10 Brief definition of the heterogeneous freezing processes provided by Kanji *et al.*[330] and Knopf *et al.*[331]

Term	Definition
Immersion freezing	Ice nucleation initiated by an INP immersed in an aqueous solution or water droplets *via* activation of CCN during cloud formation. This process is suggested to be the most important for mixed phase clouds
Deposition ice nucleation	Ice forms on an INP from the supersaturated gas phase (*i.e.*, RH_{ice} > 100%). Liquid water is presumed to be absent
Condensation freezing	Freezing being initiated concurrently with the initial formation of liquid on CCN at supercooled temperatures
Contact ice nucleation	Ice nucleation occurs when an INP collides or comes into contact with a supercooled water or aqueous solution droplet
Inside-out freezing	Freezing occurs when an INP is in contact with the liquid–air interface, establishing three interfaces (*i.e.*, gas, solid, and liquid), under supercooled conditions
Pore condensation and freezing[333]	Ice formation is initiated at cirrus temperatures *via* the liquid phase in a two-step process involving the condensation and freezing of supercooled water inside pores

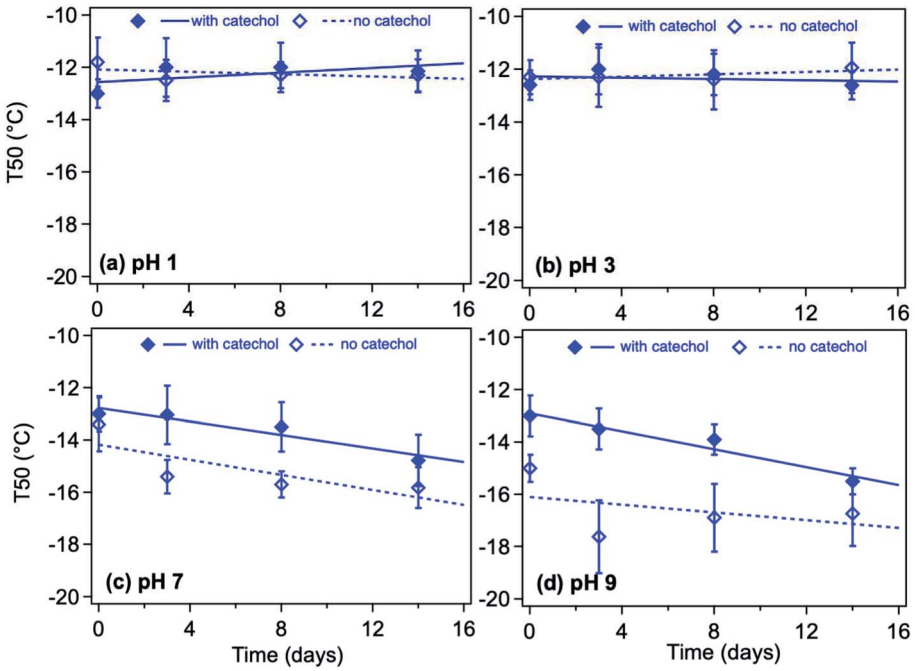

Fig. 37 Ice nucleation efficiency as gauged by T_{50} values as functions of time and starting pH of reaction and control AZTD slurries. Error bars in T_{50} represent propagated $\pm 2\sigma$. The figure and the caption were reproduced from ref. 206 with permission from the American Chemical Society, © 2020.

homogeneous freezing temperatures, $T < -40$ °C, when amorphous glass-like species form.[330] Studies to date concluded that salt mixtures with organics affect the ice nucleating abilities of these systems in an unclear way because of variations in chemical composition and functional groups, phase, and morphology[338] compared to single component salt systems. In their modeling study, Yun and Penner[339] found that marine organic aerosol contributes to more ice formation than dust or black carbon/organic matter in mixed-phase clouds and highlighted their inclusion as natural heterogeneous ice nuclei reduced the magnitude of the total top-of-atmosphere anthropogenic aerosol force by 0.3 W m^{-2}. The review by Knopf *et al.*[331] examined in detail the current state of knowledge of the ice nucleating ability of organic matter in atmospheric aerosols with additional details in ref. 330 and highlighted the need for molecular level investigations to better understand the underlying mechanisms affecting organic ice nucleating abilities, particularly the structure of ice and nature of hydrogen bonding on different organic surfaces, as done for mineral clays and metal oxides.[340]

The impacts of solution pH and the extent of polycatechol formation on AZTD ice nucleation efficiency were investigated by Link *et al.*[206] using the droplet freezing technique. In these experiments, microliter droplets were placed on a hydrophobic glass slide on the top of a temperature-controlled cooling stage with a cover equipped with a digital camera. The 'frozen fraction' was calculated from the images, which corresponds to the percentage of droplets that froze at a given temperature. The temperature that corresponds to the 50% frozen fraction is called 'T_{50}' and is used as a measure of the ice nucleation efficiency of different samples. Fig. 37 shows T_{50} values as a function of time and pH for the control and reaction vials of AZTD (*i.e.*, with and without catechol) over a 14 d period. The data in Fig. 37 show that polycatechol did not significantly impact ice nucleation or block ice nucleation sites on AZTD. The lack of a strong effect of polycatechol on T_{50} values of reacted AZTD means that polycatechol either not completely blocks the AZTD surface or is also efficient at nucleating ice. The T_{50} of polycatechol only was reported at -17.7 ± 0.8 °C, which is reproducibly lower than the T_{50} values for AZTD with polycatechol in all cases ($T_{50} > -17$ °C). This conclusion suggests that polycatechol did not completely block the AZTD surface.

The data in Fig. 37 show that in the absence of catechol, increasing pH decreased the ice nucleation ability of AZTD. The shift in T_{50} values of 3.8 ± 1.3 and 4.7 ± 1.6 °C, respectively, due to more basic pH might be explained by the change in the protonation state of the surface of the minerals identified in AZTD. The impairment of freezing efficiency of AZTD under the basic condition can be expected, since studies[341,342] have shown that the freezing efficiency of potassium-rich feldspar and quartz was suppressed under alkaline conditions, and feldspars and quartz make up a significant portion (nearly 50% in total) of the AZTD samples investigated.

7. Summary and outlook

This review recounted the current state of knowledge of iron chemistry in multicomponent atmospheric aerosol systems containing ubiquitous phenolic compounds, dicarboxylic acids, ammonium sulfate and ammonium nitrate that lead to efficient brown carbon formation in the aqueous phase. This chemistry was shown to take place using extracts of BBOA and to change

the optical properties and mixing states of dust and hematite particles. Since reactive oxygen species are generated in the presence of iron, as shown in the mechanism of brown carbon formation from aromatic precursors, the atmospheric importance of these reactions can only be assessed by comparing to the HOx source strength. The laboratory studies summarized here highlight the need for additional systematic experiments that focus on the (1) effect of specific burning conditions and the nature of the fuel on the BBOA particle composition and its aqueous phase extract. This way, the extent of the reactivity of iron with organics producing BrC would be better predicted, (2) kinetics of the Fe(III)/Fe(II) cycling in reaction systems that produce BrC. This cycling of redox species can be followed by flow injection analysis and also online monitoring by continuous flow analysis,[343,344] where the concentrations of Fe(II) and total Fe after the reduction of Fe(III) can be determined on the basis of the color of the reaction, (3) effect of organic compounds that do not form complexes with Fe(III) but can scavenge the ROS species that form *in situ* from the cycling of Fe(III)/Fe(II) in the presence of dissolved oxygen such as the OH radical.[345] These organic compounds could indirectly limit the extent of the chemistry leading to colored product formation, (4) changes to the size, mixing state, and optical properties of suspended aqueous microdroplets containing soluble iron due to the gas phase uptake of semivolatile phenolic compounds, and (5) mechanisms of how soluble and insoluble products summarized here affect the aqueous phase chemistry. The results of these experiments would then be compared with similar ones conducted in a beaker or with thin films to explore the effect of micro- and nano-level reaction environments on the products.

Moreover, the research summarized in this review highlights the need to strategically design field campaigns that (1) track the processing of iron-containing particles in polluted areas or those impacted by biomass burning emissions and (2) explore the changes to iron speciation and fate upon deposition of iron containing secondary particles to the ocean surface microlayer.[21] The atmospheric chemistry models need to incorporate reactions of iron with organics that lead to particle formation and not only soluble complexes. These models could also impart knowledge for planning new laboratory studies and field measurements to minimize uncertainty associated with pathways that lead to SOA and BrC formation and aging.

Author contributions

H. A. A. conceived the idea and organization of this review and fully wrote the manuscript.

Conflicts of interest

There are no conflicts to declare.

Acknowledgements

The author acknowledges contributions to experiments and data analysis from students at Laurier, the University of California Irvine (UCI), the University of British Columbia (UBC), the University of Kentucky (UKY), and the University of Maryland (UMD). Also, the author is grateful to the stimulating discussions and fruitful collaborations with professor Sergey Nizkorodov (UCI), professor Allan Bertram (UBC), professor Nicholas Meskhidze (North Carolina State University), professor Marcelo Guzman (UKY), professor Sasho Gligorovski (Chinese Academy of Science) and professor Akua Asa-Awuku (UMD). Financial support to the atmospheric chemistry research program in the author's lab was provided by Wilfrid Laurier University, Natural Science and Research Council of Canada (NSERC) Discovery, Canadian Foundation for Innovation Leaders Opportunities Fund (CFI-LOF), and the Fulbright Canada Visiting Research Chair Program at UCI.

References

1 O. Boucher, D. Randall, P. Artaxo, C. Bretherton, G. Feingold, F. Forster, V.-M. Kerminen, Y. Kondo, H. Liao, U. Lohmann, P. Rasch, S. K. Satheesh, S. Sherwood, B. Stevens and X. Y. Zhang, in *Climate Change 2013: the Physical Science Basis. Contribution of Working Group I to the Fifth Assessment Report of the Intergovernmental Panel on Climate Change*, ed. T. F. Stocker, D. Qin, G.-K. Plattner, M. Tignor, S. K. Allen, J. Boschung, A. Nauels, Y. Xia, V. Bex and P. M. Midgley, Cambridge University Press, Cambridge, United Kingdom and New York, NY, USA, 2013, pp. 571–657.

2 J. Heintzenberg, F. Raes and S. E. Schwartz, in *Atmospheric Chemistry in a Changing World - an Integration and Synthesis of a Decade of Tropospheric Chemistry Research*, ed. G. Brasseur, R. G. Prinn and A. A. P. Pszenny, Springer, Berlin, 2003, pp. 125–156.

3 B. J. Finlayson-Pitts and J. N. Pitts Jr, *Chemistry of the Upper and Lower Atmosphere*, Academic Press, New York, 2000.

4 J. H. Seinfeld and S. N. Pandis, *Atmospheric Chemistry and Physics: from Air Pollution to Climate Change*, Wiley, New York, 2006.

5 C. Tomasi and A. Lupi, in *Atmospheric Aerosols: Life Cycles and Effects on Air Quality and Climate*, ed. C. Tomasi, S. Fuzzi and A. Kokhanovsky, Wiley-VCH Verlag GmbH & Co., Weinheim, Germany, 2016, ch. 1, pp. 1–86.

6 O. Boucher, *Atmospheric Aerosols: Properties and Impacts*, Springer, France, 2015.

7 V.-M. Kerminen, X. Chen, V. Vakkari, T. Petaja, M. Kulmala and F. Bianchi, *Environ. Res. Lett.*, 2018, **13**, 1–38.

8 S. Philip, R. V. Martin, G. Snider, C. L. Weagle, A. van Donkelaar, M. Brauer, D. K. Henze, Z. Kilmont, C. Venkataraman, S. K. Guttikunda and Q. Zhang, *Environ. Res. Lett.*, 2017, **12**, 1–7.

9 S. A. Weichenthal, K. G. Pollitt and P. J. Villeneuve, *Environ. Health*, 2013, **12**, 1–8.

10 W. Shi, T. Li, Y. Zhang, Q. Sun, C. Chen, J. Wang, J. Fang, F. Zhao, P. Du and X. Shi, *Environ. Sci. Technol.*, 2020, **54**, 16006–16016.

11 P. J. Landrigan, R. Fuller, N. J. R. Acosta, O. Adeyi, R. Arnold, N. Basu, A. B. Baldé, R. Bertollini, S. Bose-O'Reilly,

J. I. Boufford, P. N. Breysse, T. Chiles, C. Mahidol, A. M. Coll-Seck, M. L. Cropper, J. Fobil, *et al.*, *Lancet*, 2018, **391**, 462–512.

12 M. Bruggemann, R. Xu, A. Tilgner, K. C. Kwon, A. Mutzel, H. Y. Poon, T. Otto, T. Schaefer, L. Poulain, M. N. Chan and H. Herrmann, *Environ. Sci. Technol.*, 2020, **54**, 3767–3782.

13 Y. B. Lim, H. Kim, J. Y. Kim and B. J. Turpin, *Atmos. Chem. Phys.*, 2016, **16**, 12631–12647.

14 M. K. Shrivastava, C. D. Cappa, J. Fan, A. H. Goldstein, A. B. Guenther, J. L. Jimemez, C. Kuang, A. Laskin, S. T. Martin, N. L. Ng, T. Petaja, J. R. Pierce, P. J. Rasch, P. Roldan, J. H. Seinfeld, J. E. Shilling, J. N. SMith, J. A. Thornton, R. Volkamer, J. Wang, D. R. Worsnop, R. A. Zaveri, A. Zelenyuk and Q. Zhang, *Rev. Geophys.*, 2017, **55**, 509–559, DOI: 10.1002/2016RG000540.

15 M. Hallquist, J. C. Wenger, U. Baltensperger, Y. Rudich, D. Simpson, M. Claeys, J. Dommen, N. M. Donahue, C. George, A. H. Goldstein, J. F. Hamilton, H. Herrmann, T. Hoffmann, Y. Iinuma, M. Jang, M. E. Jenkin, J. L. Jimenez, A. Kiendler-Scharr, W. Maenhaut, G. McFiggans, T. F. Mentel, A. Monod, A. S. H. Prevot, J. H. Seinfeld, J. D. Surratt, R. Szmigielski and J. Wildt, *Atmos. Chem. Phys.*, 2009, **9**, 5155–5236.

16 A. L. Steiner, *Acc. Chem. Res.*, 2020, **53**, 1260–1268.

17 R. M. Hoesly, S. J. Smith, L. Feng, Z. Klimont, G. Janssens-Maenhout, T. Pitkanen, J. J. Seibert, L. Vu, R. J. Andres, R. M. Bolt, T. C. Bond, L. Dawidowski, N. Kholod, J. Kurokawa, M. Li, L. Liu, Z. Lu, M. C. P. Moura, P. R. O'Rourke and Q. Zhang, *Geosci. Model Dev.*, 2018, **11**, 369–408.

18 D. J. Jacob, *Introduction to Atmospheric Chemistry*, Princeton University Press, Princeton, NJ, 1999.

19 M. Kanakidou, S. Myriokefalitakis and K. Tsigaridis, *Environ. Res. Lett.*, 2018, **13**, 063004, 063001–063022.

20 N. Mahowald, *Science*, 2011, **334**, 794–796.

21 N. Meskhidze, C. Volker, H. A. Al-Abadleh, K. Barbeau, M. Bressac, C. Buck, R. M. Bundy, P. L. Croot, Y. Feng, A. Ito, A. M. Johansen, W. M. Landing, J. Mao, S. Myriokefalitakis, D. Ohnemus, B. Pasquier and Y. Ye, *Mar. Chem.*, 2019, **217**, 103704, 103701–103716.

22 Z. Wu, J. Chen, Y. Wang, Y. Zhu, Y. Liu, B. Yao, Y. Zhang and M. Hu, *Natl. Sci. Re*, 2018, **5**, 452–454.

23 T. V. Vu, J. M. Delagad-Saborit and R. M. Harrison, *Air Qual., Atmos. Health*, 2015, **8**, 429–440.

24 P. H. McMurry, *Atmos. Environ.*, 2000, **34**, 1959–1999.

25 *Aerosol Measurement: Principles, Techniques and Applications*, ed. P. Kulkarni, P. A. Baron and K. Willeke, Wiley, New Jersey, 2011.

26 *Fundamentals and Applications in Aerosol Spectroscopy*, ed. R. Signorell and J. P. Reid, CRC Press, Boca Raton, 2011.

27 A. P. Ault and J. L. Axson, *Anal. Chem.*, 2017, **89**, 430–452.

28 M. Tang, C. K. Chan, Y. J. Li, H. Su, Q. Ma, Z. Wu, G. Zhang, Z. Wang, M. Ge, M. Hu, H. He and X. Wang, *Atmos. Chem. Phys.*, 2019, **19**, 12631–12686.

29 N. Hiranuma, S. Augustin-Bauditz, H. Bingemer, C. Budke, J. Curtius, A. Danielczok, K. Diehl, K. Dreischmeier, M. Ebert, F. Frank, N. Hoffmann, K. Kandler, A. Kiselev, T. Koop, T. Leisner, O. Mohler, B. Nillius, A. Peckhaus, D. Rose, S. Weinbruch, H. Wex, Y. Boose, P. J. DeMott, J. D. Hader, T. C. J. Hill, Z. A. Kanji, G. R. Kulkarni, E. J. T. Levin, C. S. McCluskey, M. Murakami, B. J. Murray, D. Niedermeier, M. D. Petters, D. O'Sullivan, A. Saito, G. P. Schill, T. Tajiri, M. A. Tolbert, A. Welti, T. F. Whale, T. P. Wright and K. Yamashita, *Atmos. Chem. Phys.*, 2015, **15**, 2489–2518.

30 S. Garimella, T. B. Kristensen, K. Ignatius, A. Welti, J. Voigtlander, G. R. Kulkarni, F. Sagan, G. L. Kok, J. Dorsey, L. Nichman, D. A. Rothenberg, M. Rosch, A. C. R. Kirchgabner, R. Ladkin, H. Wex, T. W. Wilson, L. A. Ladino, J. P. D. Abbatt, O. Stetzer, U. Lohmann, F. Stratmann and D. J. Cziczo, *Atmos. Chem. Phys.*, 2016, **9**, 2781–2795.

31 N. Riemer, A. P. Ault, M. West, R. L. Craig and J. H. Curtis, *Rev. Geophys.*, 2019, **57**, 187–249.

32 A. Laskin, R. C. Moffet and M. K. Gilles, *Acc. Chem. Res.*, 2019, **52**, 3419–3431.

33 A. Laskin, J. Laskin and S. A. Nizkorodov, *Chem. Rev.*, 2015, **115**, 4335–4382.

34 J. P. Reid, A. K. Bertram, D. O. Topping, A. Laskin, S. T. Martin, M. D. Petters, F. D. Pope and G. Rovelli, *Nat. Commun.*, 2018, **9**, 1–14.

35 Y. You, M. L. Smith, M. Song, S. T. Martin and A. K. Bertram, *Int. Rev. Phys. Chem.*, 2014, **33**, 43–77.

36 H. O. T. Pye, A. Nenes, B. Alexander, A. P. Ault, M. C. Barth, S. L. Clegg, J. L. Collett Jr, K. M. Fahey, C. J. Hennigan, H. Herrmann, M. Kanakidou, J. T. Kelly, I.-T. Ku, V. F. McNeill, N. Riemer, T. Schaefer, G. Shi, A. Tilgner, J. T. Walker, T. Wang, R. Weber, J. Xing, R. A. Zaveri and A. Zuend, *Atmos. Chem. Phys.*, 2020, **20**, 4809–4888.

37 M. A. Freedman, E.-J. E. Ott and K. E. Marak, *J. Phys. Chem. A*, 2019, **123**, 1275–1284.

38 M. V. Johnston and D. E. Kerecman, *Annu. Rev. Anal. Chem.*, 2019, **12**, 247–274.

39 R. M. B. O. Duarte and A. C. Duarte, in *Ann. Rep. NMR Spec.*, ed. G. A. Webb, 2017, vol. 92, ch. 2, pp. 83–135.

40 S.-H. Lee and H. C. Allen, *Anal. Chem.*, 2012, **84**, 1196–1201.

41 K. M. Prather, C. D. Hatch and V. H. Grassian, *Annu. Rev. Anal. Chem.*, 2008, **1**, 485–514.

42 P. A. Solomon, M. P. Fraser and P. Herckes, in *Aerosol Measurement: Principles, Techniques, and Applications*, ed. P. Kulkarni, P. A. Baron and K. Willeke, John Wiley & Sons, Inc., Hoboken, NJ, 3rd edn, 2011, ch. 9, pp. 153–177.

43 G. Myhre, B. H. Samset, M. Schulz, Y. Balkanski, S. Bauer, T. K. Berntsen, H. Bian, N. Bellouin, M. Chin, T. Diehl, *et al.*, *Atmos. Chem. Phys.*, 2013, **13**, 1853–1877.

44 Y. Kuang, W. Xu, J. Tao, N. Ma, C. Zhao and M. Shao, *Currrent Poll. Rep.*, 2020, **6**, 410–424.

45 S. T. Martin, *Chem. Rev.*, 2000, **100**, 3403–3454.

46 L. J. Mauer and L. S. Taylor, *Annu. Rev. Food Sci. Technol.*, 2010, **1**, 41–63.

47 U. K. Krieger, C. Marcolli and J. P. Reid, *Chem. Soc. Rev.*, 2012, **41**, 6631–6662.

48 M. Bilde, K. Barsanti, M. Booth, C. D. Cappa, N. M. Donahue, E. U. Emanuelsson, G. McFiggans, U. K. Krieger, C. Marcolli, D. O. Topping, *et al.*, *Chem. Rev.*, 2015, **115**, 4115–4156.
49 A. K. Bertram, S. T. Martin, S. J. Hanna, M. L. Smith, A. Bodsworth, Q. Chen, M. Kuwata, A. Liu, Y. You and S. R. Zorn, *Atmos. Chem. Phys.*, 2011, **11**, 10995–11006.
50 P. S. Monks, *Chem. Soc. Rev.*, 2005, **34**, 376–395.
51 S. S. Brown, T. B. Ryerson, A. G. Wollny, C. A. Brock, R. Peltier, A. P. Sullivan, R. J. Weber, W. P. Dube, M. Trainer, J. F. Meagher, F. C. Fehsenfeld and A. R. Ravishankara, *Science*, 2006, **311**, 67–80.
52 J. Kleffmann, *ChemPhysChem*, 2007, **8**, 1137–1144.
53 R. Atkinson and J. Arey, *Chem. Rev.*, 2003, **103**, 4605.
54 H. Chen, M. E. Varner, B. Gerber and B. J. Finlayson-Pitts, *J. Phys. Chem. B*, 2016, **120**, 1526–1536.
55 D. M. Cwiertny, M. A. Young and V. H. Grassian, *Annu. Rev. Phys. Chem.*, 2008, **59**, 27–51.
56 C. George, M. Ammann, B. D'Anna, D. J. Donaldson and S. A. Nizkorodov, *Chem. Rev.*, 2015, **115**, 4218–4258.
57 D. J. Donaldson and K. T. Valsaraj, *Environ. Sci. Technol.*, 2010, **44**, 865–873.
58 I. J. George and J. P. D. Abbatt, *Nat. Chem.*, 2010, **2**, 713–722.
59 E. Harris, B. Sinha, D. van Pinxteren, A. Tilgner, K. W. Fomba, J. Schneider, A. Roth, T. Gnauk, B. Fahlbusch, S. Mertes, T. Lee, J. Collett, S. Foley, S. Borrmann, P. Hoppe and H. Herrmann, *Science*, 2013, **340**, 727–730.
60 Q. Chen, T. Sherwen, M. Evans and B. Alexander, *Atmos. Chem. Phys.*, 2018, **18**, 13617–13637.
61 D. J. Donaldson and V. Vaida, *Chem. Rev.*, 2006, **103**, 4717–4729.
62 R. Zhao, A. K. Y. Lee, C. Wang, F. Wania, J. P. S. Wong, S. Zhou and J. P. D. Abbatt, in *Advances in Atmospheric Chemistry*, ed. J. R. Barker, A. L. Steiner and T. J. Wallington, World Scientific, New Jersey, 2019, vol. 2, ch. 2, pp. 95–184.
63 J. H. Kroll and J. H. Seinfeld, *Atmos. Environ.*, 2008, **42**, 3593–3624.
64 S. M. Murphy, A. Sorooshian, J. H. Kroll, N. L. Ng, P. S. Chhabra, C. Tong, J. D. Surratt, E. Knipping, R. C. Flagan and J. H. Seinfeld, *Atmos. Chem. Phys.*, 2007, **7**, 2313–2337.
65 N. M. Donahue, A. L. Robinson, E. R. Trump, I. Riipinen and J. H. Kroll, in Atmospheric and Aerosol Chemistry, *Topics in Current Chemistry*, ed. V. F. McNeill and P. Ariya, Springer, Berlin, Heidelberg, 2012, vol. 339, pp. 97–143.
66 H. Herrmann, T. Schaefer, A. Tilgner, S. A. Styler, C. Weller, M. Teich and T. Otto, *Chem. Rev.*, 2015, **115**, 4259–4334.
67 C. R. C. R. Hoyle, C. C. Fuchs, E. Järvinen, H. Saathoff, A. Dias, I. El Haddad, M. Gysel, S. C. Coburn, J. Tröstl, A.-K. Bernhammer, F. Bianchi, M. Breitenlechner, J. C. J. C. Corbin, J. Craven, N. M. Donahue, J. Duplissy, S. Ehrhart, C. Frege, H. Gordon, N. Höppel, M. Heinritzi, T. B. Kristensen, U. Molteni, L. Nichman, *et al.*, *Atmos. Chem. Phys.*, 2016, **16**, 1693–1712.
68 A. Al Nimer, L. Rocha, M. A. Rahman, S. A. Nizkorodov and H. A. Al-Abadleh, *Environ. Sci. Technol.*, 2019, **53**, 6708–6717.
69 A. Tran, G. William, S. Younus, N. N. Ali, S. L. Blair, S. A. Nizkorodov and H. A. Al-Abadleh, *Environ. Sci. Technol.*, 2017, **51**, 9700–9708.
70 S. Slikboer, L. Grandy, S. L. Blair, S. A. Nizkorodov, R. W. Smith and H. A. Al-Abadleh, *Environ. Sci. Technol.*, 2015, **49**, 7793–7801.
71 C. Wang, Y. D. Lei, S. Endo and F. Wania, *Environ. Sci. Technol.*, 2014, **48**, 13238–13245.
72 J. H. Seinfeld, *Nat. Geosci.*, 2008, **1**, 15–16.
73 M. Tang, D. J. Cziczo and V. H. Grassian, *Chem. Rev.*, 2016, **116**, 4205–4259.
74 B. A. Maher, J. M. Prospero, D. Mackie, D. Gaiero, P. P. Hesse and Y. Balkanski, *Earth-Sci. Rev.*, 2010, **99**, 61–97.
75 N. Mahowald, A. R. Baker, G. Bergametti, N. Brooks, R. A. Duce, T. D. Jickells, N. Kubilay, J. M. Prospero and I. Tegen, *Global Biogeochem. Cycles*, 2005, **19**, GB4025, 4021–4015.
76 T. M. Conway and S. G. John, *Nature*, 2014, **511**, 212–215.
77 H. A. Al-Abadleh, *RSC Adv.*, 2015, **5**, 45785–45811.
78 C. R. Usher, A. E. Michel and V. H. Grassian, *Chem. Rev.*, 2003, **103**, 4883–4940.
79 S. R. Taylor, *Geochim. Cosmochim. Acta*, 1964, **28**, 1273–1285.
80 P. N. Sedwick, E. r. Sholkovitz and T. M. Church, *Geochem., Geophys., Geosyst.*, 2007, **8**, Q10Q06.
81 P. N. Sedwick, E. R. Sholkovitz and T. M. Church, *Geochem., Geophys., Geosyst.*, 2007, **8**, Q10Q06.
82 H. Chen, A. Laskin, J. Baltrusaitis, C. A. Gorski, M. M. Scherer and V. H. Grassian, *Environ. Sci. Technol.*, 2012, **46**, 2112–2120.
83 C. Guieu, S. Bonnet, T. Wagener and M.-D. Loye-Pilot, *Geophys. Res. Lett.*, 2005, **32**, L19608, DOI: 10.1029/2005GL022962.
84 A. Ito, *Environ. Sci. Technol. Lett.*, 2015, **2**, 70–75.
85 A. Ito, S. Myriokefalitakis, M. Kanakidou, N. Mahowald, R. A. Scanza, D. S. Hamilton, A. R. Baker, T. D. Jickells, M. Sarin, S. Bikkina, Y. Gao, R. U. Shelley, C. S. Buck, W. M. Landing, A. R. Bowie, M. M. G. Perron, C. Guieu, N. Meskhidze, M. S. Johnson, Y. Feng, J. F. Kok, A. Nenes and R. A. Duce, *Sci. Adv.*, 2019, **5**, eaau7671.
86 R. M. Harrison, A. M. Jones, J. Gietl, J. X. Yin and D. C. Green, *Environ. Sci. Technol.*, 2012, **46**, 6523–6529.
87 M. Schulz, J. M. Prospero, A. R. Baker, F. Dentener, L. Ickes, P. S. Liss, N. Mahowald, S. Nickovic, C. P. Garcia-Pando, S. Rodriguez, M. Sarin, I. Tegen and R. A. Duce, *Environ. Sci. Technol.*, 2012, **46**, 10390–10404.
88 A. Ito and Z. Shi, *Atmos. Chem. Phys.*, 2016, **16**, 85–99.
89 M. Oakes, R. J. Weber, B. Lai, A. Russell and E. D. Ingall, *Atmos. Chem. Phys.*, 2012, **12**, 745–756.
90 A. J. Butler, M. S. Andrew and A. G. Russell, *J. Geophys. Res.: Atmos.*, 2003, **108**, SOS3-1–SOS3-11.

91 P. Hoffmann, A. N. Dedik, J. Ensling, S. Weinbruch, S. Weber, T. Sinner, P. Gutlich and H. M. Ortner, *J. Aerosol Sci.*, 1996, **27**, 325–327.
92 A. M. Johansen, R. Siefert and M. R. Hoffmann, *J. Geophys. Res.: Atmos.*, 2000, **105**, 15277–15312.
93 W. Liu, Y. H. Wang, A. Russell and E. S. Edgerton, *Atmos. Environ.*, 2005, **39**, 4453–4470.
94 M. Oakes, N. Rastogi, B. J. Majestic, M. Shafer, J. J. Schauer, E. S. Edgerton and R. J. Weber, *J. Geophys. Res.: Atmos.*, 2010, **115**, 1–12.
95 A. P. Ault, T. M. Peters, E. J. Sawvel, G. S. Casuccio, R. D. Willis, G. A. Norris and V. H. Grassian, *Environ. Sci. Technol.*, 2012, **46**, 4331–4339.
96 T. L. Guasco, L. A. Cuadra-Rodriguez, B. E. Pedler, A. P. Ault, D. B. Collins, D. Zhao, M. J. Kim, M. J. Ruppel, S. C. Wilson, R. S. Pomeroy, V. H. Grassian, F. Azam, T. H. Bertram and K. A. Prather, *Environ. Sci. Technol.*, 2014, **48**, 1324–1333.
97 A. P. Ault, M. J. Moore, H. Furutani and K. A. Prather, *Environ. Sci. Technol.*, 2009, **43**, 3500–3506.
98 A. P. Ault, C. J. Gaston, Y. Wang, G. Dominguez, M. H. Thiemen and K. A. Prather, *Environ. Sci. Technol.*, 2010, **44**, 1954–1961.
99 K. Deboudt, P. Flament, M. Choel, A. Gloter, S. Sobanska and C. Colliex, *J. Geophys. Res.: Atmos.*, 2010, **115**, D24207.
100 C. Oppo, S. Bellandi, N. D. Innocenti, A. M. Stortini, G. Loglio, E. Schiavuta and R. Cini, *Mar. Chem.*, 1999, **63**, 235–253.
101 S. R. Piotrowicz, R. A. Duce, J. L. Fasching and C. P. Weisel, *Mar. Chem.*, 1979, **7**, 307–324.
102 C. P. Weisel, R. A. Duce, J. L. Fasching and R. W. Heaton, *J. Geophys. Res.: Atmos.*, 1984, **89**, 1607–1618.
103 O. A. Choobari, P. Zawar-Reza and A. Sturman, *Atmos. Res.*, 2014, **138**, 152–165.
104 G. Rubasinghege, S. Elzey, J. Baltrusaitis, P. M. Jayaweera and V. H. Grassian, *J. Phys. Chem. Lett.*, 2010, **1**, 1729–1737.
105 K. Schepanski, *Geosciences*, 2018, **8**, 151, DOI: 10.3390/geosciences8050151.
106 Z. B. Shi, M. D. Krom, T. D. Jickells, S. Bonneville, K. S. Carslaw, N. Mihalopoulos, A. R. Baker and L. G. Benning, *Aeolian Res*, 2012, **5**, 21–42.
107 M. F. M. McDaniel, E. D. Ingall, P. L. Morton, E. Castorina, R. J. Weber, R. U. Shelley, W. M. Landing, A. F. Longo, Y. Feng and B. Lai, *ACS Earth Space Chem.*, 2019, **3**, 2443–2451.
108 R. C. Sullivan, S. A. Guazzotti, D. A. Sodeman and K. A. Prather, *Atmos. Chem. Phys.*, 2007, **7**, 1213–1236.
109 W. Li, L. Shao, D. Zhang, C.-U. Ro, M. Hu, X. Bi, H. Geng, A. Matsuki, H. Niu and J. Chen, *J. Cleaner Prod.*, 2016, **112**, 1330–1349.
110 W. Li, L. Shao, Z. Shi, J. Chen, Q. Yuan, C. Yan, X. Zhang, Y. Wang, J. Sun, Y. Zhang, X. Shen, Z. Wang and W. Wang, *J. Geophys. Res.: Atmos.*, 2014, **119**, 1044–1059.
111 B. Weinzierl, A. Ansmann, J. M. Prospero, D. Althausen, N. Benker, F. Chouza, M. Dollner, D. Farrell, W. K. Fomba, V. Freudenthaler, J. Gasteiger, S. Grob, M. Haarig, B. Heinold, K. Kandler, T. B. Kristensen, O. L. Mayol-Bracero, T. Muller, O. Reitebuch, D. Sauer, A. Schafler, K. Schepanski, A. Spanu, I. Tegen, C. Toledano and A. Walser, *Bull. Am. Meteorol. Soc.*, 2017, **98**, 1427–1451.
112 D. Liu, J. W. Taylor, J. Crosier, N. Marsden, K. N. Bower, G. Lloyd, C. L. Ryder, J. K. Brooke, R. Cotton, F. Marenco, A. Blyth, Z. Cui, V. Estelles, M. Gallagher, H. Coe and T. W. Choularton, *Atmos. Chem. Phys.*, 2018, **18**, 3817–3838.
113 C. Denjean, P. Formenti, K. Desboeufs, S. Chevaillier, S. Triquet, M. Maille, M. Cazaunau, B. Laurent, O. L. Mayol-Bracero, P. Vallejo, M. Quinones, I. E. Gutierre-Molina, F. Cassola, P. Prati, E. Andrews and J. Ogren, *J. Geophys. Res.: Atmos.*, 2016, **121**, 7117–7138.
114 E. Kadar, A. Fisher, B. Stople, S. Calabrese, J. Lead, E. Valsami-Jones and Z. Shi, *Sci. Total Environ.*, 2014, **466–467**, 864–870.
115 M. Tang, X. Huang, K. Lu, M. Ge, Y. Li, P. Cheng, T. Zhu, A. Ding, Y. Zhang, S. Gligorovski, W. Song, X. Ding, B. Xinhui and X. Wang, *Atmos. Chem. Phys.*, 2017, **17**, 11727–11777.
116 M. N. Romanias, H. Ourrad, F. Thevenet and V. Riffault, *J. Phys. Chem. A*, 2016, **120**, 1197–1212.
117 M. C. Gonzalez and E. S. Roman, in *Hdb Environmental Chemistry*, Springer-Verlag, Berlin, 2005, vol. 2, pp. 49–75.
118 C. George, B. D'Anna, H. Herrmann, C. Weller, V. Vaida, D. J. Donaldson, T. Bartels-Rausch and M. Ammann, in *Atmospheric and Aerosol Chemistry*, ed. V. F. McNeill and P. A. Ariya, Springer, Heidelberg, 2012, vol. 339, pp. 1–54.
119 L. Deguillaume, M. Leriche, K. Desboeufs, G. Mailhot, C. George and N. Chaumerliac, *Chem. Rev.*, 2005, **105**, 3388–3431.
120 D. K. Singh and T. Gupta, *J. Aerosol Sci.*, 2016, **94**, 56–69.
121 H. Chen, J. G. Navea, M. A. Young and V. H. Grassian, *J. Phys. Chem. A*, 2011, **115**, 490–499.
122 Z. Shi, M. D. Krom, S. Bonneville and L. G. Benning, *Environ. Sci. Technol.*, 2015, **49**, 1472–1477.
123 W. Stumm, *Chemistry of the Solid-Water Interface*, John Wiely & Sons, Inc., New York, 1992.
124 D. W. Griffin, C. A. Kellogg and E. A. Shinn, *Global Change and Human Health*, 2001, **2**, 20–33.
125 V. Ramanathan, P. J. Crutzen, J. Lelieveld, A. P. Mitra, D. Althausen, J. Anderson, M. O. Andreae, W. Cantrell, G. R. Cass, C. E. Chung, A. D. Clarke, J. A. Coakley, W. D. Collins, W. C. Conant, F. Dulac, J. Heintzenberg, A. J. Heymsfield, B. Holben, S. Howell, J. Hudson, A. Jayaraman, J. T. Kiehl, T. N. Krishnamurti, D. Lubin, G. McFarquhar, T. Novakov, J. A. Ogren, I. A. Podgorny, K. Prather, K. Priestley, J. M. Prospero, P. K. Quinn, K. Rajeev, P. Rasch, S. Rupert, R. Sadourny, S. K. Satheesh, G. E. Shaw, P. Sheridan and F. P. J. Valero, *J. Geophys. Res. D*, 2001, **106**, 28371–28398.
126 R. Paris, K. Desboeufs, P. Formenti, S. Nava and C. Chou, *Atmos. Chem. Phys.*, 2010, **10**, 4273–4282.
127 H. Chen and V. H. Grassian, *Environ. Sci. Technol.*, 2013, **47**, 10312–10321.
128 G. Rubasinghege, R. W. Lentz, M. M. Scherer and V. H. Grassian, *Proc. Natl. Acad. Sci. U. S. A.*, 2010, **107**, 6628–6633.

129 H. Chen, A. Laskin, J. Baltrusaitis, C. A. Gorski, M. M. Scherer and V. H. Grassian, *Environ. Sci. Technol.*, 2012, **46**, 2112–2120.
130 C. S. Buck, W. M. Landing and J. A. Resing, *Mar. Chem.*, 2010, **102**, 14–24.
131 N. Meskhidze, D. Hurley, T. M. Royalty and M. S. Johnson, *Mar. Chem.*, 2017, **194**, 124–132.
132 R. Paris and K. Desboeufs, *Atmos. Chem. Phys.*, 2013, **13**, 4895–4905.
133 A. S. Wozniak, R. U. Shelley, S. D. McElhenie, W. M. Landing and P. G. Hatcher, *Mar. Chem.*, 2015, **173**, 162–172.
134 T. Fang, H. Guo, L. Zeng, V. Verma, A. Nenes and R. J. Weber, *Environ. Sci. Technol.*, 2017, **51**, 2611–2620.
135 D. E. Romonosky, Y. Li, M. Shiraiwa, A. Laskin, J. Laskin and S. A. Nizkorodov, *J. Phys. Chem. A*, 2017, **121**, 1298–1309.
136 D. E. Romonosky, A. Laskin, J. Laskin and S. A. Nizkorodov, *J. Phys. Chem. A*, 2015, **119**, 2594–2606.
137 A. P. Bateman, S. A. Nizkorodov, J. Laskin and A. Laskin, *Phys. Chem. Chem. Phys.*, 2011, **13**, 12199–12212.
138 R. F. Hems and J. P. D. Abbatt, *ACS Earth Space Chem.*, 2018, **2**, 225–234.
139 J. Chen and W. R. Browne, *Coord. Chem. Rev.*, 2018, **374**, 15–35.
140 A. Bianco, M. Passananti, M. Brigante and G. Mailhot, *Molecules*, 2020, **25**(2), 423.
141 U. Lueder, B. B. Jorgensen, A. Kappler and C. Schmidt, *Environ. Sci.: Processes Impacts*, 2020, **22**.
142 R. F. Hems, J. S. Hsieh, M. A. Slodki, S. M. Zhou and J. P. D. Abbatt, *Environ. Sci. Technol. Lett.*, 2017, **4**, 439–443.
143 B. J. Holmes and G. A. Petrucci, *J. Atmos. Chem.*, 2007, **58**, 151–166.
144 A. M'Hemdi, B. Dbira, R. Abdelhedi, E. Brillas and S. Ammar, *Clean: Soil, Air, Water*, 2012, **40**, 878–885.
145 T. B. Nguyen, M. M. Coggon, R. C. Flagan and J. H. Seinfeld, *Environ. Sci. Technol.*, 2013, **47**, 4307–4316.
146 J. Rodriguez, D. Contreras, C. Oviedo, J. Freer and J. Baeza, *Water Sci. Technol.*, 2004, **49**, 81–84.
147 M. Gen, R. Zhang, Y. Li and C. K. Chan, *Environ. Sci. Technol.*, 2020, **54**, 9862–9871.
148 H. A. Al-Abadleh, M. S. Rana, W. Mohammed and M. I. Guzman, *Environ. Sci. Technol.*, 2021, **55**, 209–219.
149 M. Reggente, A. M. Dillner and S. Takahama, *Atmos. Meas. Tech.*, 2019, **12**, 2287–2312.
150 G. Cao, Y. Yan, X. Zou, R. Zhu and F. Ouyang, *Spectral Anal. Rev.*, 2018, **6**, 12–32.
151 R. M. B. O. Duarte and A. C. Duarte, *Magn. Reson. Chem.*, 2014, **53**, 658–666.
152 C. E. Stockwell, P. R. Veres, J. Williams and R. J. Yokelson, *Atmos. Chem. Phys.*, 2015, **15**, 845–865.
153 P. Veres, J. M. Roberts, I. R. Burling, C. Warneke, J. de Gouw and R. J. Yokelson, *J. Geophys. Res. D*, 2010, **115**, D23302, DOI: 10.1029/2010JD014033.
154 L. E. Hatch, A. Rivas-Ubach, C. N. Jen, M. Lipton, A. H. Goldstein and K. C. Barsanti, *Atmos. Chem. Phys.*, 2018, **18**, 17801–17817.
155 J. Ofner, H.-U. Kruger, H. Grothe, P. Schmitt-Kopplin, K. Whitmore and C. Zetzsch, *Atmos. Chem. Phys.*, 2011, **11**, 1–15.
156 J. Lelieveld, P. J. Crutzen, V. Ramanathan, M. O. Andreae, C. A. M. Brenninkmeijer, T. Campos, G. R. Cass, R. R. Dickerson, H. Fischer, J. A. de Gouw, A. Hansel, A. Jefferson, D. Kley, A. T. J. de Laat, S. Lal, M. G. Lawrence, J. M. Lobert, O. L. Mayol-Bracero, A. P. Mitra, T. Novakov, S. J. Oltmans, K. A. Prather, T. Reiner, H. Rodhe, H. A. Scheeren, D. Sikka and J. Williams, *Science*, 2001, **291**, 1031–1036.
157 A. Salam, M. Hasan, B. A. Begum, M. Begum and S. K. Biswas, *Biomass Bioenergy*, 2013, **52**, 122–130.
158 E. A. Pillar, R. X. Zhou and M. I. Guzman, *J. Phys. Chem. A*, 2015, **119**, 10349–10359.
159 Z. Finewax, J. de Gouw and P. J. Ziemann, *Environ. Sci. Technol.*, 2018, **52**, 1981–1989.
160 B. Minofar, P. Jungwirth, M. R. Das, W. Kunz and S. J. Mahiuddin, *J. Phys. Chem. C*, 2007, **111**, 8242–8247.
161 R. Sander, *Atmos. Chem. Phys.*, 2015, **15**, 4399–4981.
162 K. Kawamura and S. Bikkina, *Atmos. Res.*, 2016, **170**, 140–160.
163 S. Kundu, K. Kawamura, T. W. Andreae, A. Hoffer and M. O. Andreae, *Atmos. Chem. Phys.*, 2010, **10**, 2209–2225.
164 M. E. Jenkin, S. M. Saunders, V. Wagner and M. J. Pilling, *Atmos. Chem. Phys.*, 2003, **3**, 181–193.
165 E. Borras, L. Antonio and L. A. Genaro-Tortajada, *Atmos. Environ.*, 2012, **47**, 154–163.
166 M. Huang, Y. Lin and X. Huang, *J. Atmos. Chem.*, 2014, **71**, 213–224.
167 Z. Y. Cong, K. Kawamura, S. C. Kang and P. Q. Fu, *Sci. Rep.*, 2015, **5**, 9580.
168 K. Kawamura, E. Tachibana, K. Okuzawa, S. G. Aggarwal, Y. Kanaya and Z. F. Wang, *Atmos. Chem. Phys.*, 2013, **13**, 8285–8302.
169 H. Okochi and P. Brimblecombe, *Sci. World. J.*, 2002, **2**, 767–786.
170 *CRC Handbook of Chemistry and Physics*, ed. D. R. Lide, Taylor & Francis, Boca Raton, 2012–2013.
171 J. N. Spencer, R. A. Heckman, R. S. Harner, S. L. Shoop and K. S. Robertson, *J. Phys. Chem.*, 1973, **77**, 3103–3106.
172 N. V. Deorkar and L. L. Tavlarides, *Hydrometallurgy*, 1997, **46**, 121–135.
173 N. P. Slabbert, *Tetrahedron*, 1977, **33**, 821–824.
174 S. R. Cooper and V. J. Tulane, *Ind. Eng. Chem., Anal. Ed.*, 1936, **8**, 210–211.
175 A. I. Biggs, *Trans. Faraday Soc.*, 1956, **52**, 35–39.
176 C. George, R. S. Strekowski, J. Kleffmann, K. Stemmler and M. Ammann, *Faraday Discuss.*, 2005, **130**, 195–210.
177 E. F. G. Herington and W. Kynaston, *Trans. Faraday Soc.*, 1957, **53**, 138–142.
178 Z. Pawelka and T. Zeegers-Huyskens, *Can. J. Chem.*, 2003, **81**, 1012–1018.
179 R. Sander, *Atmos. Chem. Phys.*, 2015, **15**, 4399–4981.
180 C. Marcolli, B. Luo and T. Peter, *J. Phys. Chem. A*, 2004, **108**, 2216–2224.
181 Pubchem, https://pubchem.ncbi.nlm.nih.gov.

182 *Visual MINTEQ Ver. 3.1*, 2000, https://vminteq.lwr.kth.se.
183 E. Mentasti and C. Baiocchi, *J. Coord. Chem.*, 1980, **10**, 229–237.
184 E. G. Moorhead and N. Sutin, *Inorg. Chem.*, 1966, **5**, 1866–1871.
185 B. Kormanyos, G. Peintler, A. Nagy and I. Nagypal, *Int. J. Chem. Kinet.*, 2008, **40**, 114–124.
186 E. Mentasti, *Inorg. Chem.*, 1979, **18**, 1512–1515.
187 E. Mentasti and E. Pelizzetti, *J. Chem. Soc., Dalton Trans.*, 1973, **1**, 2605–2608.
188 J. G. Charrier and C. Anastasio, *Atmos. Chem. Phys.*, 2012, **12**, 9321–9333.
189 I. Grgic, in *Environmental Chemistry of Aerosols*, ed. I. Colbeck, Blackwell Publishing Ltd, Oxford, UK, 2008, ch. 5, pp. 117–139.
190 H. Chin, K. S. Hopstock, L. T. Fleming, S. A. Nizkorodov and H. A. Al-Abadleh, *Environ. Sci.: Atmos.*, 2021, **1**, 64–78.
191 L. Huang, R. E. Cochran, E. M. Coddens and V. H. Grassian, *Environ. Sci. Technol. Lett.*, 2018, **5**, 315–321.
192 D. Channei, S. Phanichphant, A. Nakaruk, S. S. Mofarah, P. Koshy and C. C. Sorrell, *Catalysts*, 2017, **7**, 1–23.
193 J. L. N. Xavier, E. Ortega, J. Z. Ferreira, A. M. Bernardes and V. Perez-Herranz, *Int. J. Electrochem. Sci.*, 2011, **6**, 622–636.
194 A. M. Chiorcea-Paquim, T. A. Enache, E. D. Gil and A. M. Oliveira-Brett, *Compr. Rev. Food Sci. Food Saf.*, 2020, **19**, 1680–1726.
195 T. Kasa and T. Solomon, *Am. J. Phys. Chem.*, 2016, **5**, 45–55.
196 P. E. Hayes, J. D. Glennon, A. Buzid and J. H. T. Luong, *Electroanalysis*, 2020, **32**, 119–127.
197 O. Scialdone, A. Galia and C. Guarisco, *Electroanalysis*, 2013, **4**, 290–301.
198 N. R. Perron and J. L. Brumaghim, *Cell Biochem. Biophys.*, 2009, **53**, 75–100.
199 N. R. Perron, H. C. Wang, S. N. DeGuire, M. Jenkins, M. Lawson and J. L. Brumaghim, *Dalton Trans.*, 2010, **39**, 9982–9987.
200 J. Tofan-Lazar, A. Situm and H. A. Al-Abadleh, *J. Phys. Chem. A*, 2013, **117**, 10368–10380.
201 W. Feng and D. Nansheng, *Chemosphere*, 2000, **41**, 1137–1147.
202 H. Kipton, J. Powell and M. C. Taylor, *Aust. J. Chem.*, 1982, **35**, 739–756.
203 G. Albarran, W. Boggess, V. Rassolov and R. H. Schuler, *J. Phys. Chem. A*, 2010, **114**, 7470–7478.
204 A. Lee, A. H. Goldstein, M. D. Keywood, S. Gao, V. Varutbangkul, R. Bahreini, N. L. Ng, R. C. Flagan and J. H. Seinfeld, *J. Geophys. Res.*, 2006, **111**, D07302, DOI: 10.1029/2005JD006437.
205 B. Ervens, B. J. Turpin and R. J. Weber, *Atmos. Chem. Phys.*, 2011, **11**, 11069–11102.
206 N. Link, N. Removski, J. Yun, L. Fleming, S. A. Nizkorodov, A. K. Bertram and H. A. Al-Abadleh, *ACS Earth Space Chem.*, 2020, **4**, 1127–1139.
207 E. A. Pillar, R. Zhou and M. I. Guzman, *J. Phys. Chem. A*, 2015, **119**, 10349–10359.
208 K. J. Schmalzl, C. M. Forsyth and P. D. Evans, *Wood Sci. Technol.*, 1995, **29**, 307–319.
209 X. Sun, R. Bai, Y. Zhang, Q. Wang, X. Fan, J. Yuan, L. Cui and P. Wang, *Appl. Biochem. Biotechnol.*, 2013, **171**, 1673–1680.
210 N. Aktas, N. Shahiner, O. Kantoglu, B. Salih and A. Tanyolac, *J. Polym. Environ.*, 2003, **11**, 123–128.
211 A. Lavi, P. Lin, B. Bhaduri, R. Carmieli, A. Laskin and Y. Rudich, *ACS Earth Space Chem.*, 2017, **1**, 637–646.
212 P. Salgado, D. Contreras, H. D. Mansilla, K. Marquez, G. Vidal, C. J. Cobos and D. O. Martire, *New J. Chem.*, 2017, **41**, 12685–12693.
213 S. Dubey, D. Singh and R. A. Misra, *Enzyme Microb. Technol.*, 1998, **23**, 432–437.
214 R. A. Larson and J. M. Hufnal, *Limnol. Oceanogr.*, 1980, **25**, 505–512.
215 C. K. Duesterberg and T. D. Waite, *Environ. Sci. Technol.*, 2007, **41**, 4103–4110.
216 R. L. Crawford, L. E. Robinson and R. D. Foster, *Appl. Environ. Microbiol.*, 1981, **41**, 1112–1116.
217 R. A. Larson and J. M. Hufnal Jr, *Limnol. Oceanogr.*, 1980, **25**, 505–512.
218 B. Morgan and O. Lahav, *Chemosphere*, 2007, **68**, 2080–2084.
219 M. Hayyan, M. A. Hashim and I. M. AlNashef, *Chem. Rev.*, 2016, **116**, 3029–3085.
220 C. K. Duesterberg and T. D. Waite, *Environ. Sci. Technol.*, 2007, **41**, 4103–4110.
221 M. L. Kremer, *J. Phys. Chem. A*, 2003, **107**, 1734–1741.
222 P. A. Lovell and R. J. Young, *Introduction to Polymers*, CRC Press, Boca Raton, FL, 2011.
223 R. L. Crawford, L. E. Robinson and R. D. Foster, *Appl. Environ. Microbiol.*, 1981, **41**, 1112–1116.
224 S. Hwang, C.-H. Lee and I.-S. Ahn, *J. Ind. Eng. Chem.*, 2008, **14**, 487–492.
225 D. R. Doerge, R. L. Divi and M. I. Churchwell, *Anal. Biochem.*, 1997, **250**, 10–17.
226 R. Zhao, A. K. Y. Lee and J. P. D. Abbatt, *J. Phys. Chem. A*, 2012, **116**, 6253–6263.
227 G. Zhang, Q. Lin, L. Peng, Y. Yang, F. Jiang, F. Liu, W. Song, D. Chen, Z. Cai, X. Bi, M. Miller, M. Tang, W. Huang, X. Wang, P. Peng and G. Sheng, *Environ. Sci. Technol.*, 2019, **53**, 1269–1277.
228 C. J. Hennigan, J. Izumi, A. P. Sullivan, R. J. Weber and A. Nenes, *Atmos. Chem. Phys.*, 2015, **15**, 2775–2790.
229 J. Z. Yu, X.-F. Huang, J. Xu and M. Hu, *Environ. Sci. Technol.*, 2005, **39**, 128–133.
230 S. Bikkina, K. Kawamura and M. Sarin, *Environ. Sci. Technol.*, 2017, **51**, 4347–4357.
231 T. Koop, J. Bookhold, M. Shiraiwa and U. Pöschl, *Phys. Chem. Chem. Phys.*, 2011, **13**, 19238–19255.
232 D. A. Thomas, M. M. Coggon, H. Lignell, K. A. Schilling, X. Zhang, R. H. Schwantes, R. C. Flagan, J. H. Seinfeld and J. L. Beauchamp, *Environ. Sci. Technol.*, 2016, **50**, 12241–12249.
233 P. C. Arroyo, K. T. Malecha, M. Ammann and S. A. Nizkorodov, *Phys. Chem. Chem. Phys.*, 2018, **20**, 30021–30031.

234 H. Pang, Q. Zhang, H. Wang, D. Cai, Y. Ma, L. Li, K. Li, X. Lu, H. Chen, X. Yang and J. Chen, *Environ. Sci. Technol.*, 2018, **53**, 127–136.
235 H. Li, H. Y. Guo, B. Pan, S. H. Liao, D. Zhang, X. K. Yang, C. G. Min and B. S. Xing, *Sci. Rep.*, 2016, **6**.
236 S. W. C. Chien, H. L. Chen, M. C. Wang and K. Seshaiah, *Chemosphere*, 2009, **74**, 1125–1133.
237 G. L. Shi, J. Xu, X. Peng, Z. Xiao, K. Chen, Y. Tian, X. Guan, Y. Feng, H. Yu, A. Nenes and A. Russell, *Environ. Sci. Technol.*, 2017, **51**, 4289–4296.
238 T. K. V. Nguyen, Q. Zhang, J. L. Jimenez, M. Pike and A. G. Carlton, *Environ. Sci. Technol. Lett.*, 2016, **3**, 257–263.
239 R. L. Craig, L. Nandy, J. L. Axson, C. S. Dutcher and A. P. Ault, *J. Phys. Chem. A*, 2017, **121**, 5690–5699.
240 S. M. Kreidenweis, K. Koehler, P. J. DeMott, A. J. Prenni, C. Carrico and B. Ervens, *Atmos. Chem. Phys.*, 2005, **5**, 1357–1370.
241 Q. Chen, D. K. Farmer, J. Schneider, S. R. Zorn, C. L. Heald, T. G. Karl, A. Guenther, J. D. Allan, N. Robinson, H. Coe, J. R. Kimmel, T. Pauliquevis, S. Borrmann, U. Poschl, M. O. Andreae, P. Artaxo, J. L. Jimenez and S. T. Martin, *Geophys. Res. Lett.*, 2009, **36**, L20806.
242 J. L. Jimenez, M. R. Canagaratna, N. M. Donahue, A. S. H. Prevot, Q. Zhang, J. H. Kroll, P. F. DeCarlo, J. D. Allan, H. Coe, N. L. Ng, A. C. Aiken, K. S. Docherty, I. M. Ulbrich, A. P. Grieshop, A. L. Robinson, J. Duplissy, J. D. Smith, K. R. Wilson, V. A. Lanz, C. Hueglin, Y. L. Sun, J. Tian, A. Laaksonen, T. Raatikainen, J. Rautiainen, P. Vaattovaara, M. Ehn, M. Kulmala, J. M. Tomlinson, D. R. Collins, M. J. Cubison, E. J. Dunlea, J. A. Huffman, T. B. Onasch, M. R. Alfarra, P. I. Williams, K. Bower, Y. Kondo, J. Schneider, F. Drewnick, S. Borrmann, S. Weimer, K. Demerjian, D. Salcedo, L. Cottrell, R. Griffin, A. Takami, T. Miyoshi, S. Hatakeyama, A. Shimono, J. Y. Sun, Y. M. Zhang, K. Dzepina, J. Kimmel, D. Sueper, J. Jayne, S. C. Herndon, A. M. Trimborn, L. R. Williams, E. C. Wood, A. M. Middlebrook, C. E. Kolb, U. Baltensperger and D. R. Worsnop, *Science*, 2009, **326**, 1525–1529.
243 N. L. Ng, M. R. Canagaratna, Q. Zhang, J. L. Jimenez, J. Tian, I. M. Ulbrich, J. H. Kroll, K. S. Docherty, P. S. Chhabra, R. Bahreini, S. M. Murphy, J. H. Seinfeld, L. Hildebrandt, N. M. Donahue, P. F. DeCarlo, V. A. Lanz, A. S. H. Prevot, E. Dinar, Y. Rudich and D. R. Worsnop, *Atmos. Chem. Phys.*, 2010, **10**, 4625–4641.
244 A. K. Bertram, S. T. Martin, S. J. Hanna, M. L. Smith, A. Bodsworth, Q. Chen, M. Kuwata, A. Liu, Y. You and S. R. Zorn, *Atmos. Chem. Phys.*, 2011, **11**, 10995–11006.
245 G. H. Khoe and R. G. Robins, *J. Chem. Soc., Dalton Trans.*, 1988, 2015–2021, DOI: 10.1039/DT9880002015.
246 A. Leitzke and C. von Sonntag, *Ozone: Sci. Eng.*, 2009, **31**, 301–308.
247 M. P. Tolocka, M. Jang, J. M. Ginter, F. J. Cox, R. M. Kamens and M. V. Johnston, *Environ. Sci. Technol.*, 2004, **38**, 1428–1434.
248 I. Taraniuk, E. R. Graber, A. Kostinski and Y. Rudich, *Geophys. Res. Lett.*, 2007, **34**, L16807, DOI: 10.1029/2007GL029576.
249 E. Dinar, I. Taraniuk, E. R. Graber, T. Anttila, T. F. Mentel and Y. Rudich, *J. Geophys. Res.: Atmos.*, 2007, **112**, D05211, DOI: 10.1029/2006JD007442.
250 R. A. Washenfelder, A. R. Attwood, C. A. Brock, H. Guo, L. Xu, R. J. Weber, N. L. Ng, H. M. Allen, B. R. Ayres, K. Baumann, R. C. Cohen, D. C. Draper, K. C. Duffey, E. Edgerton, J. L. Fry, W. W. Hu, J. L. Jimenez, B. B. Palm, P. Romer, E. A. Stone, P. J. Wooldridge and S. S. Brown, *Geophys. Res. Lett.*, 2015, **42**, 653–664.
251 M. A. J. Harrison, S. Barra, D. Borghesi, D. Vione, C. Arsene and R. L. Olariu, *Atmos. Environ.*, 2005, **39**, 231–248.
252 Y. Iinuma, O. Boge, R. Grafe and H. Herrmann, *Environ. Sci. Technol.*, 2010, **44**, 8453–8459.
253 C. L. Li, Q. F. He, J. Schade, J. Passig, R. Zimmermann, D. Meidan, A. Laskin and Y. Rudich, *Atmos. Chem. Phys.*, 2019, **19**, 139–163.
254 M. L. Colarieti, G. Toscano, M. R. Ardi and G. Greco Jr, *J. Hazard. Mater.*, 2006, **134**, 161–168.
255 S. China and C. Mazzoleni, *Atmosphere*, 2018, **9**, 249, 241–246.
256 K. Gorkowski, N. M. Donahue and R. C. Sullivan, *Chem*, 2020, **6**, 204–220.
257 M. Song, C. Marcolli, U. K. Krieger, D. M. Lienhard and T. Peter, *Faraday Discuss.*, 2013, **165**, 289–316.
258 R. Stevens and A. Dastoor, *Atmosphere*, 2019, **10**(4), 168.
259 N. Riemer and M. West, *Atmos. Chem. Phys.*, 2013, **18**, 12595–12612.
260 W. Li, J. Sun, L. Xu, Z. Shi, N. Riemer, Y. Sun, P. Q. Fu, J. Zhang, Y. Lin, X. Wang, L. Shao, J. Chen, X. Zhang, Z. Wang and W. Wang, *J. Geophys. Res.: Atmos.*, 2016, **121**, 13784–13798, DOI: 10.1002/2016JD025252.
261 T. Bond and R. Bergstrom, *Aerosol Sci. Technol.*, 2006, **40**, 27–67.
262 T. Wriedt, in *The Mie Theory: Basics and Applications*, ed. W. Hergert and T. Wriedt, Springer-Verlag, Heidelberg, 2012, vol. 169, pp. 53–71.
263 D. B. Curtis, B. Meland, M. Aycibiin, N. P. Arnold, V. H. Grassian, M. A. Young and P. D. Kleiber, *J. Geophys. Res.*, 2008, **113**, D08210, DOI: 10.1029/2007JD009387.
264 B. H. Samset, C. W. Stjern, E. Andrews, R. A. Kahn, G. Myhre, M. Schulz and G. L. Schuster, *Curr. Clim. Change Rep.*, 2018, **4**, 65–83.
265 J. Hansen, M. Sato and R. Ruedy, *J. Geophys. Res.*, 1997, **102**, 6831–6864.
266 C. Textor, M. Schulz, S. Guibert, S. Kinne, Y. Balkanski, S. Bauer, T. Berntsen, T. Berglen, O. Boucher, M. Chin, *et al.*, *Atmos. Chem. Phys.*, 2006, **6**, 1777–1813.
267 J. F. Kok, D. A. Ridley, Q. Zhou, R. L. Miller, C. Zhao, C. L. Heald, *et al.*, *Nat. Geosci.*, 2017, **10**, 274–278.
268 L. Caponi, P. Formenti, D. Massabo, C. Di Biagio, M. Cazaunau, E. Pangui, *et al.*, *Atmos. Chem. Phys.*, 2017, **17**, 7175–7191.
269 S. K. Satheesh and K. K. Moorthy, *Atmos. Environ.*, 2005, **39**, 2089–2110.

270 H. Liao and J. H. Seinfeld, *J. Geophys. Res. D.*, 1998, **103**(D24), 31637–31645.
271 Y. J. Kaufman, D. Tanre, O. Dubovik, A. Karnieli and L. A. Remer, *Geophys. Res. Lett.*, 2001, **28**, 1479–1482.
272 O. Dubovik, B. Holben, T. F. Eck, A. Smirnov, Y. J. Kaufman, M. D. King, a. Tanre and I. Slutsker, *J. Atmos. Sci.*, 2002, **59**, 590–608.
273 R. A. Scanza, N. Mahowald, S. Ghan, C. S. Zender, J. F. Kok, X. Liu, Y. Zhang and S. Albani, *Atmos. Chem. Phys.*, 2015, **15**, 537–561.
274 A. D. Clarke, Y. Shinozuka, V. N. Kapustin, S. Howell, B. Huebert, S. Doherty, T. Anderson, D. Covert, J. Abderson, X. Hua, K. G. Moore II, C. McNaughton, G. Carmichael and R. Weber, *J. Geophys. Res.: Atmos.*, 2004, **109**(D15), D15S09, DOI: 10.1029/2003JD004378.
275 B. V. Scarnato, S. China, K. Nielsen and C. Mazzoleni, *Atmos. Chem. Phys.*, 2015, **15**, 6913–6928.
276 C. Denjean, F. Cassola, A. Mazzino, S. Triquet, S. Chevaillier, N. Grand, T. Bourrianne, G. Momboisse, K. Sellegri, A. Schwarzenbock, E. Freney, M. Mallet and P. Formenti, *Atmos. Chem. Phys.*, 2016, **16**, 1081–1104.
277 J. Bi, J. Huang, B. Holben and G. Zhang, *Atmos. Chem. Phys.*, 2016, **16**, 15501–15516.
278 L. Xu, S. Fukushima, S. Sobanska, K. Murata, A. Naganuma, L. Liu, Y. Wang, H. Niu, Z. Shi, T. Kojima, D. Zhang and W. Li, *Atmos. Chem. Phys.*, 2020, **20**, 14321–14332.
279 V. Ramanathan and G. Carmichael, *Nat. Geosci.*, 2008, **1**, 221–227.
280 T. C. Bond, S. Doherty, D. W. Fahey, P. M. Forster, T. Bernsten, *et al.*, *J. Geophys. Res.: Atmos.*, 2013, **118**, 5380–5552.
281 O. Gustafsson and V. Ramanathan, *Proc. Natl. Acad. Sci. U. S. A.*, 2016, **113**, 4243–4245.
282 J. Peng, M. Hu, S. Guo, Z. Du, J. Zheng, D. Shang, M. L. Zamora, L. Zeng, M. Shao, Y.-S. Wu, J. Zheng, Y. Wang, C. R. Glen, D. R. Collins, M. J. Molina and R. Zhang, *Proc. Natl. Acad. Sci. U. S. A.*, 2016, **113**, 4266–4271.
283 O. Boucher, Y. Balkanski, O. Hodnebrog, C. E. L. Myhre, G. Myhre, J. Quaas, B. H. Samset, N. Schutgen, P. Stier and R. Wang, *Proc. Natl. Acad. Sci. U. S. A.*, 2016, **113**, E5092–E5093.
284 Y. Zhang, O. Favez, F. Canonaco, D. Liu, G. Mocnik, T. Amodeo, J. Sciare, A. S. H. Prevot, V. Gros and A. Albinet, *npj Clim. Atmos. Sci.*, 2018, **47**, 1–8.
285 T. C. Bond and R. W. Bergstrom, *Aerosol Sci. Technol.*, 2006, **40**, 27–67.
286 C. D. Cappa, T. B. Onasch, P. Massoli, D. R. Worsnop, T. S. Bates, E. S. Cross, P. Davidovits, J. Hakala, K. L. Hayden, B. T. Jobson, K. R. Kolesar, D. A. Lack, B. M. Lerner, S.-M. Li, D. Mellon, I. Nuaaman, J. S. Olfert, T. Petäjä, P. K. Quinn, C. Song, R. Subramanian, E. J. Williams and R. A. Zaveri, *Science*, 2012, **337**, 1078–1081.
287 X. Cui, X. Wang, L. Yang, B. Chen, J. Chen, A. Andersson and Ö. Gustafsson, *Sci. Total Environ.*, 2016, **551**, 51–56.
288 J. Peng, M. Hu, S. Guo, Z. Du, J. Zheng, D. Shang, M. Levy Zamora, L. Zeng, M. Shao, Y.-S. Wu, J. Zheng, Y. Wang, C. R. Glen, D. R. Collins, M. J. Molina and R. Zhang, *Proc. Natl. Acad. Sci. U. S. A.*, 2016, **113**, 4266–4271.
289 S. Liu, A. C. Aiken, K. Gorkowski, M. K. Dubey, C. D. Cappa, L. R. Williams, S. C. Herndon, P. Massoli, E. C. Fortner, P. S. Chhabra, W. A. Brooks, T. B. Onasch, J. T. Jayne, D. R. Worsnop, S. China, N. Sharma, C. Mazzoleni, L. Xu, N. L. Ng, D. Liu, J. D. Allan, J. D. Lee, Z. L. Fleming, C. Mohr, P. Zotter, S. Szidat and A. S. H. Prévôt, *Nat. Commun.*, 2015, **6**, 8435.
290 R. M. Healy, J. M. Wang, C. H. Jeong, A. K. Y. Lee, M. D. Willis, E. Jaroudi, N. Zimmerman, N. Hilker, M. Murphy, S. Eckhardt, A. Stohl, J. P. D. Abbatt, J. C. Wenger and G. J. Evans, *J. Geophys. Res.: Atmos.*, 2015, **120**, 6619–6633.
291 T. Nakayama, Y. Ikeda, Y. Sawada, Y. Setoguchi, S. Ogawa, K. Kawana, M. Mochida, F. Ikemori, K. Matsumoto and Y. Matsumi, *J. Geophys. Res.: Atmos.*, 2014, **119**, 12721–12739.
292 P. R. Sinha, Y. Kondo, M. Koike, J. A. Ogren, A. Jefferson, T. E. Barrett, R. J. Sheesley, S. Ohata, N. Moteki, H. Coe, D. Liu, M. Irwin, P. Tunved, P. K. Quinn and Y. Zhao, *J. Geophys. Res.: Atmos.*, 2017, **122**, 3544–3572.
293 Z.-J. Lan, X.-F. Huang, K.-Y. Yu, T.-L. Sun, L.-W. Zeng and M. Hu, *Atmos. Environ.*, 2013, **69**, 118–123.
294 D. Liu, J. Whitehead, M. R. Alfarra, E. Reyes-Villegas, D. V. Spracklen, C. L. Reddington, S. Kong, P. I. Williams, Y.-C. Ting, S. Haslett, J. W. Taylor, M. J. Flynn, W. T. Morgan, G. McFiggans, H. Coe and J. D. Allan, *Nat. Geosci.*, 2017, **10**, 184–188.
295 J. Yan, X. Wang, P. Gong, C. Wang and Z. Cong, *Sci. Total Environ.*, 2018, **634**, 1475–1485.
296 Y. Feng, V. Ramanathan and V. R. Kotamarthi, *Atmos. Chem. Phys.*, 2013, **13**, 8607–8621.
297 A. Laskin, P. Lin, J. Laskin, L. Fleming and S. A. Nizkorodov, in *Multiphase Environmental Chemistry in the Atmosphere*, ed. S. W. Hunt, A. Laskin and S. A. Nizkorodov, American Chemical Society, Washington DC, 2018, vol. 1299, ch. 13, pp. 261–274.
298 M. O. Andreae and A. Gelencser, *Atmos. Chem. Phys.*, 2006, **6**, 3131–3148.
299 A. Tasoglou, E. Louvaris, K. Florou, A. Liangou, E. Karnezi, C. Kaltsonoudis, N. Wang and S. N. Pandis, *Atmos. Chem. Phys.*, 2020, **20**, 11625–11637.
300 M. Fraund, D. J. Bonanno, S. China, D. Q. Pham, D. Veghte, J. Weis, G. Kulkarni, K. Teske, M. K. Gilles, A. Laskin and R. C. Moffet, *Atmos. Chem. Phys.*, 2020, **20**, 11593–11606.
301 D. Liu, C. He, J. P. Schwarz and X. Wang, *npj Clim. Atmos. Sci.*, 2020, **3**, 1–18.
302 C. Li, Q. He, Z. Fang, S. S. Brown, A. Laskin, S. R. Cohen and Y. Rudich, *Environ. Sci. Technol.*, 2020, **54**, 11827–11837.
303 L. T. Fleming, P. Lin, J. M. Roberts, V. Selimovic, R. Yokelson, J. Laskin, A. Laskin and S. A. Nizkorodov, *Atmos. Chem. Phys.*, 2020, **20**, 1105–1129.
304 G. Lin, J. E. Penner, M. G. Flanner, S. Sillman, L. Xu and C. Zhou, *J. Geophys. Res.: Atmos.*, 2014, **119**, 7453–7476.

305 Z. Lu, D. G. Streets, E. Winijkul, F. Yan, Y. Chen, T. Bond, Y. Feng, M. K. Dubey, S. Liu, J. P. Pinto and G. Carmichael, *Environ. Sci. Technol.*, 2015, **49**, 4868–4877.
306 Y. Chen and T. C. Bond, *Atmos. Chem. Phys.*, 2010, **10**, 1773–1787.
307 M. A. Rahman and H. A. Al-Abadleh, *ACS Omega*, 2018, **3**, 15519–15529.
308 P. A. Kollman and L. C. Allen, *Chem. Rev.*, 1972, **72**, 283–303.
309 H. Fairbrother, F. M. Geiger, V. H. Grassian and J. C. Hemminger, *J. Phys. Chem. C*, 2009, **113**(6), 2035–2646.
310 R. Signorell and A. K. Bertram, *Phys. Chem. Chem. Phys.*, 2009, **11**, 7741–8104.
311 H. A. Al-Abadleh and V. H. Grassian, *Langmuir*, 2003, **19**, 341–347.
312 G. E. Ewing, *Chem. Rev.*, 2006, **106**, 1511–1526.
313 W. Cantrell and G. E. Ewing, *J. Phys. Chem. B*, 2001, **105**, 5434–5439.
314 B. Bagchi, *Chem. Rev.*, 2005, **105**, 3197–3219.
315 N. Winter, J. Vieceli and I. Benjamin, *J. Phys. Chem. B*, 2008, **112**, 227–231.
316 P. A. Thiel and T. E. Madey, *Surf. Sci. Rep.*, 1987, **7**, 211–385.
317 G. Jeffrey, *An Introduction to Hydrogen Bonding*, Oxford University Press, New York, 1997.
318 L. F. Scatena, M. G. Brown and G. L. Richmond, *Science*, 2001, **292**, 908–912.
319 S. Cowen and H. A. Al-Abadleh, *Phys. Chem. Chem. Phys.*, 2009, **11**, 7838–7847.
320 M. Tang, W. Gu, Q. Ma, Y. J. Li, C. Zhong, S. Li, X. Yin, R.-J. Huang, H. He and X. Wang, *Atmos. Chem. Phys.*, 2019, **19**, 2247–2258.
321 D. B. Asay, A. L. Barnette and S. H. Kim, *J. Phys. Chem. C*, 2009, **113**, 2128–2133.
322 S. G. Moussa, T. M. McIntire, M. Szori, M. Roeselová, D. J. Tobias, R. L. Grimm, J. C. Hemminger and B. J. Finlayson-Pitts, *J. Phys. Chem. A*, 2009, **113**, 2060–2069.
323 S. E. Lappi, B. Smith and S. Franzen, *Spectrochim. Acta, Part A*, 2004, **60**, 2611–2619.
324 H. R. Wyss and M. Falk, *Can. J. Chem.*, 1970, **48**, 607–614.
325 W. Cheng, K. Hanna and J.-F. Boily, *Environ. Sci. Technol.*, 2019, **53**, 1252–1257.
326 A. Pajunoja, A. T. Lambe, J. Hakala, N. Rastak, M. J. Cummings, J. F. Brogan, L. Hao, M. Paramonov, J. Hong, N. L. Prisle, J. Malila, *et al.*, *Geophys. Res. Lett.*, 2015, **42**, 3063–3068.
327 N. Rastak, A. Pajunoja, J. C. Acosta Navaaro, J. Ma, D. G. Partridge, A. Kirkevag, Y. Leong, W. W. Hu, N. F. Taylor, A. T. Lambe, K. Cerully, *et al.*, *Geophys. Res. Lett.*, 2017, **44**, 5167–5177.
328 J. K. Mayer, X. Wang, M. V. Santander, B. A. Mitts, J. Sauer, C. M. Sultana, C. D. Cappa and K. A. Prather, *ACS Cent. Sci.*, 2020, **6**, 2259–2266.
329 D. K. Farmer, C. D. Cappa and S. M. Kreidenweis, *Chem. Rev.*, 2015, **115**, 4199–4217.
330 Z. A. Kanji, L. A. Ladino, H. Wex, Y. Boose, M. Burkert-Kohn, D. J. Cziczo and M. Kramer, *Meteorol. Monogr.*, 2017, **58**, 1.1–1.33.
331 D. A. Knopf, P. A. Alpert and B. Wang, *ACS Earth Space Chem.*, 2018, **2**, 168–202.
332 B. J. Murray, D. O'Sullivan, J. D. Atkinson and M. E. Webb, *Chem. Soc. Rev.*, 2012, **41**, 6519–6554.
333 N. S. Umo, R. Wagner, R. Ullrich, A. Kiselev, H. Saathoff, P. G. Weidler, D. J. Cziczo, T. Leisner and O. Mohler, *Atmos. Chem. Phys.*, 2019, **19**, 8783–8800.
334 P. J. DeMott, A. J. Prenni, G. R. McMeeking, R. C. Sullivan, M. D. Petters, Y. Tobo, M. Niemand, O. Mohler, J. R. Snider, Z. Wang and S. M. Kriedenweis, *Atmos. Chem. Phys.*, 2015, **15**, 393–409.
335 J. Yun, N. Link, A. Kumar, A. Schukarev, J. Davidson, A. Lam, C. Walters, Y. Xi, J.-F. Boily and A. K. Bertram, *ACS Earth Space Chem.*, 2020, **4**, 873–881.
336 T. F. Whale, M. A. Holden, T. W. Wilson, D. O'Sullivan and B. J. Murray, *Chem. Sci.*, 2018, **9**, 4142–4151.
337 C. Chatre, C. Emmelin, S. Urbaniak, C. George and C. Cogne, *Cryst. Growth Des.*, 2019, **19**, 4619–4624.
338 K. J. Baustian, D. J. Cziczo, M. E. Wise, K. A. Pratt, G. Kulkarni, A. G. Hallar and M. A. Tolbert, *J. Geophys. Res.*, 2012, **117**, D06217.
339 Y. Yun and J. E. Penner, *Geophys. Res. Lett.*, 2013, **40**, 4121–4126.
340 M. Yesilbas and J.-F. Boily, *J. Phys. Chem. Lett.*, 2016, **7**, 2849–2855.
341 A. Kumar, C. Marcolli, B. Luo and T. Peter, *Atmos. Chem. Phys.*, 2018, **18**, 7057–7079.
342 A. Kumar, C. Marcolli and T. Peter, *Atmos. Chem. Phys.*, 2019, **19**, 6035–6058.
343 M. Novic, I. Grgic, M. Poje and V. Hudnik, *Atmos. Environ.*, 1996, **30**, 4191–4196.
344 I. Grgic, A. Dovzan, G. Bercic and V. Hudnik, *J. Atmos. Chem.*, 1998, **29**, 315–337.
345 T. Arakai, C. Anastasio, Y. Kuroki, H. Nakajima, K. Okada, Y. Kotani, D. Handa, S. Azechi, T. Kimura, A. Tsuhako and Y. Miyagi, *Environ. Sci. Technol.*, 2013, **47**, 8196–8203.